Radial and 2D Color Properties of E+A Galaxies

Chisato Yamauchi
Department of Physics and Astrophysics,
Nagoya University

A doctoral dissertation submitted to Nagoya University

November 30, 2004

Contents

Acknowledgments

I am grateful to my advisers, Shin-ichi Ichikawa for his continuous encouragement and support for not only this thesis, but also for my entire graduate school life. He kept an eye on SDSS database on Astronomical Data Analysis Center in National Astronomical Observatory, and I was always able to access the latest SDSS data for my thesis work. The large amount of time I have spent with him during my graduate life has been extremely helpful to me. His presence is as if that of the *Sun* not only for me but everyone in Data Analysis Center. I am indebted to Tomotsugu Goto for introducing me to an interesting field in galaxy astrophysics, an encounter with extremely rare objects in this field — E+A galaxies, and for his continuous and cordial support for my study. If there were no his backup, I could not complete this thesis work. I put him into a great deal of trouble at our UKIRT observation and in various occasions. Nevertheless, his support to me did not changed. I can never thank him enough. I gratefully thank Masataka Fukugita for looking over my paper written in a clumsy style and correcting drastically. I would like to thank Satoru Ikeuchi, Takahiko Matsubara and Tomoyuki Hanawa for important advice in seminars when I was a master's degree student. The experiences is very useful for this theses work. I am grateful to Masaaki Takahashi, Takeyasu Sawa, Masahisa Matsuda and Chitao Suzuki for their continuous support during not only my undergraduate but also graduate life. I thank them for great encouragement to me.

I acknowledge Naoki Yasuda and for his extensive help in technical issues. His suggestion was always appropriate, so I admire his erudition. He also made efforts to keep the SDSS database latest despite frequent disk crashes. I would like to thank Masafumi Yagi for grate help in solving technical problems. He consistently gave me rapid and powerful advice. Although I was sometimes not able to follow the speed of his supercomputer brain, it inspired me a lot. I thank Ani Thakar for his SDSS work and quick advice for my technical questions. I thank Akihiko Ibukiyama for his bright interpretations of my observational results. Although my knowledge fell far short of his, he always brought useful discussions. He also provided tea service for students in my room, and it formed our friendly atmosphere. I thank Issha Kayo, Kanako Sugimoto, Kiyotomo Ichiki and Misato Fukagawa for their continuous friendship, and for showing their spirit of astronomer. I thank Tomomi Ohta, Yuichi Matsuda and other tennis lovers in National Astronomical Observatory for sharing pleasure in tennis. Tennis also became the source of my exertion. I thank Hiroshi

Daisaka for useful discussion and night '*ramen*' tours in Tokyo city. I thank Akira Yoshino for his encouragement and enthusiastic talk of comic books for a breather. I thank Yuko Ishii and Maiko Shingo for having a pleasant time at the connection room of Astronomical Data Analysis Center. The room was an oasis for us. I thank Reiko Nakajima for advice about my talk in the SDSS collaboration meeting at Princeton University. She also makes efforts to study astrophysics for thesis work, it is good encouragement for me.

I thank the SDSS collaboration for creating such a wonderful data set. Working with such a great data set for my graduate life has been quite an experience. I also thank Linux, XFree86, and other UNIX-related communities for the development of various useful softwares.

I thank Johann Sebastian Bach, Helmut Walcha and Kerl Richter for their beautiful and lucidity music. I also thank my father, Etsuo Yamauchi for introducing me the impression of Bach's music. Their music always gave me a tranquil mind, even when I was worried. I thank my mother, Ayako Yamauchi for her continuous encouragement and for watching affectionately for a long time. I can never thank her enough. I thank my sister, Yuri, and grand mother, Chiyo Yamauchi for their continuous support for my entire life. I thank my grand father, Kakusaburo Yamauchi for his placid support during his lifetime, and he has been watching over me in Heaven.

Lastly I thank M. N. for her warm-hearted support. I went through hardships on September, with no promising results in my study. At that time, I attained her salvation, which enabled me to continue my study. I never forget my gratitude to her in my whole life.

With my prayer that I pass a doctoral examination.

Chisato Yamauchi, November 30, 2004.

Abstract

The formation processes of early-type galaxies is a long-standing issue of great importance to galaxy evolution. One of hypothesis is that early-type galaxies form via mergers of gaseous disc galaxies or of many dwarf galaxies (e.g., Toomre 1977). The merger hypothesis is supported by some observational studies, such as the dynamical disturbances of observed ellipticals such as shell structures (e.g., Malin & Carter 1983; Schweizer & Seitzer 1988) and kinematically decoupled cores (e.g., Kormendy 1984; Bender & Surma 1992) of elliptical galaxies. Theoretically, ancestral equal-mass galaxies are completely destroyed so as to form a spheroid that looks more like an elliptical galaxy, and merging of two unequal-mass spirals are finally transformed into one S0 galaxy that has a flattened oblate spheroid (e.g., Bekki 1998), with a centralized violent starburst (e.g., Mihos & Heanquist 1996). More recently, hierarchical galaxy formation models in cold dark matter cosmologies have postulated that massive galaxies have complex assembly histories and were built up gradually through mergers and periods of star formation (White & Frenk 1991). In these models properties such as mass, star formation rate, and morphology are transient, depending largely on the merger history and the time elapsed since the most recent merger (e.g., Kauffmann, White & Guiderdoni 1993).

E+A galaxies have been understood as post-starburst galaxies based on the observed strong Balmer absorption lines and the absence of Hα or [OII] emission lines. Since E+A galaxies are very rare and difficult to find, for more than 20 years, most of the previous work is focused on the global properties of E+A galaxies to reveal the origin of E+A galaxies. Recent studies suggest merger/interaction origin of E+A galaxies, therefore, the E+A phase might be very important stage of galaxy formation scenario. However, the two transitions, "from merger/interaction galaxy to E+A galaxy" and "from E+A galaxy to early-type galaxy", are still uncertain. One of the best way to ascertain the two transitions is the investigation of internal properties, such as age and metallicity gradients, of E+A galaxies along the evolutionary sequence. Previous work often lacked a statistical significance, and did not study them along the evolutionary sequence since E+A galaxies are extremely rare. We then focus on internal properties of E+A galaxies, two-dimensional (2D) color and radial color gradients, and study them along the evolutionary sequence using clean E+A sample in huge galaxy catalog.

In this study, we investigate the radial color gradient and 2D color property of 22 E+A galaxies with 5.5Å $<$ Hδ EW $<$ 8.5Å and normal 49 early-type galaxies as a control sample at the redshift of < 0.2 in the Second Data Release of the Sloan Digital Sky Survey. We found that substantial number of E+A galaxies exhibit positive slopes of radial color gradient (bluer gradients toward the center) which are seldom seen in normal early-type galaxies. We found irregular 'Color Morphologies' – asymmetrical and clumpy pattern – at the center of $g-r$ and $r-i$ 2D colormap of E+A galaxies with positive slope of color gradient. Kolomogorov-Smirnov two-sample tests show that $g-r$ and $r-i$ color gradient distributions of E+A galaxies are different from that of

early-type galaxies with a more than 99.99% significance level. We also found a tight correlation between radial color gradients and colors, and between radial color gradients and 4000Å break in the E+A sample; E+A galaxies which exhibit bluer color or weaker D_{4000} tend to have positive slopes of radial color gradient. We compare the GISSEL model and E+A's observational quantities, Hδ EW, D_{4000} and $u-g$ color, and found that almost all our E+A galaxies are placed under a single evolution track. Therefore, these results are interpreted as E+A galaxies evolve from Hδ EW $\sim$ 8Å to Hδ EW $\sim$ 5Å, their color gradient changes from positive to negative, and the irregular 2D colormap becomes smoother, during the time scale of $\sim$300 Myr.

Our results favor a hypothesis that E+A galaxies are post-starburst galaxies caused by the merger/interaction and underwent a centralized violent starburst, and make the two transitions, "from merger/interaction galaxy to E+A galaxy" and "from E+A galaxy to early-type galaxy", more plausible in one of the evolutionary paths of early-type galaxies.

1 General Introduction

1.1 Evolution Scenarios for Elliptical Galaxies

Elliptical galaxies show a much smaller variation in structure and kinematics than allowed by the models. The clearest example is the very small variation in light profiles, M/L values, the Faber-Jackson relation, the regular isophoto shapes of galaxies, the correlation of v/σ with luminosity and other parameters, the relatively small kinematic misalignments, the color-magnitude relation, etc. (Figure 1). These properties are most likely to be a result of the shared formation process, but not result of the equilibrium dynamics (de Zeeuw & Franx 1991).

The formation processes of elliptical galaxies is a long-standing issue of great

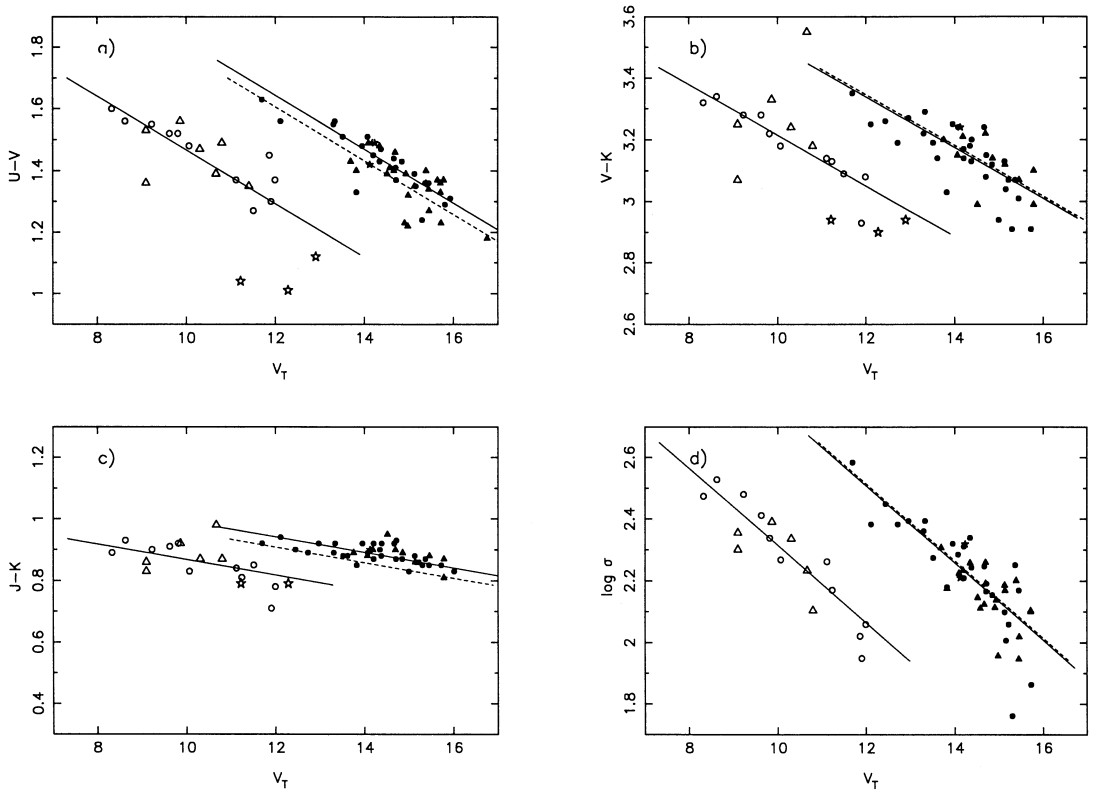

Figure 1: The color-magnitude and Faber-Jackson relations for early-type galaxies in the Virgo and Coma clusters: (a) $U-V$ color-magnitude; (b) $V-K$ color-magnitude; (c) $J-K$ color-magnitude; (d) the Faber-Jackson relation (Bower, Lucey & Ellis 1992).

importance to galaxy evolution. The regularity in the light distribution and the global velocity anisotropy in elliptical galaxies were explained by the violent relaxation (Lynden-Bell 1967). The dissipationless formation of an elliptical galaxy was discussed in various ways. For example, stars have formed prior to the beginning of the collapse of the gas cloud (Gott 1973, 1975) or stars have formed slowly in disc galaxies, which subsequently merge to make a spheroidal galaxy (Marchant & Shapiro 1977; Toomre 1977; Barnes 1988). The limit of dissipationless collapse is amenable to *N*-body experiments, which can form the objects with observed dynamical properties. In addition, not only the collapse but mergers without dissipation can produce the $r^{1/4}$-law profile; simulations have shown that realistic profiles result from a wide variety of initial conditions (e.g., White 1979; van Albada 1982; McGlynn 1984; Aguilar & Merritt 1990). However, the dissipation during formation process is required to explain the photometric and chemical properties of elliptical galaxies such as color-magnitude relation, mass-metallicity relation and the radial color gradients.

There are two competing proposed scenarios of the formation of elliptical galaxies with dissipational process (see Figure 2):

- Monolithic collapse hypothesis

  Elliptical galaxies form monolithically by the gravitational collapse of a gas cloud with considerable energy dissipation (e.g., Larson 1974; Arimono & Yoshii 1987).

- Merger hypothesis

  Elliptical galaxies form via mergers of gaseous disc galaxies or of many dwarf galaxies (e.g., Toomre 1977; Kauffmann, White & Guiderdoni 1993; Baugh, Cole & Frenk 1996; Steinmetz & Navarro 2002)

The merger hypothesis is supported by the dynamical disturbances of observed ellipticals such as shell structures (e.g., Malin & Carter 1983; Schweizer & Seitzer 1988) and kinematically decoupled cores (e.g., Kormendy 1984; Bender & Surma 1992). Schweizer et al. (1990, 1992) found that line strength and UBV colors are correlated with their structure-related parameter which indicates the amount of fine structures such as ripples and jets of luminous matter. They estimates that the merger age of ellipticals with the most fine structures is ~ 4.6 Gyr. Although elliptical galaxies are basically pressure-supported systems, it is known that bright ellipticals tend to be slow rotators and faint ellipticals tend to be rapid rotators.

However, Lauer (1985) found that surface brightness distribution of bright elliptical galaxies can be categorized into boxy- and disky-isophotes (Figure 3), and Bender (1988) reported that elliptical galaxies with box-shaped isophotes frequently owe their shape to anisotropies in their velocity dispersion. In addition, Bender et al. (1989) found that ellipticals which are radio-loud and/or surrounded by gaxeous X-ray halos generally have boxy or irregular isophotes, and boxy ellipticals on average are found to have higher mass-to-light ratios than ellipticals with pointed isophotes. Shioya & Taniguchi (1993) shown that boxy ellipticals tend to appear in rich cluster environments, while the disky type are found in the field, and they summarize the possible formation mechanisms of boxy-elliptical galaxies that boxy ellipticals were formed by a dissipative merger of two gas-rich disk galaxies, with taking account of some previous studies (e.g., Kormendy 1992; Sanders et al. 1988a,b). Theoretically,

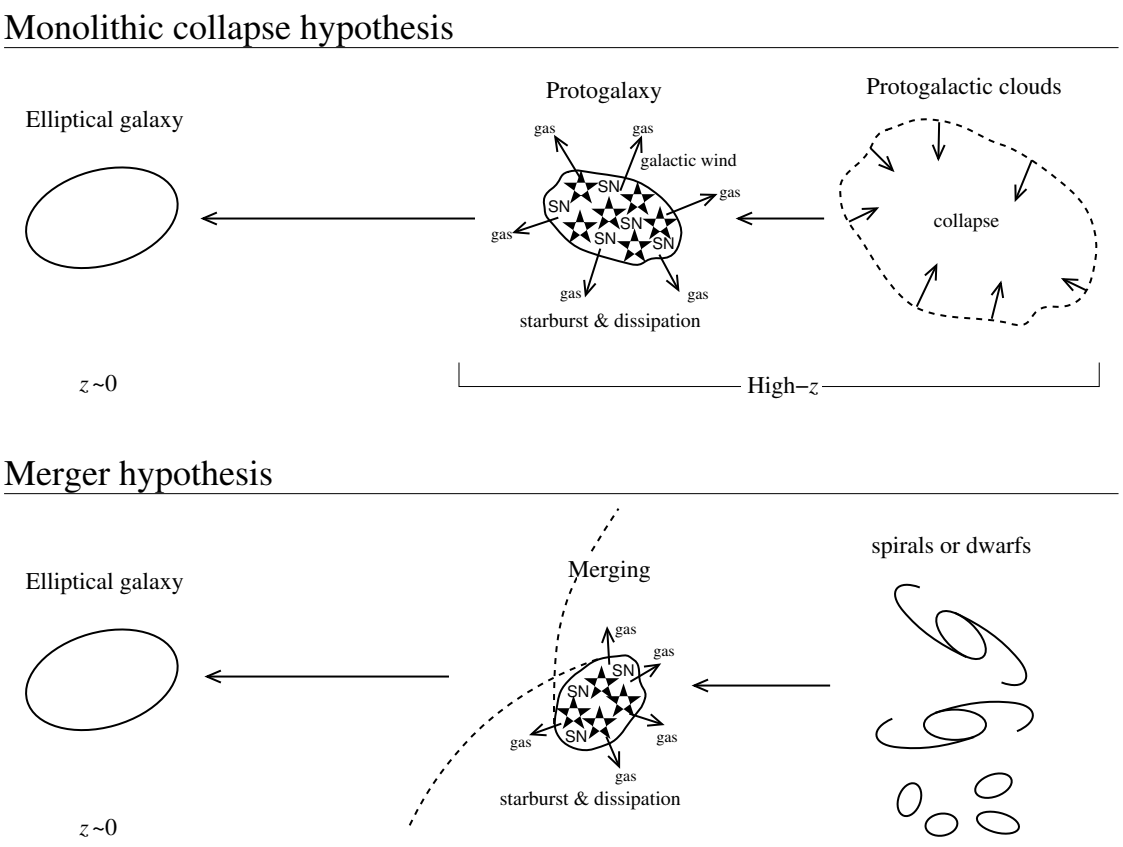

Figure 2: The concept view of monolithic collapse hypothesis (*top*) and merger hypothesis (*bottom*).

Naab, Burkert & Hernquist (1999) modeled 1:1 and 3:1 mass mergers to determine if either type preferentially formed disk- or boxy-type objects. They found that, regardless of projection effects, 1:1 mass mergers produced boxy elliptical galaxies and 3:1 mass mergers produced disky elliptical galaxies. Using more sophisticated models, Naab & Burkert (2003) found that 1:1 mergers produce boxy isophotes, depending on the alignment of the progenitors during the initial encounter. In many cases, their simulations of 1:1 mass mergers produced elliptical galaxies with disky isophotes. Moreover, the morphology-density relation in clusters (e.g., Dressler 1980; Dressler et al. 1997) may be easily explained by the merger hypothesis. However, elliptical galaxies apparently show little evidence for on-going star formation, and old stars occupy their stellar population (e.g., Kodama et al. 1998; Silva & Bothun 1998; Stanford, Eisenhardt & Dickinson 1998).

The monolithic collapse hypothesis assumes that an initial starburst at high redshift forms the most part of stars in galaxies, and then the star formation is quenched with a supernovae-driven galactic wind which expels the left-over interstellar gas from galaxies. The galactic wind is supposed to play an essential role in injecting heavy elements into the hot intracluster gas (Ciotti et al. 1991), and predicts tight correlations among global properties of galaxies such as the color-magnitude relation (Bower, Lucey & Ellis 1992), the metallicity-velocity dispersion relation (Davies et al. 1987) and the fundamental plane (Djorgovski & Davis 1987;

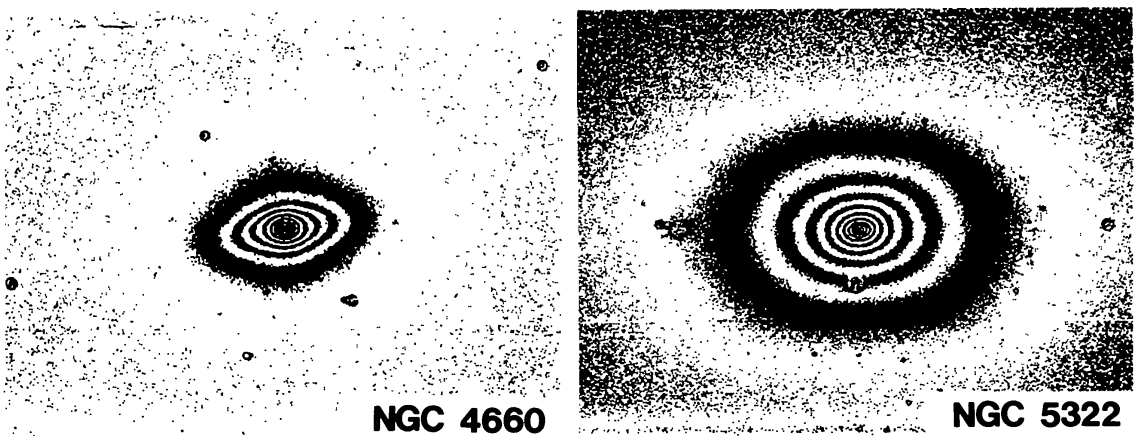

Figure 3: R-image of NGC 4660, an elliptical galaxy with a disk-component in the isophotes (*left*), and R-image of NGC 3522, and elliptical galaxy with box-shaped isophotes (*right*). (Bender, Döbereiner & Möllenhoff 1988).

Dressler et al. 1987). Recent observations of clusters at high redshifts reveal that these relationship exist even at $z\sim1$ (Dickinson 1996; Kelson et al. 1997; Schade, Barrientos & Lopez-Cruz 1997; Stanford, Eisenhardt & Dickinson 1998), which indicates that the bulk of stars in cluster elliptical galaxies form at the redshift $z \gtrsim$ 2.5-4 (Kodama et al. 1998).

However, we should also pay attention to the morphological evolution, since there have been direct evidence for cluster galaxy evolution. Butcher & Oemler (1984) found that fractions of blue galaxies are larger in the past, showing that cluster galaxies evolve from blue to red (so-called the Butcher-Oemler effect; Figure 4). In addition, morphological evolution of cluster galaxies have been observed. Dressler et al. (1997) studied 10 high redshift clusters at $z \sim 0.5$ and found that S0 fractions are much smaller than those in nearby clusters, suggesting that S0 galaxies are created

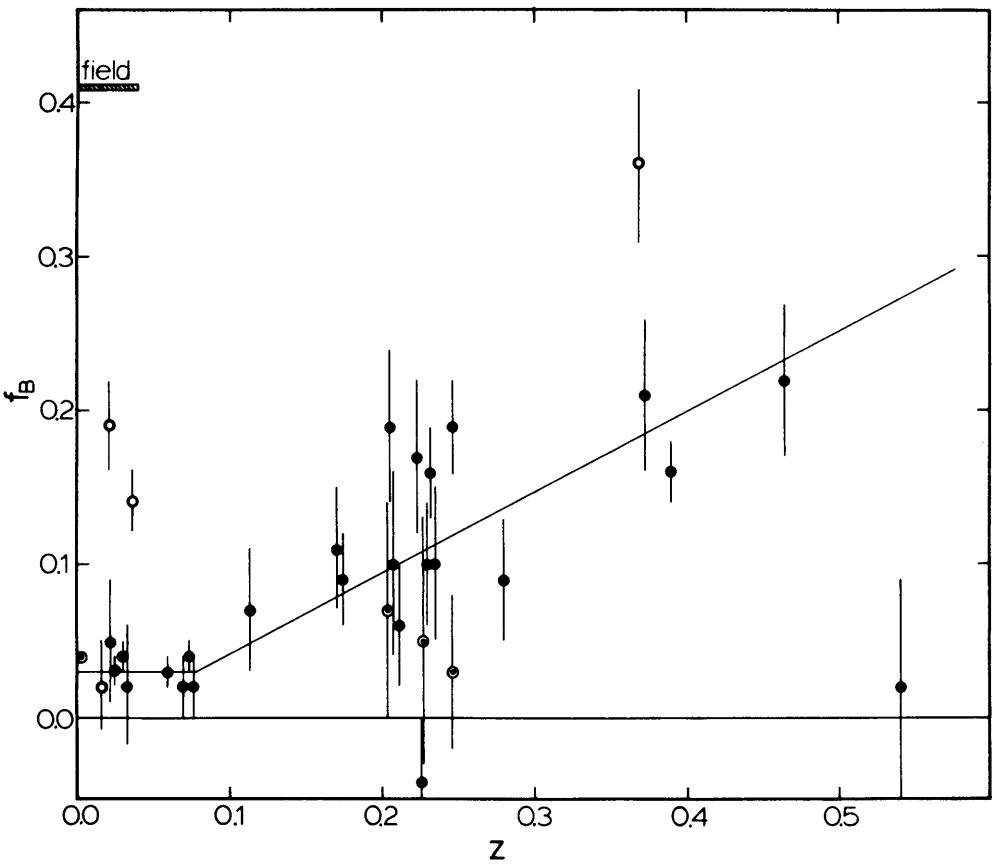

Figure 4: The Butcher-Oemler effect. Blue galaxy fraction v.s. redshift. Filled circles, compact clusters ($C \leq 0.40$); open circles, irregular clusters ($C \leq 0.35$); dotted circles, intermediate clusters ($0.35 \leq C \leq 0.40$) (Butcher & Oemler 1984).

fairly recently ($z \leq 0.5$; Figure 5). Therefore, these Butcher-Oemler effect and morphological evolution prevent us from comparing ellipticals at high-redshift with that at low-redshift. That is, the progenitors of the youngest low-redshift, cluster early-type galaxies significantly drop out of the sample at high redshift (Franx & Dokkum 1996; van Dokkum & Franx 2001); this problem is called 'progenitor bias', and van Dokkum & Franx (2001) estimates that $\sim 50\%$ of early-type galaxies were transformed from other galaxy types at $z < 1$, and their progenitor galaxies may have had roughly constant star formation rates prior to morphological transformation.

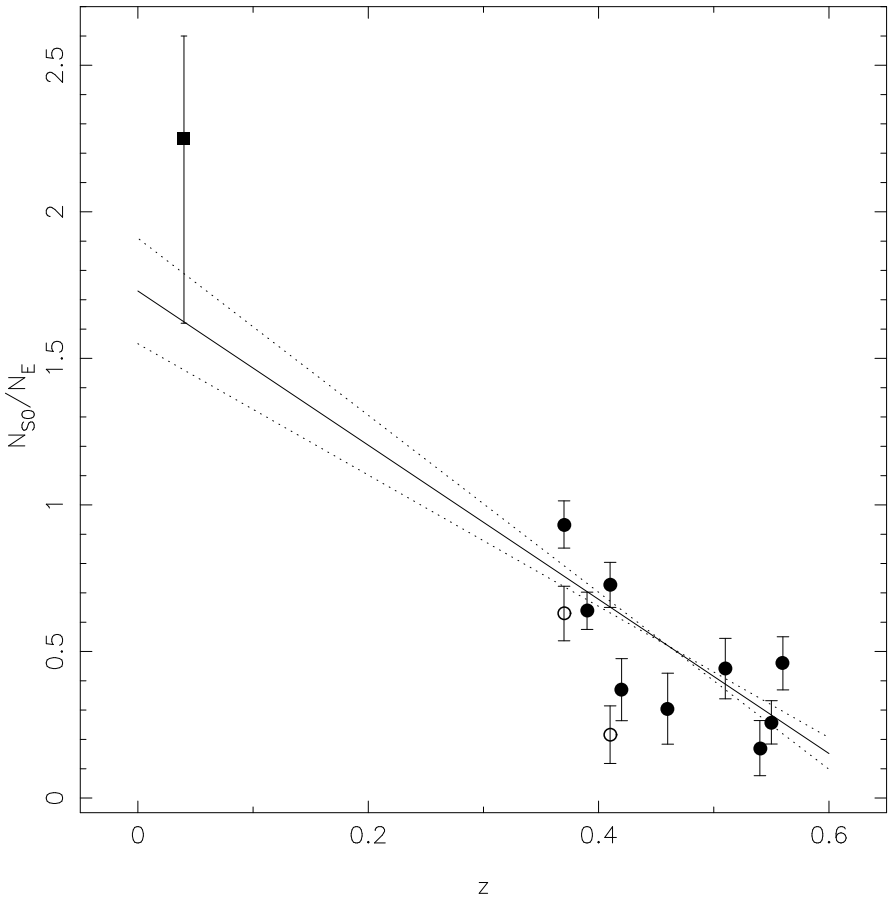

Figure 5: The S0/E fraction for clusters in the sample as a function of redshift. The open circles are the outer fields in A370 and Cl 0930+47, which are not used in the least-squares fit, shown with its 1 σ errors as the solid and dotted lines. The extrapolation of this linear relation to zero redshift approximately matches the value S0/E ~ 2, shown by the filled square, found for 11 clusters with $0.035 < z < 0.044$ of the D80 cluster sample (Dressler et al. 1997).

The evolution of field early-type galaxies is also now paid attention as the observational constraints. Kauffmann (1996) conclude that elliptical galaxies in the field are intrinsically different from cluster ellipticals in their merger model; these galaxies have undergone recent merging and star formation. Drory et al. (2001) found mass evolution of massive field galaxies at redshift $0.4 < z < 1.2$; the integrated stellar mass function is roughly constant for the lower mass limit, but it decreases with redshift for the higher mass limits. However, some authors (e.g., Schade et al. 1999; Brinchmann & Ellis 2000; Im et al. 2002) reported that no evolution of field elliptical galaxies found at least $z \lesssim 1$. Franceschini et al. (1998) investigated the properties of a complete K-band selected $z \lesssim 1.3$ sample of 35 elliptical and S0 galaxies brighter than $K = 20.15$mag in the Hubble Deep Field (HDF), found that HDF early-type galaxies are relatively young with the formation epochs spanning $1 \lesssim z \lesssim 4$. Moreover, the number of field red elliptical at high redshift is smaller than expected by the monolithic collapse hypothesis (Zepf 1997; Menanteau et al 1999; Barger et al. 1999).

A number of recent observations focus on high redshift $z \gtrsim 1$. Some of these high redshift observations have not detected enough objects to know whether they are clustered or not. Elston, Rieke & Rieke (1988, 1989) discoverd a new extragalactic population by deep K-band surveys, which exhibits extremely red in $R-K$ color but cannot be detected at R-band. These objects are called Extremely Red Objects (hererafter EROs). Stiavelli & Treu (2001) have classified 30 EROs based on morphology of HST/NICMOS images, finding that about 60% of them are consistent with ellipticals, and Daddi et al. (2000) reported that EROs are strongly clustered. Miyazaki et al. (2003) classified $z \gtrsim 1$ EROs with $R - K_s \leq 3.35$ (AB system) into passively evolving old galaxies (OGs) and dusty starburst galaxies (DSs), and the number density of OGs drops at $z \gtrsim 1.5$ by a factor of three or more. They also found that OGs have a wide range of colors at any redshift, suggesting not only that OGs cannot be reproduced by a single passive evolution model, but also that a significant fraction of OGs at $z \geq 0.8$ have a non-negligible amount of star formation. Cimatti et al. (1999) estimated that the masses of passively evolving EROs are intermediate $\sim 10^{11} M_{\odot}$ by their rest-frame K-band absolute magnitudes. The EROs at higher redshift are observed by the observation Infrared Array Camera (IRAC) on the Spitzer Space Telescope. Yan et al. (2004) selected IRAC-selected EROs (IEROs) with $1.6 \lesssim z \lesssim 2.9$, and found that most of them can be well fitted by a simple two-component model, where the primary component represents a massive, old population that dominates the strong IR emission, while the sec-

ondary component represents a low-amplitude, on-going star formation process that accounts for the weak optical fluxes. High redshift 'Lyman-break' galaxies (LBGs) with $z \sim 3$ in the Hubble Deep Field (HDF) can be identified by means of their very red $U-B$ colors. This red color is due to the fact that the Lyman continuum break at 912Å shifts into the terrestrial U wavelength band. Since the majority of spiral disks will not yet have formed at $z \sim 3$ it seems likely that most of the LBGs are young ellipticals, or precursors of present-day galactic bulges (van den Bergh 1998). The apparent size of LBGs at $z \sim 3$ is 0.2″ - 0.3″ in a half-light radius (Steidel et al. 1996), and Madau (1997) pointed out that the Lyman-break systems

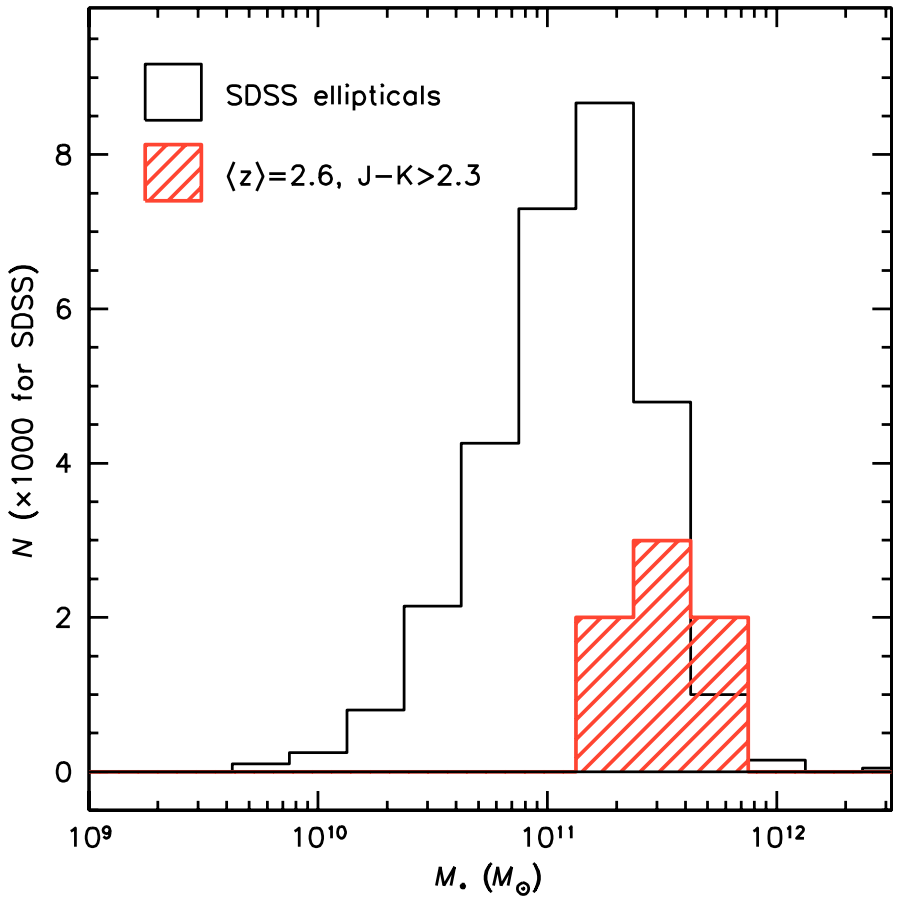

Figure 6: Comparison of the stellar masses (derived from SEDs) of the seven J_s-K_s selected galaxies (DRGs) discussed in the van Dokkum et al. (2004) to those of more than 29,000 galaxies in the SDSS (Padmanabhan et al. 2004). The red $z > 2$ galaxies have similar stellar masses as massive elliptical galaxies in the nearby universe (van Dokkum et al. 2004).

in the HDF are under-luminous relative to the expectations for young spheroidal systems. Papovich, Dickinson & Ferguson (2001) estimated that LBGs have minimum stellar masses $\sim 10^{10} M_{\odot}$. Ouchi et al. (2001) studied the clustering properties of about 1200 $z \sim 4$ LBGs from deep *BRi'* imaging data of a 618 arcmin^2 area in the SUBARU/XMM deep survey field, and found strong clustering. The Lyα emitters (LAEs) are identified by their redshifted Lyα emission with narrowband imaging (Cowie & Hu 1998; Hu & Cowie 1998). LAEs are high-z galaxies that have a relatively strong Lyα emission whise rest-frame EW is $\gtrsim 20$Å, and size of LAEs at $z = 2.4$ is as small as $\lesssim 0.1''$. Searchers of LAEs on targeted fields have found strong clustering of LAEs around QSOs (Campos et al. 1999), radio galaxies (Venemans et al. 2002), high-redshift clusters (Palunas Francis & Woodgate), and overdensities in the LBG distribution (Steidel et al. 2000). Ouchi et al. (2003) found that the distribution of $z = 4.86$ LAEs shows a large-density gradient with a scale of $\gtrsim 15'$, which would indicate the existence of a large-scale structure of LAEs. On the other hand, a massive galaxy population is also found. The distant red galaxies (DRGs) selected by $J_s - K_s > 2.3$ (Vega system) and $z > 2$ are observed, and followup near-infrared spectroscopy showed that they have already high stellar masses $\sim 2 \times 10^{11} M_{\odot}$ (van Dokkum et al. 2004) (Figure 6). The high redshift galaxies are identified by radio wavelength. The SCUBA 8-mJy survey, the largerst submm extragalactic mapping survey, captured dusty starbust galaxies with $z \gtrsim 2$. Ivison et al. (2002) reported $\sim 1000 M_{\odot}$ star formation rate (SFR) derived from radio and submm observations, and that at least 60% of the radio-detected optical/IR host galaxies display highly structured or distorted morphologies, suggestive of merging or interacting systems.

Thus, galaxy populations with high-z are growing diversity of the high-redshift "zoo". We summarized these observations (and estimations derived by them) from low-z to high-z in Figure 8. It becomes increasingly important to determine the relations between these populations, with the aim of establishing plausible evolutionary histories for nearby galaxies. We conformed that the Monolithic collapse hypothesis or Merger hypothesis solely cannot explain even low-z observations, and the high-z world also cannot be explained by such a way. If $z \gtrsim 2.5$-4 star burst galaxies are the progenitor of elliptical galaxies, it can be interpreted as initial gas-rich starbursts occurs mainly at $z \gtrsim 2.5$-4 predicted by Kodama et al. (1998), and the driven galactic winds induce the loss of gas from formed galaxies at $z \gtrsim 2.5$-4 as proposed in the monolithic collapse hypothesis. Even though the the monolithic collapse hypothesis models can reproduce the fundamental properties of ellipticals as long as we take a reliable initial condition of the protogalactic clouds, however,

we have not yet find the reason why the initial condition of the protogalactic clouds can be selected as required in the the monolithic collapse hypothesis. Therefore, we must consider alternative scenarios. More recently, hierarchical galaxy formation models in cold dark matter cosmologies have postulated that massive galaxies have complex assembly histories and were built up gradually through mergers and periods of star formation (White & Frenk 1991). The concept view of hierarchical galaxy formation scenario is shown in Figure 7. In the hierarchical scenario, the initial density perturbation in the early universe grows the small dark halos, i.e. small blobs of dark matter, and these dark halos are assembled into protogalaxies with star formation by gas cooling. While dark halos grow, merging of galaxies builds up larger galaxies. In these models properties such as mass, star formation rate, and morphology are transient, depending largely on the merger history and the time elapsed since the most recent merger (e.g., Kauffmann, White & Guiderdoni 1993; Kauffmann et al. 1999; Baugh et al. 1998; Meza et al 2003).

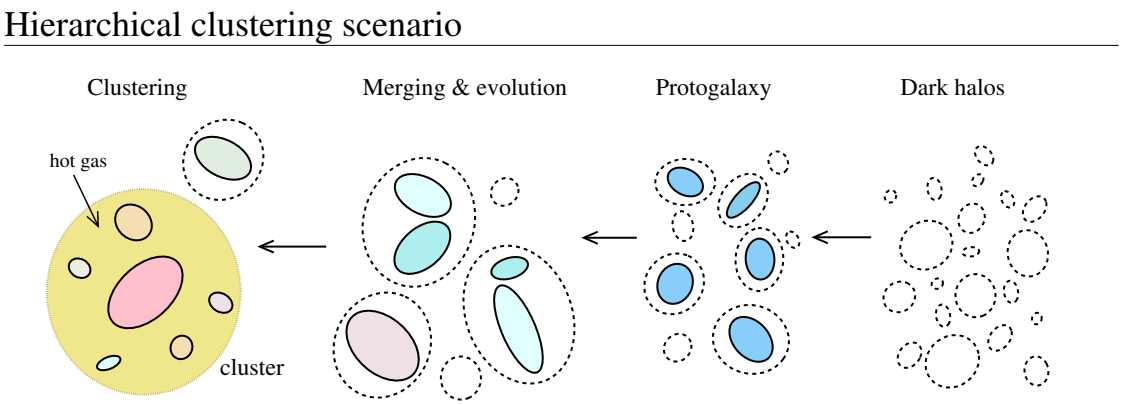

Figure 7: The concept view of the hierarchical galaxy formation models.

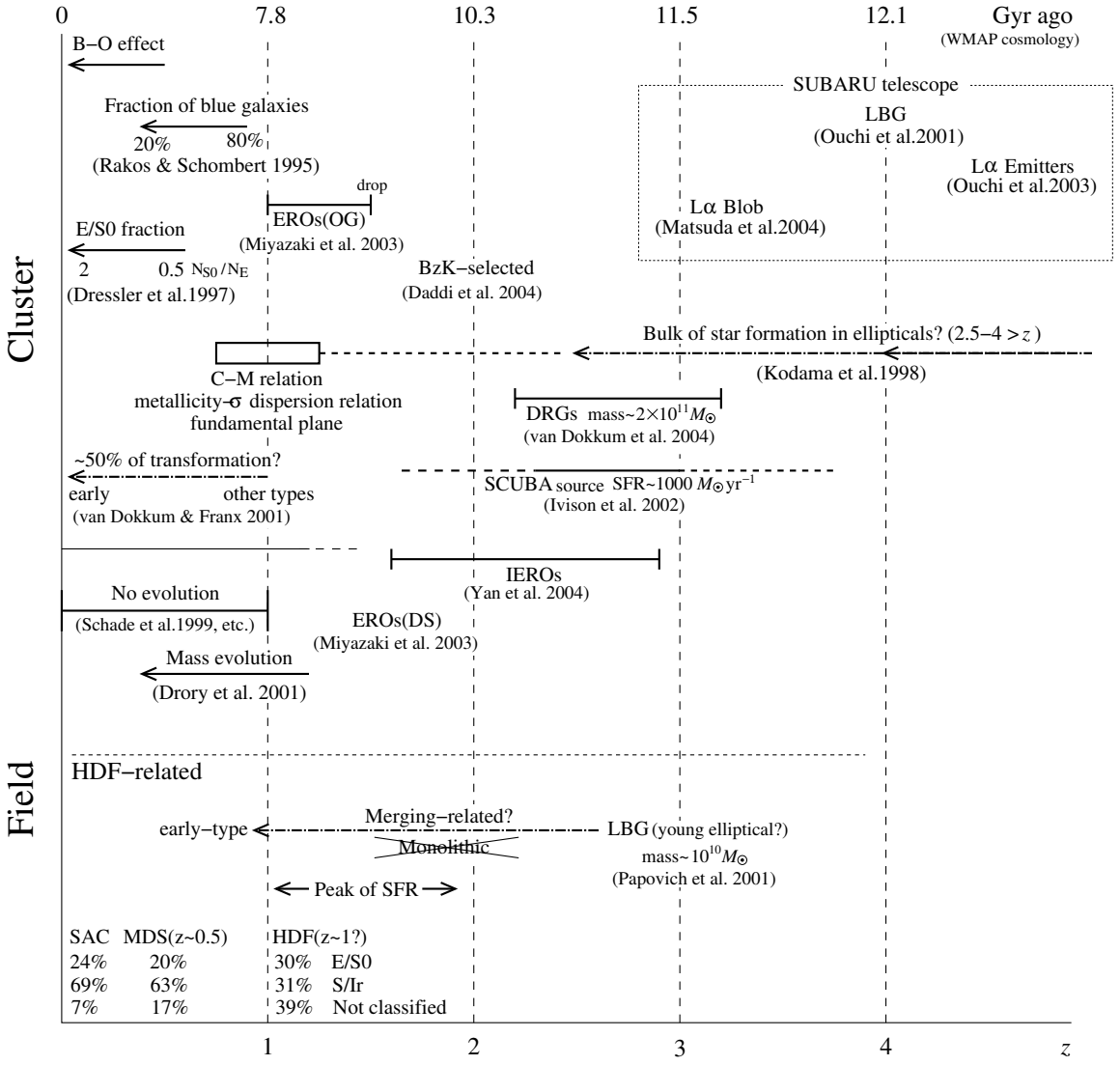

Figure 8: The overview of recent observational studies of cluster/field early-type (-related) galaxies with redshift z. The solid lines represent observational evidences, and dot-dashed lines show inferences. Galaxy populations with high-z are growing diversity of the high-redshift "zoo". The connections between high-z objects are almost uncertain.

1.2 E+A galaxies and its placement in galaxy evolution

Dressler & Gunn (1983, 1992) discovered galaxies with mysterious spectra while investigating high redshift cluster galaxies. These galaxies had strong Balmer absorption lines with no emission in [OII]. They are named "E+A" galaxies since their spectra looked like a superposition of that of elliptical galaxies (Mg_{5175}, Fe_{5270} and $Ca_{3934,3468}$ absorption lines) and that of A-type stars (Strong Balmer absorption). Since the lifetime of A-type stars is about 1 Gyr, the existence of strong Balmer absorption lines shows that these galaxies have experienced starburst within the last Gyr. However, they do not show any sign of on-going star formation as non-detection in [OII] emission line indicates. Therefore E+A galaxies are interpreted as a post-starburst galaxy, that is, a galaxy which has undergone a truncated starburst (Dressler & Gunn 1983, 1992; Couch & Sharples 1987; MacLaren, Ellis & Couch 1988; Newberry, Boroson & Kirshner 1990; Fabricant, McClintock & Bautz 1991; Abraham et al. 1996)

At first, "E+A" galaxies were found in cluster regions, both in low redshift clusters (Franx 1993; Caldwell et al. 1993; Caldwell & Rose 1997; Castander et al. 2001; Rose et al. 2001) and high redshift clusters (Sharples et al. 1985; Lavery & Henry 1986; Couch & Sharples 1987; Broadhurst, Ellis & Shanks 1988; Fabricant, McClintock & Bautz 1991; Belloni et al. 1995; Barger et al. 1996; Fisher et al. 1998; Morris et al. 1998; Couch et al. 1998; Dressler et al. 1999). Therefore, a cluster specific phenomenon was thought to be responsible for the violent star formation history of E+A galaxies. A ram-pressure stripping model (Spitzer & Baade 1951; Gunn & Gott 1972; Farouki & Shapiro 1980; Kent 1981; Abadi, Moore & Bower 1999; Fujita & Nagashima 1999; Quilis, Moore & Bower 2000; Fujita 2004; Fujita & Goto 2004) may first accelerate star formation of cluster galaxies and later turn it off as well as tides from the cluster potential (e.g., Fujita 2004). However, recent large surveys of the nearby universe found many E+A galaxies in the field regions (Goto 2003; Goto et al. 2003c; Quintero 2004). At the very least, it is clear that these E+A galaxies in the field regions cannot be explained by a physical mechanism that works in the cluster region. E+A galaxies have been often thought to be transition objects during the cluster galaxy evolution such as the Butcher-Oemler effect (e.g., Goto et al. 2003a), the morphology-density relation (e.g., Goto et al. 2003e), and the correlation between various properties of galaxies with the environment (e.g., Tanaka et al. 2004). However, explaining cluster galaxy evolution using E+A galaxies may not be realistic anymore.

One possible explanation for E+A phenomena is dust enshrouded star formation, where E+A galaxies are actually star-forming, but emission lines are invisible in optical wavelengths due to the heavy obscuration by dust. As a variant, Poggianti & Wu (2000) presented the selective dust extinction hypothesis, where dust extinction is dependent on stellar age since youngest stars inhabit very dusty star-forming HII regions while older stars have had time to migrate out of such dusty regions. If O, B-type stars in E+A galaxies are embedded in dusty regions and only A-type stars have long enough lifetimes ($\sim$1 Gyr) to move out from such regions, this scenario can naturally explain the E+A phenomena. A straightforward test for these scenario is to observe in radio wavelengths where the dust obscuration is negligible. At 20cm radio wavelengths, the synchrotron radiation from electrons accelerated by supernovae can be observed. Therefore, in the absence of a radio-loud active nucleus, the radio flux of a star-forming galaxy can be used to estimate its current massive star formation rate (SFR) (Condon 1992; Kennicutt 1998; Hopkins et al. 2003). Smail et al. (1999) performed such a radio observation and found that among 8 galaxies detected in radio, 5 galaxies have strong Balmer absorption with no detection in [OII]. They concluded that massive stars are currently forming in these 5 galaxies. Owen et al. (1999) investigated the radio properties of galaxies in a rich cluster at $z \sim 0.25$ (A2125) and found that optical line luminosities (e.g., Hα+[NII]) were often weaker than one would expect for the SFRs implied by the radio emission. Miller & Owen (2001) observed radio continua of 15 E+A galaxies and detected moderate levels of star formation in only 2 of them. Goto (2004) performed 20cm radio continuum observation of 36 E+A galaxies, and none of them are detected in 20cm, suggesting that E+A galaxies are not dusty-starburst galaxies.

Alternatively, galaxy-galaxy interaction has been known to trigger star formation in the pair of galaxies (Schweizer 1982; Lavery & Henry 1988; Liu & Kennicutt 1995a,b; Schweizer 1996; Nikolic, Cullen & Alexander 2004). Oegerle, Hill & Hoessel (1991) found a nearby E+A galaxy with a tidal tail feature. High resolution imaging of Hubble Space Telescope supported the galaxy-galaxy interaction scenario by identifying that some of post-starburst (E+A) galaxies in high redshift clusters show disturbed or interacting signatures (Couch et al. 1994, 1998; Dressler et al. 1994; Oemler, Dressler & Butcher 1997). Liu & Kennicutt (1995a,b) observed 40 merging/interacting systems and found that some of their spectra resemble E+A galaxies. Bekki, Shioya & Couch (2001) modeled galaxy-galaxy mergers with dust extinction, confirming that such systems can produce spectra with evolve into E+A spectra. Recently, Goto et al. (2003d) found that young E+A galaxies have 8 times more

companion galaxies within 50 kpc, providing a strong support for merger/interaction origin of E+A galaxies.

Thus, when we recognize that recent many studies indicate the evidences of merger/interaction origin of E+A galaxies, the E+A galaxies can become progenitors of early-type galaxies and important roles in galaxy formation scenario (see Figure 9). However, the two transitions, "from merger/interaction galaxy to E+A galaxy" and "from E+A galaxy to early-type galaxy", are still uncertain. One of the best way to ascertain the two transitions is the investigation of internal properties, such as age and metallicity gradients, of E+A galaxies along the evolutionary sequence. In addition, the questions — how much fraction of E/S0 galaxies in current universe underwent merging, and how old is their merger age? — are basic problems in the hierarchical clustering scenario. The investigations of E+A phase might find a clue to solution of these problems. How do E+A galaxies play their roles in the evolution scenario of E/S0 galaxies? If we can trace E+A's evolution, the methods which reveal E+A's evolution might be applied into post-E+A phase. However,

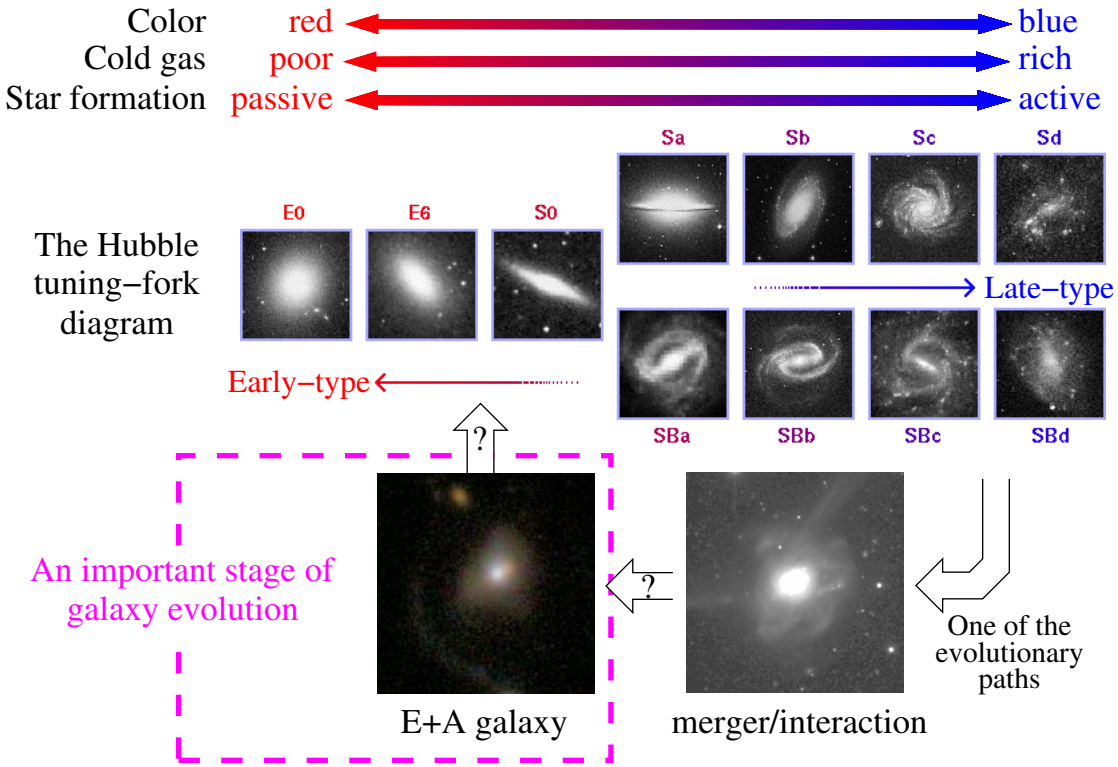

Figure 9: The placement of E+A in galaxy evolution.

we have not investigated E+A phase enough, to say nothing of post-E+A phase. Unfortunately, we have not obtained enough observational data of E+A galaxies to satisfy a statistical significance and investigate their evolutionary sequence since E+A galaxies were found. Because E+A galaxies are quite rare objects due to their very short phase (less than a Gyr).

The SDSS which is both imaging and redshift survey of 10,000 deg^2, provides us with the first opportunity to study E+A galaxies in a much large number. Currently, DR3 is released and its footprint area has attained 5,282 deg^2, and spectroscopic data of 374,767 galaxies with imaging data are publicly available. However, astronomers tend to keep SDSS imaging data (i.e. SDSS photometry) at a respectful distance, since handling imaging data requires contrivances due to its own peculiar character. Needless to say, it is often important to measure observational quantities by ourself to fulfill our scientific needs. In this thesis, I focus on spatial properties of E+A galaxies, and contrive methods of handling SDSS imaging data to make the best use of them. I then try to trace the evolutionary sequence of E+A galaxies to ascertain the two transitions, "from merger/interaction galaxy to E+A galaxy" and "from E+A galaxy to early-type galaxy", using two-dimensional (2D) color and radial color gradients.

Fortunately, I obtained new results in return for my effort, and I stress that this thesis work is epoch-making at the following points:

- Use of higher purity of E+A galaxies in huge SDSS sample.
- Discovery of irregular morphologies in 2D colormap with SDSS imaging data.
- Discovery of substantial number of E+A galaxies with a positive slope (bluer towards the center) of radial color gradient.
- Discovery of tight correlation between E+A's radial color gradients and other photometric/spectroscopic observational quantities such as color and 4000Å break.
- Trace of E+A's spatial evolution, i.e., color gradients and 2D colormaps, using comparison to SED models.

The pioneering work which I should emphasise is *the trace of E+A's spatial properties along the evolutionary sequence using SDSS imaging data*. The contrivances of handling SDSS imaging data are described in section 2.5, and the main study of this thesis and its conclusions are presented in section 3 and section 4, respectively.

2 The Sloan Digital Sky Survey

2.1 The Sloan Digital Sky Survey

The Sloan Digital Sky Survey (SDSS, York et al. 2000; Early Data Release, Stoughton et al. 2002, hereafter EDR; First Data Release, Abazajian et al. 2003, hereafter DR1; Second Data Release, Abazajian et al. 2004, hereafter DR2) is a project for both an imaging and spectroscopic surveys. The SDSS project began the operation in November 2000 using a dedicated 2.5-m telescope located at Apache Point Observatory in New Mexico, USA (Figure 10). The telescope is used for both imaging and spectroscopy, and its optical design is based on a modified f/5.0 Ritchy-Chretien with a large secondary and two corrector lenses. The field of view of the telescope is a wide (3°; equal to about 30 full moons) and essentially distortion-free. Both imaging and spectroscopic surveys will be carry out to cover the region of $\sim\pi$ steradians centered on the north Galactic pole. The imaging survey obtains images of 10,000 deg^2 of the sky in five optical bands (u,g,r,i and z; Fukugita et al. 1996). The spectroscopic survey observes one million galaxies uniformly selected from the data of imaging survey.

We use this excellent data set to grapple with the long standing E+A problems. In this chapter, we summaries the design and data products of the SDSS and our method and tools for SDSS data handling.

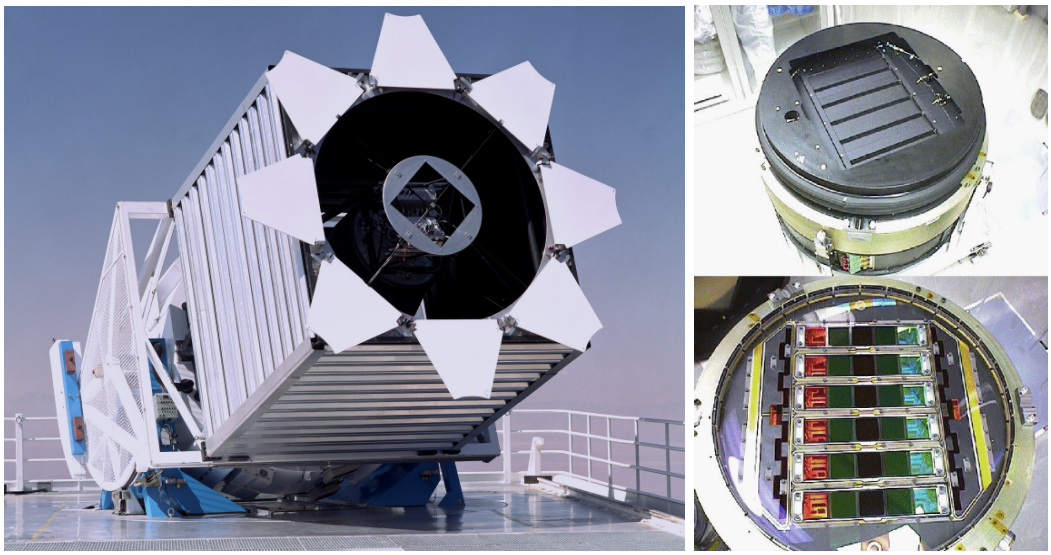

Figure 10: SDSS 2.5-meter telescope (*left*) and imaging camera (*right*). The five broad-band filters are aligned in order of *riuzg* (SDSS Web site).

2.2 The SDSS Imaging Survey

The SDSS imaging survey will obtain the image of 10,000 square degrees to a depth of $g \sim 23$ mag with effective wavelength of [3561Å, 4676Å, 6176Å, 7494Å and 8873Å] (u,g,r,i and z) spanning from the atmospheric cutoff at 300nm to the limit of sensitivity of CCD at 1100nm (Fukugita et al. 1996). This dedicated imaging camera consists of a mosaic of 30 2048×2048 SITe CCDs with 24μm pixels (See Gunn et al. (1998) for details). The camera has a resolusion of 0.396″ per pixel on the sky and observes the sky through five broad-band filters(u,g,r,i and z). The response functions are displayed in Figure 11. The limiting magnitude (5σ detection in 1″ seeing limits) of point sources are 22.3, 23.3, 23.1, 22.3 and 20.8 in the u,g,r,i and z filters, respectively, at airmass of 1.4. The camera has additional 22 CCDs (having 2048×400 pixels each) with neutral density filters that saturate at 8 mag (main CCDs saturate at ∼14 mag). The photometric calibration is carried out using separate 20" photometric telescope having a single-CCD camera and SDSS filters (Uomoto et al. 2003). This photometric telescope is located near the SDSS telescope.

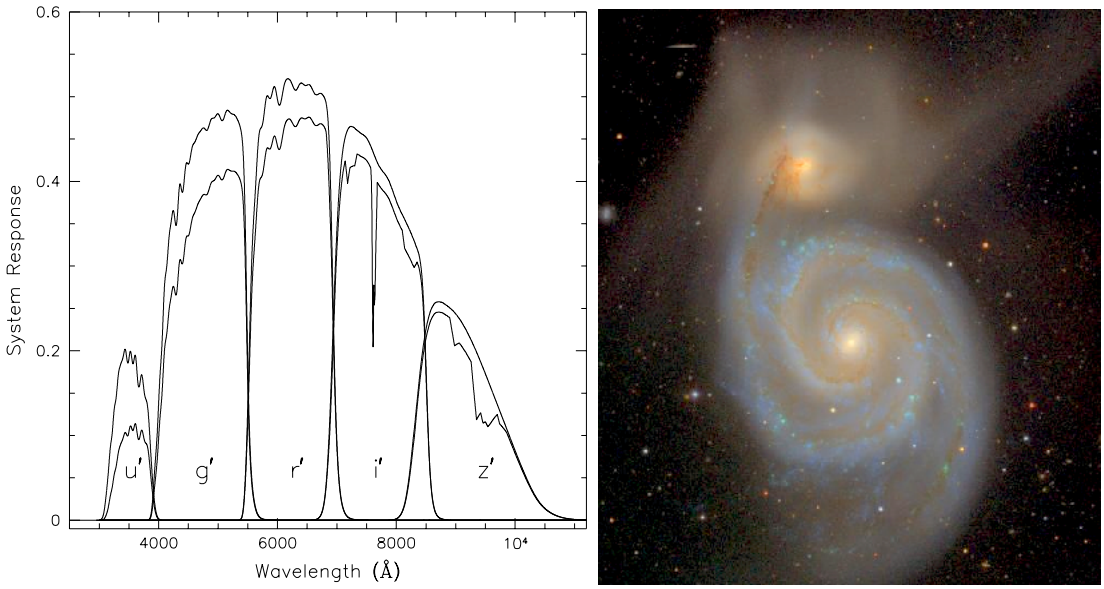

Figure 11: The response of SDSS photometric system as a function of wavelength (*left*; Fukugita et al. (1996)) and the M51 Whirlpool Galaxy observed with the SDSS imaging camera (*right*; SDSS Web site). The upper response curves indicate the response function without atmospheric extinction; the lower curves include extinction when observed at a typical altitude of 56″.

The Imaging survey is performed using Time Delay and Integrate (TDI) mode. The telescope is basically driven along a great circle on the sky so that objects pass directly along a column of CCDs. This strategy allows simultaneous observations in five passbands and enables very efficient survey. An object spends 5.7 mins to pass the entire CCD array. The net integration time per filter is 54.1 sec. We also show the M51 Whirlpool Galaxy in Figure 11, one of representative bright astronomical objects observed with the SDSS camera.

Figure 12 shows the location of imaging survey in the sky. To minimize Galactic foreground extinction, the area of northern survey is centered near the North Galactic Pole. It lies within a nearly elliptical shape 130° E-W by 110° N-S. All scans are conducted along great circles in order to minimize the transit time differences across the camera array. In the northern survey regions, there are 45 great circles (stripes) separated by 2.5°. In addition, three non-contiguous stripes in the Southern Galactic Hemisphere are observed, at declinations of 0°, 15° and -10°, when the northern sky

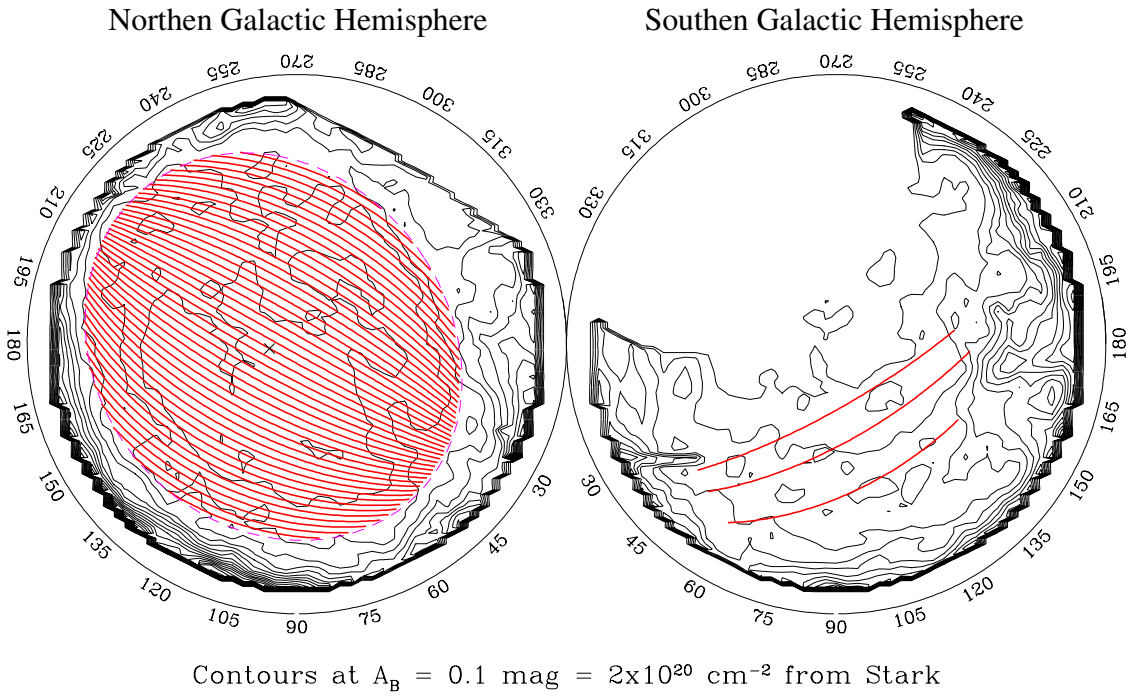

Figure 12: The location of the strips for imaging survey plotted in a polar projection for the North (*left*) and South (*right*) Galactic hemispheres (York et al. 2000). The contours show the amount of reddening due to extinction of dust in our Galaxy. Each solid line indicates a 2.5° wide rectangular region called *stripe*. The SDSS camera observes a stripe in two nights.

is unobservable (during the fall season). Each stripe is scanned twice with an offset perpendicular to the scan direction so that the photometric columns are interlaced. A completed stripe slightly exceeds 2.5° in width. This small amount of overlap allows mis-stacking of telescope and provides multiple observations of some fraction of the sky for purposes of quality assurance. Total length of 45 northern stripes will require 650 hours (minimum) of pristine photometric and seeing conditions to scan at a sidereal rate.

2.3 The SDSS Spectroscopic Survey

After selecting targets from the photometric catalog created from the data of imaging survey, the SDSS project observes 10^6 spectra of bright galaxies to the depth of

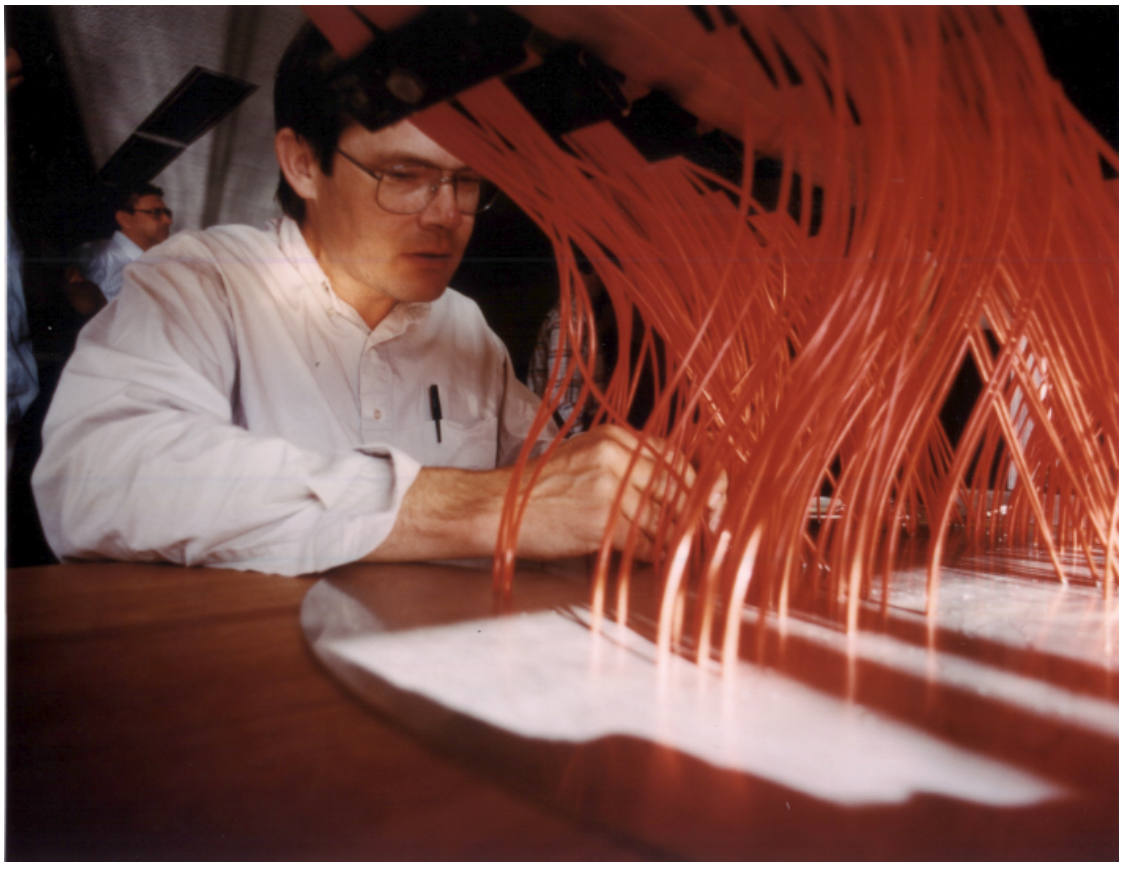

Figure 13: Astrophysicist Rich Kron, of the University of Chicago and Fermilab, inserts fibers into a pre-drilled "plug-plate". This part is unique spectrographic system of SDSS to determine the distances to objects (SDSS Web site).

$r \sim 17.77$ mag with median redshift of $z \sim 0.1$ and 10^5 brightest quasars to $i \sim 20$ mag.

640 spectra are observed at a time using a pair of double fiber-fed spectrographs shown in Figure 13. The fiber has $3''$ (0.2 mm on the plug-plate) of diameter, and adjacent fibers cannot be located more closely than $55''$ on the sky. The wavelength coverage of the spectrographs has continuous from about 3800Å to 9200Å, and the resolution of wavelength ($\lambda/\delta\lambda$) is 1800. The spectrograph has a throughput better than 25% over 4000Å to 8000Å excluding the loss due to the telescope and atmosphere.

Samples of galaxies are selected from the objects classified as "extended". The sample of main galaxies consists of ∼900,000 objects with $r < 17.77$. This limit of magnitudewas chosen to satisfy the target density of 90 objects per square degree. The SDSS spectroscopy also applies a surface brightness limit at $\mu < 24.5$ mag arcsec^{-2}, in order not to waste fibers on galaxies too faint to observe. This cut of surface brightness eliminates only 0.1% of galaxies that would otherwise be targeted for observation. See Strauss et al. (2002) for details of the target selection of main galaxies.

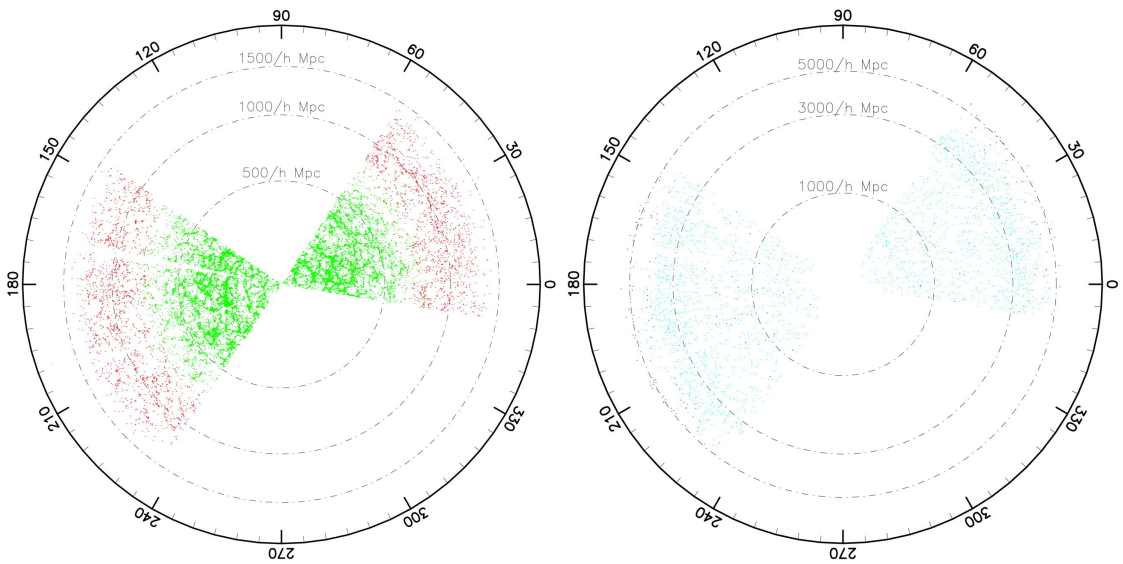

Figure 14: Pie diagram of main galaxies (*left,green*), LRGs (*left,red*), and the main quasars (*right,green*) and the high-redshift quasars (*right,blue*) with spectra in the EDR. The annuli are labeled with the comoving distance (Stoughton et al. 2002).

Additional $\sim$100,000 luminous red galaxies (LRG) are observed in the spectroscopic survey. The redshift of LRGs can be well measured using the SDSS spectrograph to $r \sim 19.5$ mag due to their intrinsic brightness and their strong absorption lines caused by high metallicity. These properties are often found in galaxies located at the dynamical centers of clusters. For these galaxies, reasonably accurate ($\Delta z \sim 0.03$) photometric redshifts can be determined. See Eisenstein et al. (2001) for more details of the target selection of LRGs. In Figure 14, we show example redshift distributions of the SDSS EDR.

The candidates of 150,000 quasars are selected by the cutout from multi-color space (Richards et al. 2002) and by identifying sources using FIRST radio catalog (Becker, White & Helfand 1995). Within most of their redshift range, the *ugriz* colors of quasars are quite distinct from those of the vastly more numerous stars (Fan 1999). Among point sources, quasar candidates are selected for spectroscopic observations as outliers from the stellar locus (Krisciunas et al. 1998) in color-color space. The SDSS plans to compile a sample of quasars brighter than $i \sim 19$ at $z < 3$; at redshift between 3 and 5.2, the limiting magnitude will be $i \sim 20$. The point sources brighter than $i \sim 20$ identified as FIRST sources are also selected. It is estimated that $\sim$65% of quasar candidates are genuine quasars based on a result of commissioning data, and the completeness of $\sim$90% is shown by comparison with samples of known quasars. This sample will larger than any existing quasar catalogs, and will be indispensable for quasar luminosity functions, evolution and clustering studies.

In addition, the SDSS spectroscopic survey also observes many thousands of stars and various serendipitous targets when remaining fibers are available.

In this thesis work, we mainly use a quite small subsample of the main galaxy sample.

2.4 Morphological Classification of Galaxies in SDSS

Morphological classification in the Hubble sequence (Sandage 1961) still serves as an important quantity that represents the basic features of galaxies, and is probably related to their formation and evolution histories. While the Hubble classification is based on the visual inspection of images of galaxies, and therefore necessarily involves subjective elements, it provides a basis for many extragalactic studies, such as Morphology-Density relation (e.g., Dressler 1980), Luminosity function (e.g., Binggeli, Sandage & Tammann 1988) and Butcher-Oemler effect (e.g., Dressler et

al. 1994).

With the advancement of automated digitized galaxy surveys, it is highly desirable to develop a fast, automated method of morphological classification based on objective quantities and applicable to large quantity of data, without losing the accuracy of the traditional visual classification. However, we have currently no method which satisfy such conditions. Therefore, SDSS catalog does not provide reliable parameters which represent morphological classification despite of their advanced automated photometric pipline. Focusing on morphological classification with imaging data, there are the two typical approaches, the use of artificial neural networks (Burda & Feitzinger 1992; Storrie-Lombardi et al. 1992; Serra-Ricart et al. 1993; Naim et al. 1995; Odewahn et al. 2002; Ball et al. 2004), and characterizations with simple surface photometric parameters (Doi, Fukugita & Okamura 1993; Abraham et al. 1994).

If we follow the latter method, the relation between the parameters and the classification can be easily understood. The simplest indicator often used in the literature is the parameter that characterizes the concentration of light towards the center of galaxies (Morgan 1958). In the case of SDSS catalog, Shimasaku et al. (2001) showed that we can use the concentration index derived from Petrosian half and 90% flux radius as a morphological parameter with $\sim 80\%$ of completeness.

We reconsidered the performance with the concentration parameter in the standard Petrosian scheme of flux definition. In particular, we examine cases where the classification fails. We employ an elliptical definition of Petrosian radii, as in Doi et al. (1993) and Abraham et al. (1996) for isophotal and aperture fluxes, and examine whether the success rate improves in comparison to the circular definition.

We also devised the method which use textures in the galaxy images to aid classification. The motivation for this approach is that, in visual classification, we mainly resort to surface brightness textures, such as properties of spiral arms, clumpiness, and HII regions, in addition to the concentration of light towards the center. The only work that we are aware of that discusses texture as a classifier is that by Naim, Ratnatunga & Griffiths (1997) who proposed "blobbiness", "isophotal center displacement" and "skeleton ratio", which correspond to roughness, global asymmetries and more localized structure, respectively. These parameters certainly correlate with morphologies and may be useful for classification, but our own tests employing these parameters show that they do not enhance the success rate of the morphological classification. We then introduce a new texture parameter, in a manner close to the way we carry out visual classification. We focus on the texture

seen in an outskirt of the intensity profile. The flux fluctuations are computed along the elliptic circumference; this characterizes the departure from a smooth surface profile of the galaxy. We define the "coarseness" parameter which, roughly speaking, is the ratio of the range of fluctuations in surface brightness along the elliptic circumference to the full dynamic range of surface brightness of the galaxy.

In this subsection, with reconsideration of concentration parameter, we introduce the new texture parameter to reader. We studied the performance of the two parameters, and their combined use, for CCD images given in the SDSS First Data Release sample (DR1, Abazajian et al. 2003), taking the visually classified catalog of galaxies constructed from the EDR sample (Fukugita et al. in preparation) as the reference. This catalog is based on the SDSS-EDR sample but contains some galaxies originating in commissioning data, and positional matching is performed to identify galaxies in the Fukugita et al. catalog with those in DR1, since the deblending of EDR presents a problem for large galaxies. The morphological catalog contains 1875 galaxies brighter than $m_{\rm P}(r^*\text{-band})=15.9$ mag [1] (after extinction corrections); this number is reduced to 1817 by dropping 58 galaxies originating in commissioning data after positional matching. 23 galaxies are morphologically disturbed in 1817 galaxies and are given $T=-1$ (unclassified); these galaxies are removed from our consideration. The galaxies are classified into 13 morphological types from $T=0$ (corresponding to E in the Hubble type) to 6 (Im) allowing for half integer classes. In this paper, we mostly refer to $T=0.5$ and 1 as S0, 1.5 and 2 as Sa, ..., 5.5 and 6 as Im.

The r-band image is used to compute the concentration index. We use the original image without rescaling, since the seeing effects on the concentration index are small for our bright galaxy sample. The coarseness parameter is computed using the g-band image because this filter is generally thought to be more sensitive to textures than r data (Our experiments have shown, however, that the use of the r-band image leads to very little difference in classification). The reference size $a_{90}^{\rm ref}$ was set at $a_{90}^{\rm ref}$ to be 25 pixels ($=10''$) (Gunn et al. 1998) as a test; we discarded galaxies with a_{90} smaller than this size. This selection leaves the 1421 galaxies in our sample, primarily removing galaxies of earlier types. Galaxies of later types (including irregular galaxies) generally have larger size in a magnitude-limited sample, and are little affected by the size cutoff.

For simplicity of our analysis we fix FWHM of the seeing at 3.53 pixels ($1.40''$;

[1] The notation r^* means the preliminary nature of early photometric calibration of commissioning data. See Shimasaku et al. (2001).

the median of our sample) and $\varsigma_{\rm sky}$ at 4.0 counts for rescaling, because our sample contains bright galaxies whose a_{90} is near $a_{90}^{\rm ref}$ and variations of seeing and $\varsigma_{\rm sky}$ are sufficiently small that they do not seriously affect the analysis, (Meanwhile, too large a_{90} of some of our galaxies affects the results of the coarseness parameter according to our investigation, so we rescale images). For a more elaborate analysis or for galaxies of small sizes or fainter galaxies, one should take account of variations of these quantities from image to image for better performance.

This study is submitted to Astronomical Journal (2004).

2.4.1 Concentration index — improvements by author

The SDSS uses the Petrosian flux to define photometric quantities. We consider a concentration index for elliptical apertures using Petrosian quantities. The intensity-weighted second-order moments are defined in the SDSS photometric pipeline (hereafter PHOTO; Lupton 1996; Lupton et al. 2001) by

$$M_{xx} \equiv \langle x^2/r^2 \rangle,\ M_{xy} \equiv \langle xy/r^2 \rangle,\ M_{yy} \equiv \langle y^2/r^2 \rangle. \tag{1}$$

If the major and minor axes of the ellipse lie along the x and y axes, the axis ratio $\alpha = b/a$ is calculated as

$$\alpha = \frac{M_{yy}}{M_{xx}}. \tag{2}$$

because

$$M_{xx} = \frac{1}{1+\alpha}, \quad M_{xy} = 0, \quad M_{yy} = \frac{\alpha}{1+\alpha}. \tag{3}$$

In general, we rotate the image to account for the position angle ϕ from (x', y') to (x, y) to align the galaxy image along the axes:

$$\begin{aligned} x' &= x\cos\phi - y\sin\phi \\ y' &= x\sin\phi + y\cos\phi. \end{aligned} \tag{4}$$

The Stokes parameters U and Q are calculated as

$$U/2 \equiv M_{x'y'} = (M_{xx} - M_{yy})\sin\phi\cos\phi = \frac{1-\alpha}{1+\alpha}\cdot\frac{\sin 2\phi}{2} \tag{5}$$

$$Q \equiv M_{x'x'} - M_{y'y'} = \frac{1-\alpha}{1+\alpha}\cos 2\phi, \tag{6}$$

where $\phi = 1/2\ \tan^{-1}(U/Q)$. The axis ratio is $\alpha = (1+P)/(1-P)$ with $P = \sqrt{(U^2+Q^2)}$. U and Q are evaluated in PHOTO and cataloged in the SDSS data releases.

To calculate the concentration index C_e for the ellipse, we consider the area $A_e(a)$ of the ellipse of the semi-major axis a and axis ratio α, and the integrated flux $F_e(a)$ within $A_e(a)$. We define the Petrosian semi-major axis $a_{\rm P}$ for a given η as

$$\eta = \frac{\{F_e(1.25a_{\rm P}) - F_e(0.8a_{\rm P})\}/\{A_e(1.25a_{\rm P}) - A_e(0.8a_{\rm P})\}}{F_e(a_{\rm P})/A_e(a_{\rm P})}, \tag{7}$$

where we take η=0.2, and the elliptical Petrosian flux $F_{\rm P}$ as

$$F_{\rm P} = F_e(ka_{\rm P}) \tag{8}$$

with k set equal to 2, following the SDSS definition (Strauss et al. 2002)

The Petrosian half-light and 90%-light semi-major axes a_{50}, a_{90} are defined in such a way that the flux in the elliptical apertures of these semi-major axes is 50% and 90% of the elliptical Petrosian flux:

$$F_e(a_{50}) = 0.5F_{\rm P}, \quad F_e(a_{90}) = 0.9F_{\rm P} \ . \tag{9}$$

We define our concentration index C_e by

$$C_e = a_{50}/a_{90} \ . \tag{10}$$

In Figure 15 we plot the two concentration indices against visual morphological type index T, employing (a) conventional circular apertures (C), and (b) C_e defined with elliptical apertures. Galaxies that follow de Vaucouleurs' law give C=C_e=0.29 and those with the exponential profile give 0.44.

The Spearman correlation coefficient with the use of C, r=0.781 increases to r=0.820 with C_e. Several significant improvements are obtained by the use of an elliptical aperture (C_e), compared with the original circular aperture (C): For example, those galaxies with $3 \leq T \leq 3.5$ and $0.3 \leq C \leq 0.45$ in panel (a) (under the dotted line) have much larger value of C_e in panel (b). These are edge-on galaxies redundantly classified using the circular aperture in C, but correctly classified as less concentrated galaxies by C_e using the elliptical aperture. A similar improvement is also seen for Sa galaxies (T=2).

Figure 16 presents the concentration index against the axis ratio. The regression lines are drawn for morphological classes of galaxies Sb, Sc and Sdm. The lines obtained by regression on samples of different galaxy types in panel (a), which are based on C, are significantly tilted with respect to the axis ratio. The concentration indices of late-type galaxies, when defined with circular apertures, drop to the values of earlier types when they are largely inclined. That is, edge-on spirals give

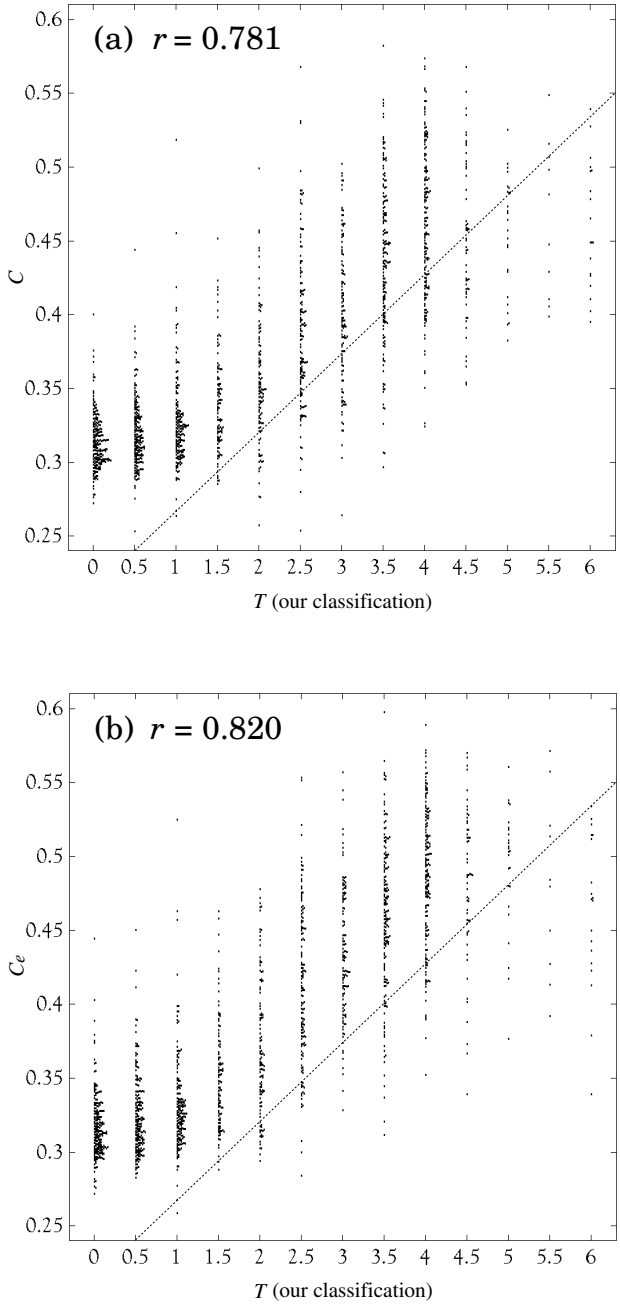

Figure 15: Inverse concentration indices of 1421 galaxies plotted against morphology T: (a) with the standard circular apertures used in the SDSS DR1 catalog; (b) with elliptical apertures defined in the text. To show the distribution of the points more clearly, some of the dots are shifted to the right, if needed, to avoid overlaps. The number on the top of each panel is a linear correlation coefficient. The dotted lines are arbitrarily placed in the same position to show differences under the lines between (a) and (b).

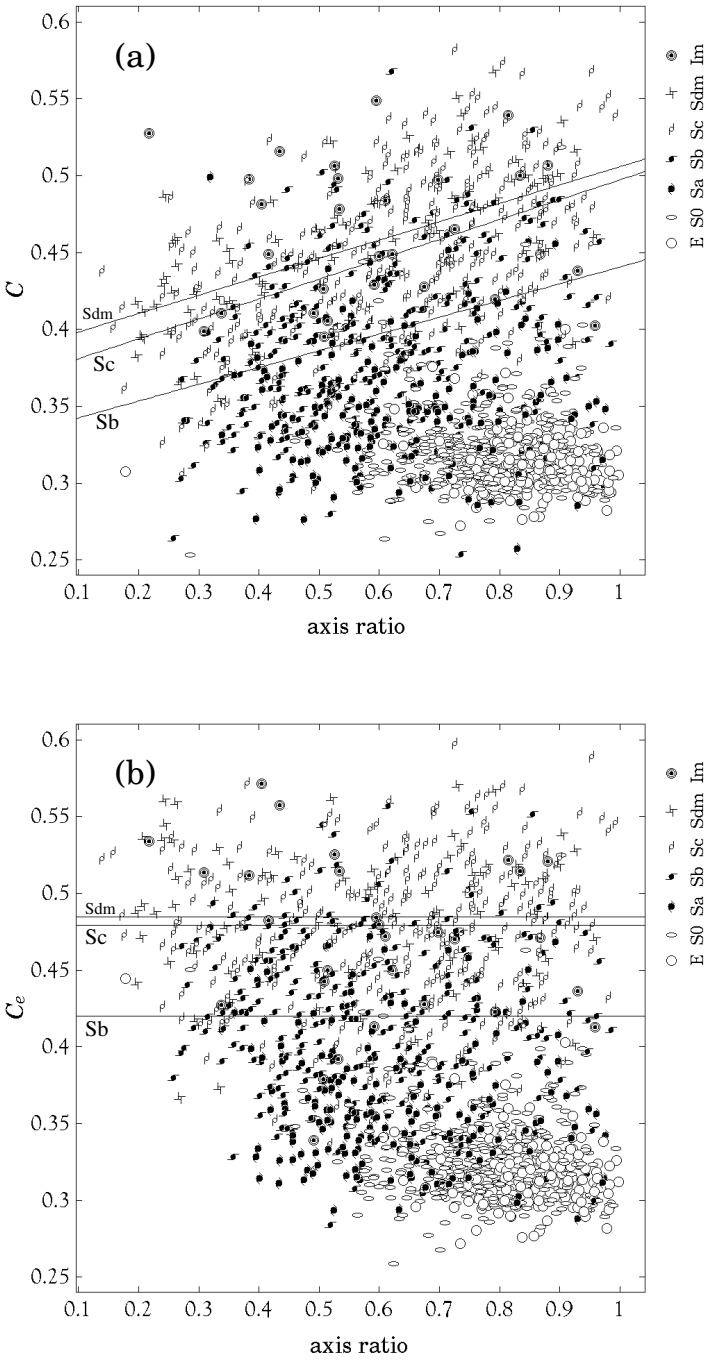

Figure 16: Inverse concentration indices plotted against axis ratio α. Each symbol indicates visual classification T as specified in the legend, and the straight lines are the linear regression lines for types Sb, Sc and Sdm. (a) Figure with circular apertures; (b) with elliptical apertures.

an anomalously high concentration of light if defined with circular apertures; the morphological classifications that use only C have significant contaminants.

Figure 16(b), using C_e, shows that elliptical apertures remedy this problem. We observe little tilt of the regression lines, suggesting that C_e works better to classify morphologies than C; the effect of inclination is removed with the use of elliptical apertures.

2.4.2 The coarseness parameter — a new parameter by author

We consider successive elliptical annuli from $a = a_{10}$ outwards to a_{90}, where a_f is defined by $F_e(a_{100f}) = fF_{\rm P}$ as in (9). We assume that each elliptical annulus has the same position angle and is congruent. The position angle ϕ and the axis ratio α are calculated in the same way as in the previous section. We define the 'equivalent distance' d from the center of the galaxy to a pixel at (x, y), after rotation of the original position by (4), by

$$d = \sqrt{x^2 + (y/\alpha)^2}. \tag{11}$$

We then divide the area sandwiched by the two ellipses specified by a_{10} and a_{90} into $n_{\rm max}$ annuli, as specified in what follows: We calculate d of each pixel contained in the annulus between a_{10} and a_{90}, and place the pixels in ascending order with respect to d as

$$\underbrace{d_{1_1}, d_{1_2}, \cdots, d_{1_{\mathcal{N}_1}}}_{\text{1st annulus}} \ , \ \underbrace{d_{2_1}, d_{2_2}, \cdots, d_{2_{\mathcal{N}_2}}}_{\text{2nd annulus}} \ , \ \underbrace{d_{3_1}, d_{3_2}, \cdots, d_{3_{\mathcal{N}_3}}}_{\text{3rd annulus}} \ , \ \cdots \ , \quad \cdots \tag{12}$$

where the number of pixels contained in the n-th annulus $\mathcal{N}_n$ is calculated by the equivalent distance to the innermost point in the n-th annulus, d_{n_1}:

$$\mathcal{N}_n = 2\pi\alpha d_{n_1} \ , \tag{13}$$

where α is the axis ratio defined in the previous section. The last annulus, which terminates at a_{90}, does not generally satisfy the condition (13). We show the actual algorithm which satisfies equation (12) and (13) as follows:

1) Focus on 1st d, d_{1_1}.
2) Calculate $\mathcal{N}_1$ by equation (13), $\mathcal{N}_1 = 2\pi\alpha d_{1_1}$.
3) When $\mathcal{N}_1$=6 for an example, the member of 1st annulus is

$$d_{1_1}, d_{1_2}, d_{1_3}, d_{1_4}, d_{1_5} \text{ and } d_{1_6}.$$

4) d_{2_1} is automatically determined by d_{1_6} (d_{2_1} is next to d_{1_6}. That is, 7th d).

5) Focus on 7th d, d_{2_1}.

6) Calculate $\mathcal{N}_2$ by equation (13), $\mathcal{N}_2 = 2\pi\alpha d_{2_1} \cdots$

Let us take the n-th annulus, and consider the flux distribution. We define the 90%- and 10%-tiles of the flux distribution as $I_{90}(n)$ and $I_{10}(n)$ in the n-th annulus, respectively (See inlaid histogram in the top left of Figure 17), and the range of the two values as

$$I_{\rm range}(n) = I_{90}(n) - I_{10}(n) \ . \tag{14}$$

We define the mean of $I_{\rm range}(n)$ over the annuli between $n_{\rm begin}$ and $n_{\rm max}$, as

$$\langle I_{\rm range} \rangle = \frac{1}{n_{\rm max} - (n_{\rm begin} - 1)} \sum_{n=n_{\rm begin}}^{n_{\rm max}} I_{\rm range}(n), \tag{15}$$

where the mean is taken from the $n_{\rm begin}$-th to the outermost annulus, some inner annuli being excluded. This exclusion of the inner annuli is made to enhance the visibility of the texture, which is usually more manifest in outer regions for late-type galaxies. From trial and error, we adopted $n_{\rm begin} = [n_{\rm max}/3]$ with the floor function as the best value for the performance of classification.

To further enhance the signal, we subtract the contribution of the sky noise to $\langle I_{\rm range} \rangle$,

$$I_{\rm signal} = \sqrt{\langle I_{\rm range} \rangle^2 - (2.56 \cdot \varsigma_{\rm sky})^2} \ , \tag{16}$$

where $\varsigma_{\rm sky}$ denotes the rms of the sky noise. We multiply the sky noise by a factor of 2.56 so that its strength corresponds to the range between 90 and 10%-tiles in the Gaussian distribution to match our definition of $I_{\rm range}$. With this choice, $I_{\rm signal}$ vanishes when the frame does not contain objects, i.e., contains sky noise only. This subtraction enhances the performance of the classifier.

We then divide $I_{\rm signal}$ by the dynamic range of the image ΔI, i.e.,

$$Y = \frac{I_{\rm signal}}{\Delta I} \ . \tag{17}$$

The ΔI is defined by

$$\Delta I = \max\{I_{90}(n)\} - \min\{I_{10}(n)\} \ , \tag{18}$$

where $\max\{\}$ and $\min\{\}$ are taken from $1 \leq n \leq n_{\rm max}$. Note that we use all annuli for ΔI, not from $n_{\rm begin} \leq n \leq n_{\rm max}$. This is the result from trial and error.

This procedure is sketched in Figure 17. The data show the flux of a test image (inlaid in the figure) detected in each pixel, which is plotted as a function of semi-major axis of the ellipse. The dotted lines show division into elliptical annuli.

Note that the Y parameter vanishes if the profile is an ideal, smooth function, such as a model de Vaucouleurs or a model exponential profile (in the absence of noise), since $I_{\rm range} = 0$. When the profile exhibits structures such as arms, both $I_{\rm range}$ and Y become non-zero.

The coarseness parameter thus defined may depend on the apparent size of galaxies, because larger images are resolved in finer details. To avoid this dependence, we set the reference size of the galaxy image, and reduce the size of larger galaxies to the reference size. The coarseness parameter is measured for the rescaled image. The number of pixels in the rescaled image is taken to be that in the reference image.

The reduction of image size takes into account the fact that the rescaling factor is generally non-integer and seeing depends on the individual images, as we explain in what follows (see also Figure 18 for illustration). We do not consider galaxies with apparent sizes smaller than the reference.

We rescale the image with the semimajor axis a_{90} to the reference size image with $a_{90}^{\rm ref}$ using Gaussian functions. We assign a Gaussian function to each pixel and map it to the rescaled array. The Gaussian function for the pixel at (x, y) is constructed so that its integration is $I(x, y)f^2$ where

$$f = \frac{a_{90}^{\rm ref}}{a_{90}} \tag{19}$$

is the rescaling factor and the Gaussian width σ_{xy},

$$\sigma_{xy} = \sqrt{\sigma_{\rm ref}^2 - (\sigma_{\rm seeing} f)^2} \ . \tag{20}$$

where $\sigma_{\rm ref}$ is the seeing taken as our reference and $\sigma_{\rm seeing}$ is the actual seeing of each image. With this procedure the PSF in the rescaled image is standardized by varying σ_{xy} from image to image. These Gaussian functions are mapped to a new array with the interval of pixels

$$w = f \times \text{pixel size} \ . \tag{21}$$

This mapping conserves surface brightness.

The sky noise that appears in (16) after rescaling the image differs from the observed value. We must rescale the sky noise as

$$\varsigma_{\rm sky} = f_s \cdot \varsigma, \tag{22}$$

where f_s is calculated by creating an artificial sky of Gaussian noise, applying the same Gaussian smearing, and measuring the standard deviation (f_s). The quantity

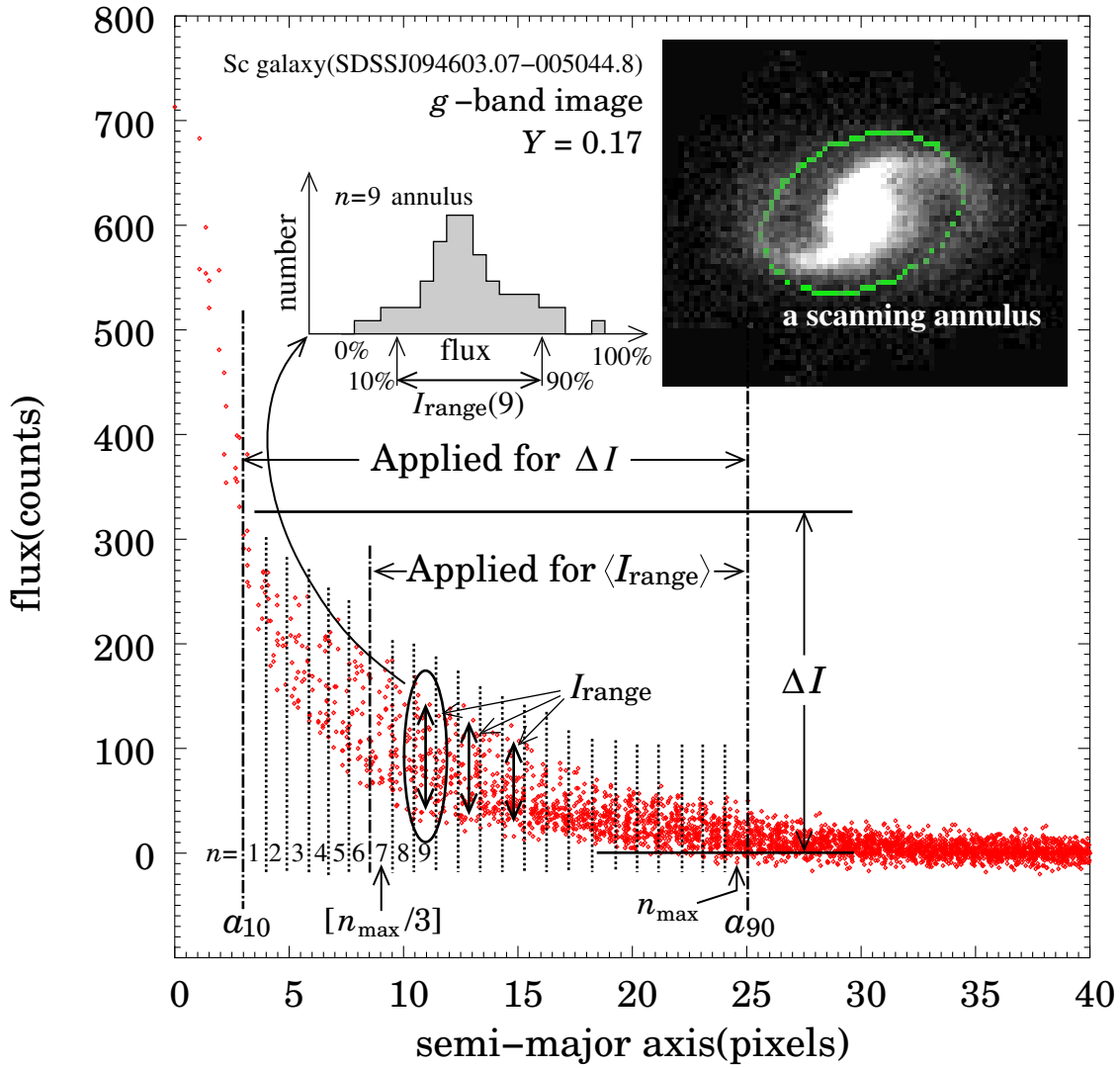

Figure 17: An illustration explaining the method of computing Y for the galaxy image inlaid in the top right of the figure. The figure shows division of the area sandwiched by the two ellipses specified by a_{90} and a_{10} into $n_{\max}$ annuli. The range of flux $I_{\rm range}(n)$ is defined by the 90%- and 10%-tiles of the flux distribution of n-th annulus as an inlaid histogram in the top left of the figure. The $I_{\rm range}$ computed in each annulus is averaged over N annuli to give $\langle I_{\rm range}\rangle$, and the coarseness parameter Y is given as $\langle I_{\rm range}\rangle$ divided by the full dynamic range of the flux observed for the galaxy, ΔI.

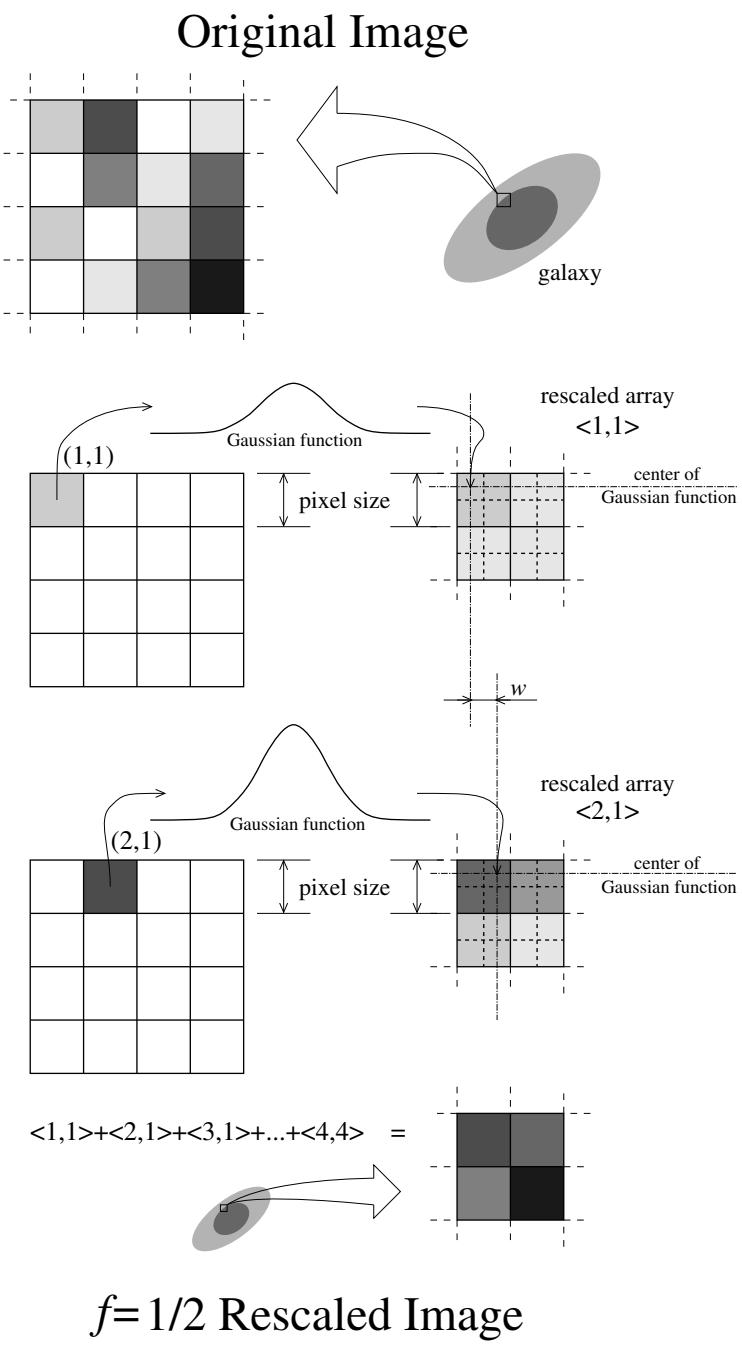

Figure 18: The method of creating rescaled images ($f = 1/2$). Each Gaussian function whose intensity is $I(x, y) \cdot f^2$ and width is adjusted to the effective seeing will be mapped to the rescaled array. The mapping <1,1>+<2,1>+...+<4,4> which creates the rescaled image conserves the surface brightness.

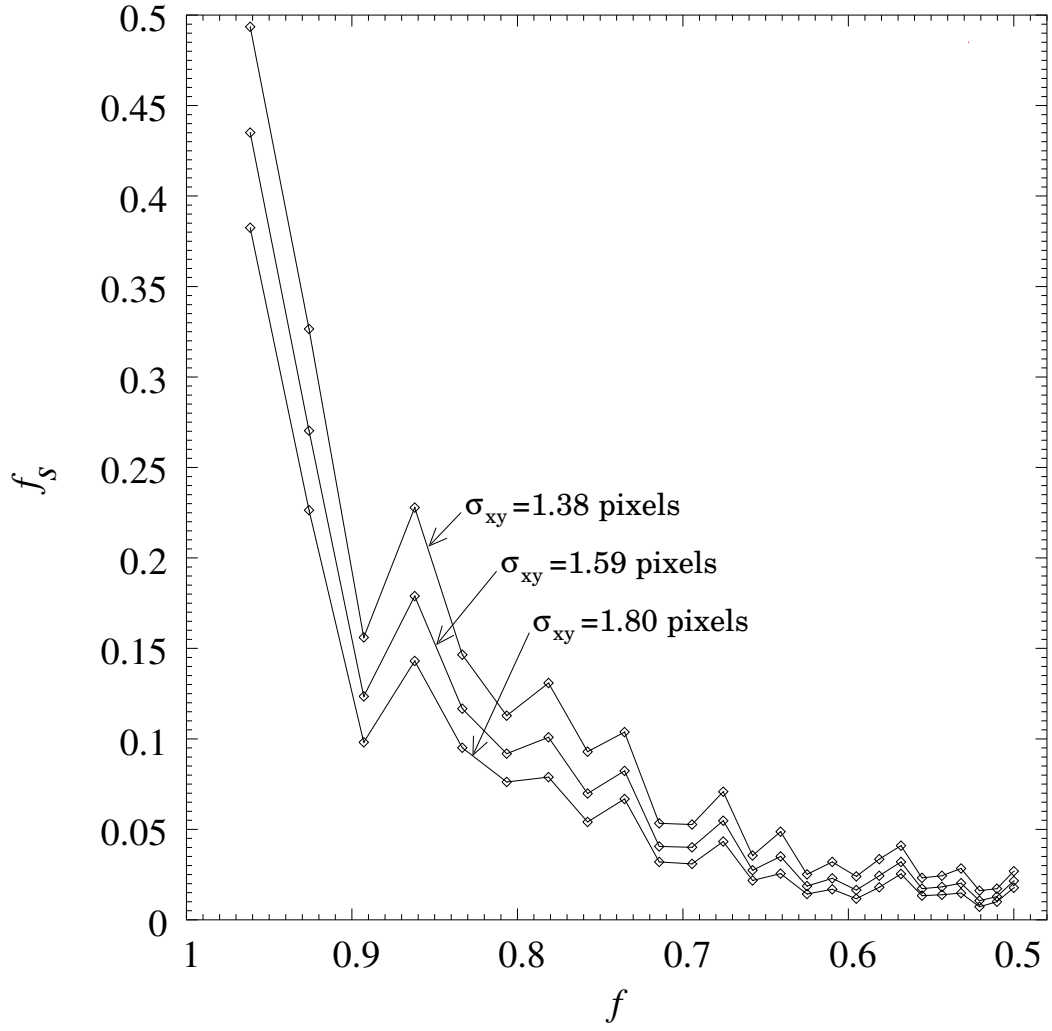

Figure 19: Effective sky noise f_s for the rescaled image as a function of the original sky noise f for a given seeing σ_{xy}.

f_s is dependent on σ_{xy} and the pixel size. The f_s thus calculated is shown in Figure 19.

Remembering the definition of equation (17), we display 16 rescaled g-band images of galaxies which have low Y values (Y<0.00805) in Figure 20, and another 16 having high Y values (Y>0.260) in Figure 21. It is apparent that the galaxies shown in Figure 20 possess very weak texture and are classified as early types. All galaxies shown in Figure 21 have conspicuous texture and are indeed classified as late (Sbc or later)-type spirals.

It is obvious that the texture of galaxies contributes to the numerator of equation (17). We should, however, emphasize the role of the denominator. When galaxies have conspicuous bulges, their ΔI values suppress the Y parameter. On the other hand, the faint bulge leads to a small ΔI value that enhances Y. The most typical case is that of Magellanic irregular type galaxies, in which the texture is not very conspicuous, but the overall intensity contrast is small, giving a small denominator so that Y indicates a very late type.

Figure 22 displays coarseness parameter Y plotted against T. The correlation (r=0.773) is not very impressive compared to that for C_e-T, but this r is caused by the fact that the Y-T correlation is curved away from the linear relation. The important feature in this figure is a very narrow distribution of the Y parameter for $0 \leq T \leq 1$ galaxies. The distribution is confined to the range $0 \leq Y \leq 0.03$, which is but 10% of the full variation of Y.

The effect of inclination on the Y is shown in Figure 23. The linear regression lines for different T are almost flat. They do not appear as flat as those for C_e, but it appears that the slopes of the lines are not caused by any systematic effects (e.g., Sdm is almost flat. The Sc and Sb have opposite slopes), but by the random scatter of the data. We conclude that Y is not affected severely by the inclination of galaxies.

2.4.3 Morphological classifications using $C_{(e)}$ and Y indices

We first attempt to classify galaxies into two types, early 'e' (E-S0/a) and late 'ℓ' (Sa-Im), by setting a dividing value for each of three parameters displayed in Figure 15(a,b) and Figure 22. We evaluate the completeness P and the contamination Q of the 'e' and 'ℓ' samples, as defined by

$$P_e = \frac{N_{e\{\mathrm{E+S0}\}}}{N_{\{\mathrm{E+S0}\}}} \ , \quad Q_e = \frac{N_{e\{\mathrm{Sa+Sb+Sc+Sdm+Im}\}}}{N_e} \ , \tag{23}$$

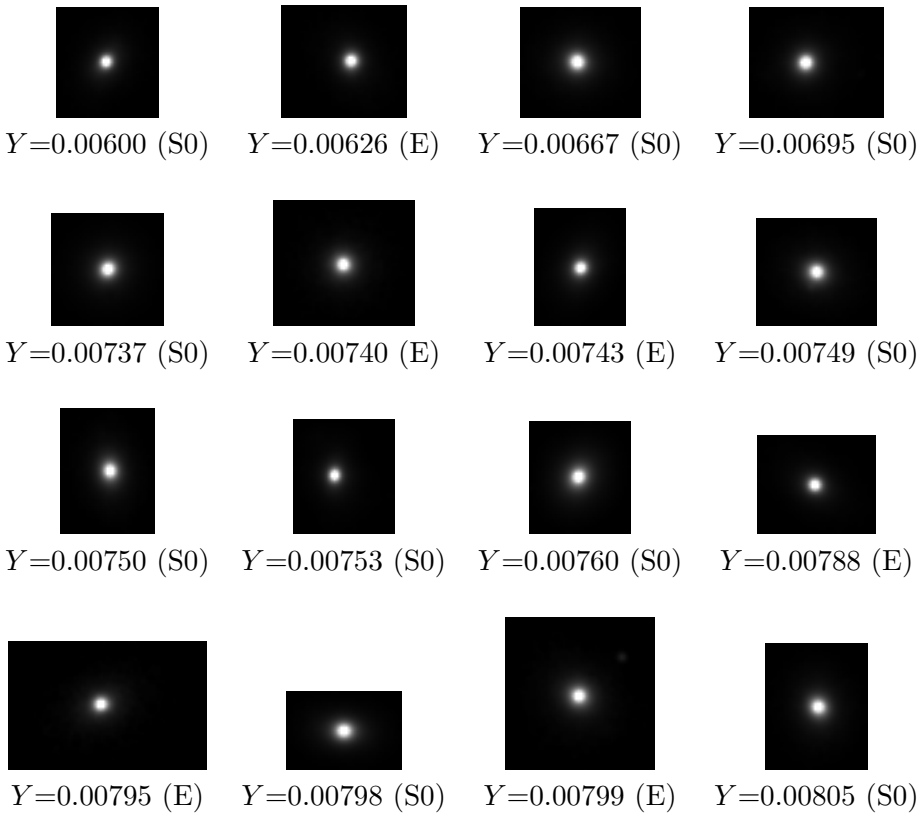

Figure 20: The g-band images (rescaled) of 16 galaxies having the lowest Y in our 1421 galaxies. Shown in parentheses are the visually classified morphological types.

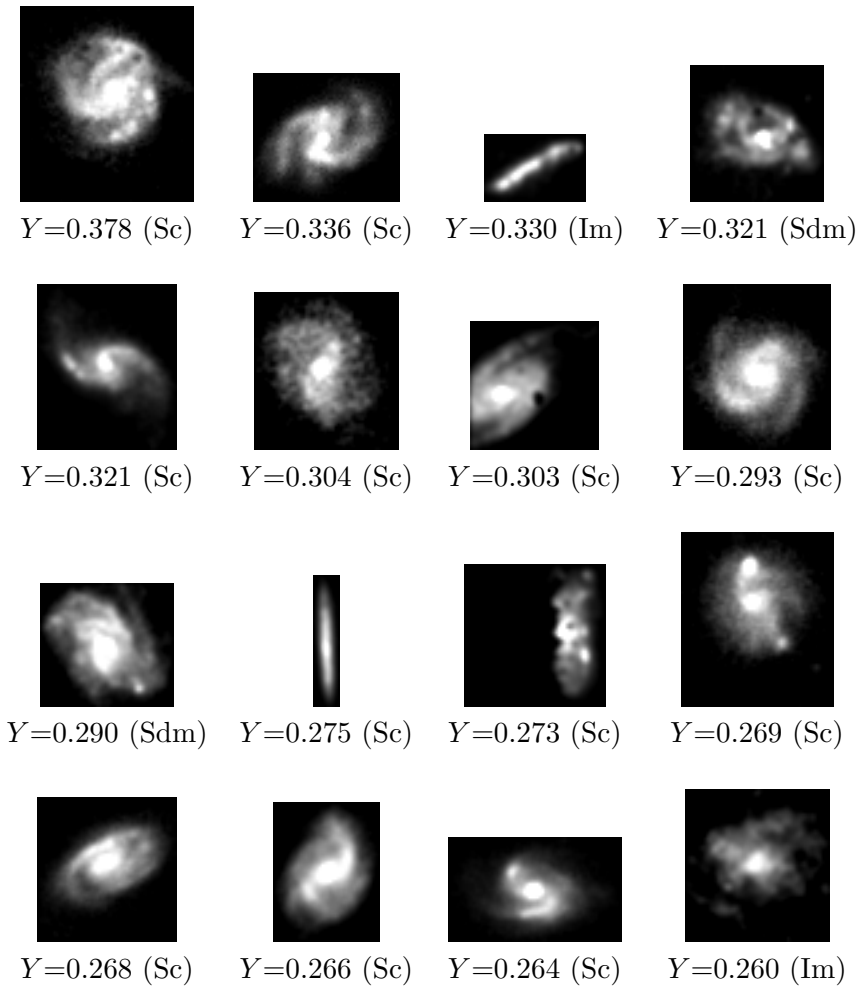

Figure 21: The g-band images (rescaled) of 16 galaxies having the largest Y in our 1421 galaxies. Shown in parentheses are the visually classified morphological types.

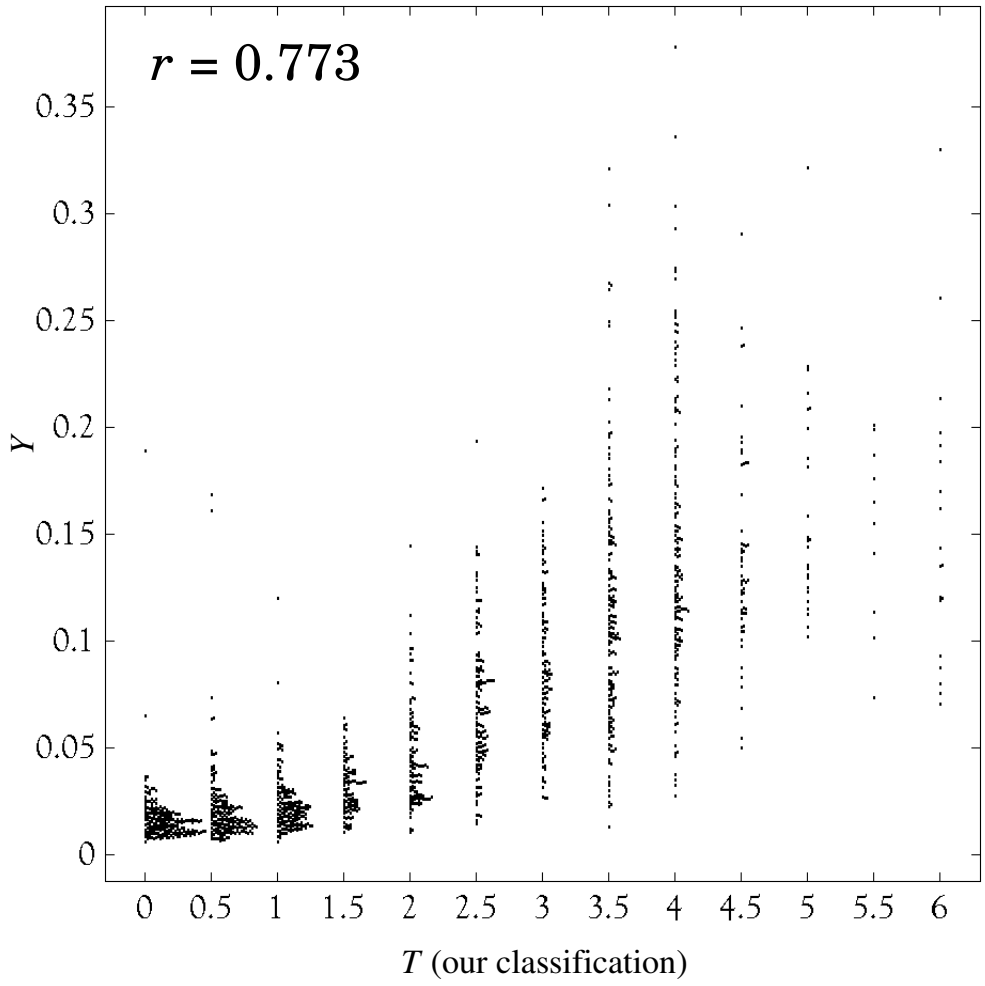

Figure 22: Coarseness parameter Y of 1421 galaxies plotted against morphology T. The value at the top of the figure is the linear correlation coefficient. In case more than one galaxy has the same (T,X) value, T values are displaced to the right by a dot size for clarity. In other words, this scatter plot can be viewed as a histogram.

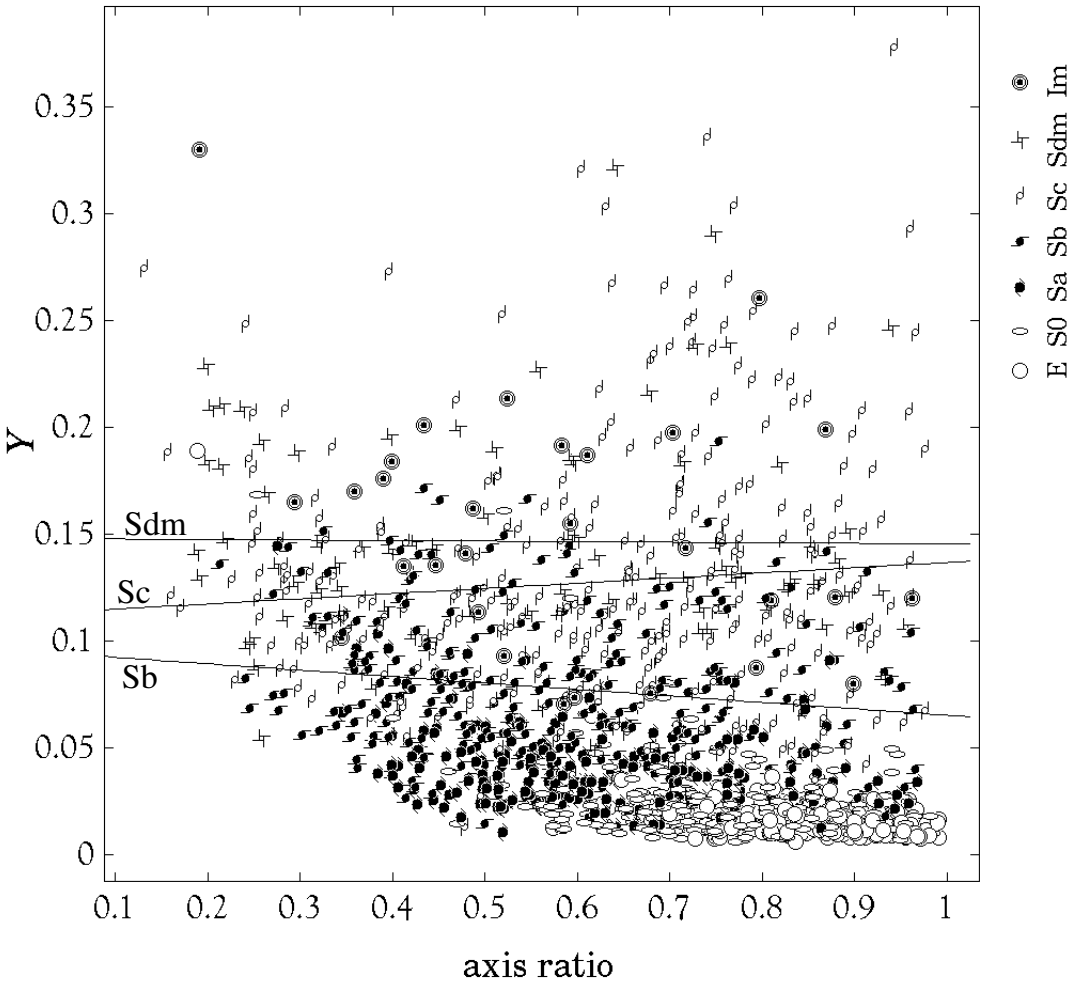

Figure 23: Coarseness parameter Y plotted against the axis ratio. Each symbol indicates visual morphological type, and straight lines are the linear regression for Sb, Sc and Sdm galaxies.

$$P_\ell = \frac{N_{\ell\{\mathrm{Sa+Sb+Sc+Sdm+Im}\}}}{N_{\{\mathrm{Sa+Sb+Sc+Sdm+Im}\}}} \ , \quad Q_\ell = \frac{N_{\ell\{\mathrm{E+S0}\}}}{N_\ell} \ , \tag{24}$$

where N_e is the number of all galaxies chosen by the separator line, $N_{e\{\mathrm{E+S0}\}}$ is the number of E+S0 galaxies chosen by the separator line, and $N_{\{\mathrm{E+S0}\}}$ is the total number of E+S0 galaxies. Other notations are defined similarly.

Figure 24 shows completeness and contamination for the classification using the C parameter. The same figure is given in Shimasaku et al. (2001) which attains 80% completeness, but based on the SDSS commissioning data. Strateva et al. (2001) also reports 83% completeness using a concentration index with circular apertures. We find that P_e=P_ℓ=85.0%, Q_e=22.5% and Q_ℓ=9.5% with the use of the division constant C_1=0.339. The success rate is somewhat higher in our case, however, with essentially the same division parameter. Improved performance is given in Figure 25 where the C parameter is replaced with C_e: we obtain P_e=P_ℓ=86.7%, Q_e=20.0% and Q_ℓ=8.2% for C_{e1}=0.349. One may attain Q_e=Q_ℓ=15.0% with the choice of C_{e1}=0.332 if the completeness of E+S0 galaxies is sacrificed.

Classification using the Y parameter is presented in Figure 26. This approach achieves a higher success rate than the C_e classification, P_e=P_ℓ=88.1%, Q_e=18.1% and Q_ℓ=7.5% for Y_1=0.030. We can attain minimum contamination of Q_e=Q_ℓ=12.1% for Y_1=0.024 with a modest cost of P_e. The Y parameter is superior to the concentration indices as the morphology classifier.

We now try to obtain the maximum performance using two parameters, C_e and Y, by optimising the choice of the dividing parameters (see Figure 27). We consider the position of the center of the average 2-vector for each morphological class,

$$G_{\mathrm{E}} = \begin{pmatrix} \langle C_{e\mathrm{E}} \rangle \\ \langle Y_{\mathrm{E}} \rangle \end{pmatrix}, \ G_{\mathrm{S0}} = \begin{pmatrix} \langle C_{e\mathrm{S0}} \rangle \\ \langle Y_{\mathrm{S0}} \rangle \end{pmatrix}, ..., \ G_{\mathrm{Im}} = \begin{pmatrix} \langle C_{e\mathrm{Im}} \rangle \\ \langle Y_{\mathrm{Im}} \rangle \end{pmatrix}. \tag{25}$$

where $\langle C_{e\mathrm{E}} \rangle = (1/N_{\mathrm{E}}) \sum_{i\in\mathrm{E}} C_{e\mathrm{E}}^i$ etc. With the weight of the number of the galaxies having the relevant morphological class given to these points, we fit 7 points by a quadratic function. For our 1421 galaxies, we obtain

$$f_q(C_e) = 2.702 C_e^2 - 1.419 C_e + 0.1967. \tag{26}$$

In general, when the distribution in two-parameter space shows linear regression, the parallel separator lines are placed along a regression line (Doi et al. 1993). We apply this method to the quadratic regression line. We then consider a set of lines crossing this quadratic curve at $(C_{e1}, f_q(C_{e1}))$,

$$f_l(C_e) = -\frac{K}{f_q'(C_{e1})}(C_e - C_{e1}) + f_q(C_{e1}) \tag{27}$$

where K is a constant, and f_q' is the first derivative of f_q. We take $f_l(C_e)$ as the dividing line for classification. We adopt K=0.1, which turns out to give the best performance. Figure 27 shows the average 2-vector and standard deviation for each morphological class, quadratic regression $f_q(C_e)$ and the best classifiers by equation (27) plotted as two dot-dashed separator lines.

Classification using the C_e-Y diagram is presented in Figure 28. The maximum success rate we achieved is: P_e=P_ℓ=89.4%, while Q_e=16.4% and Q_ℓ=6.7% at C_{e1}(crossing)=0.348, or Q_e=Q_ℓ=11.8% with P_e=79.3% and P_ℓ=93.6% at C_{e1}(crossing)=0.337. These are remarkably high success rates given the fact that visual classification suffers from uncertainties, perhaps of the order $\Delta T \sim 1$.

We consider separation into three types, dividing late ('ℓ')- type galaxies into early ($\sim$ Sa+Sb) and late spirals ($\sim$ Sc+Sdm+Im). We call the two classes of the sample $\ell_{\rm I}$ and $\ell_{\rm II}$. We fix the first division to give the best performance for early-type to late-type separation as determined in the previous subsection. We set the second division which separates $\ell_{\rm I}$ and $\ell_{\rm II}$ so that the completeness of Sa+Sb in $\ell_{\rm I}$ and that of Sc+Sdm+Im in $\ell_{\rm II}$ are nearly equal.

We show the results in matrices of 3×3 (and an additional row and column to show the subtotals) in Table 1 for the three indicators using C, C_e and Y. We take the second division separators which divide late-type galaxies into early- and late-spirals to be C_2=0.436, C_{e2}=0.463, and Y_2=0.106, respectively, while the separators between early- and late-type galaxies are the same as those quoted in the beginning of Section 2.4.3. The completeness can be read from the column by dividing the number in the diagonal entry by the total number listed in the bottom of the corresponding column. For example, the completeness of Sa+Sb galaxies separated by $C_{1,2}$ is 278/461 = 60.3%. This compares to 285/461 = 61.8% with the use of C_e, and 305/461 = 66.2% with Y. The contamination is read from the row. The contamination in the early spiral galaxy sample, $\ell_{\rm I}$, from E+S0 galaxies and late-type spiral galaxies, for instance, is $(76 + 161)/515 = 46.0\%$ with the use of C, $(68+156)/509 = 44.0\%$ with C_e, and $(59+138)/502 = 39.2\%$ with Y. Similarly, the contamination in the late spiral $\ell_{\rm II}$ sample is 20.0%, 20.2%, and 17.9% respectively.

The classification with Y again produces the best result. We also note that the gain attained with the use of elliptical apertures over circular apertures is small for the separation of $\ell_{\rm I}$ and $\ell_{\rm II}$, although the C_e parameter gives generally better performance, if slight. One might question why the gain with C_e over C is rather small in contrast to the emphasis given in the previous section that the effect of inclination is greatly removed with the C_e parameter. The reason is that early and

late spiral galaxies are not well separated in the concentration parameter space, and show large dispersion that heavily overlaps. So the effect of inclination does not play a crucial role. In fact, visual separation into early and late spirals relies more on the opening of spiral arms and textures.

It is important to note that contaminants from late spirals to the early-type sample, or vice versa, are very small, less than $\leq 1\%$, at least with the C_e and Y indices. Most of the contaminants in the E+S0 sample are from S0a and Sa galaxies.

Finally, we examine how the performance of our morphology classifier improves by considering 2-dimensional classification in the C_e-Y space. The result is shown in Table 2. The completeness of Sa+Sb galaxies is $314/461 = 68.1\%$, a 2% increase, compared with the value found employing Y alone. The contamination in the $\ell_{\rm I}$ sample from E+S0 galaxies and late-type spiral galaxies decreases to $(53 + 137)/504 = 34.1\%$, which is smaller than the value using Y alone by 5%. The contamination in the early-type spiral sample still primarily arises from late-type spiral galaxies, rather than E+S0 galaxies. The contamination in the $\ell_{\rm II}$ sample decreases from 17.9% to 17.2%.

2.4.4 The importance of improvements/devices of morphological parameters in thesis work

Only less than 100 galaxies are used for the main study of this thesis. In addition, the selection of E+A galaxies depends on spectroscopy only. Although it was shown that the new devised texture parameter 'coarseness' shows excellent performance in section 2.4.2, the study of the application limit of apparent size of Y parameter is not enough. Therefore I did not employ Y parameter in the main study of this thesis.

However, I was able to keep higher purity of 49 elliptical galaxies as a control sample using improved concentration index C_e. At first, I tried using circular-based concentration index, only to find significant contamination in elliptical sample which included edge-on late-type galaxies. Therefore, the elliptical-based concentration index is employed to confirm E+A morphologies. The morphology is one of the actively debated aspects in E+A problems, therefore, it is of a great significance to employ a newly improved parameter of C_e.

A newly developed image-processing technique described in this subsection provides a necessary basis for the application in section 3, where I perform an extremely precise photometric reduction. The author's contrivance of SDSS photometry in section 3 is presented in section 2.5.

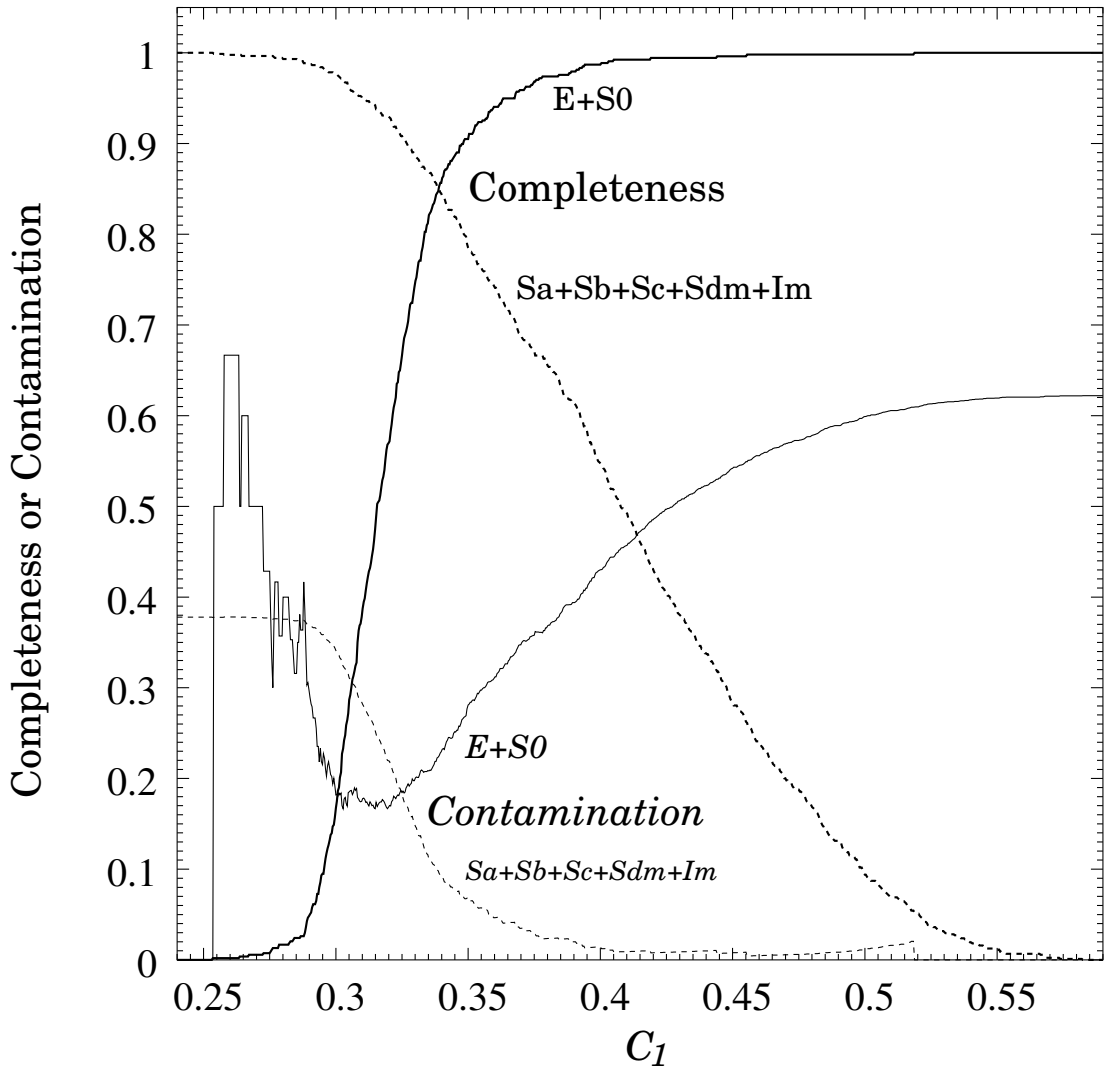

Figure 24: Completeness P and contamination Q for early- and late-type galaxy samples as a function of division parameter C_1 with the standard circular aperture definition. The thick solid and dotted lines show completeness for early- and late-types. The thin solid and dotted lines show contamination for early- and late-types.

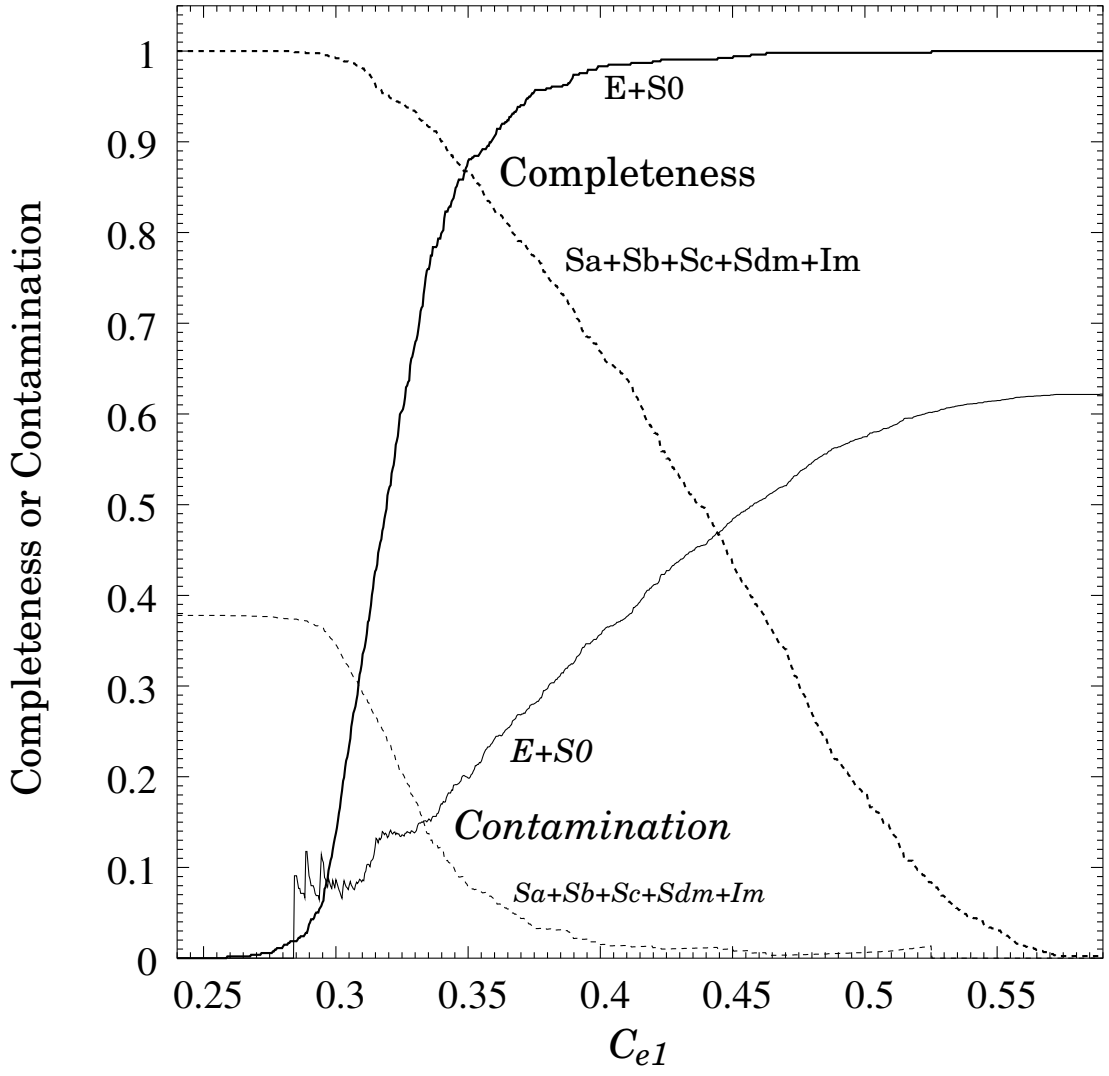

Figure 25: Completeness P and contamination Q of early- and late-type galaxy samples as a function of division parameter C_{e1} with the use of elliptical apertures. See Figure 24 for the line definitions.

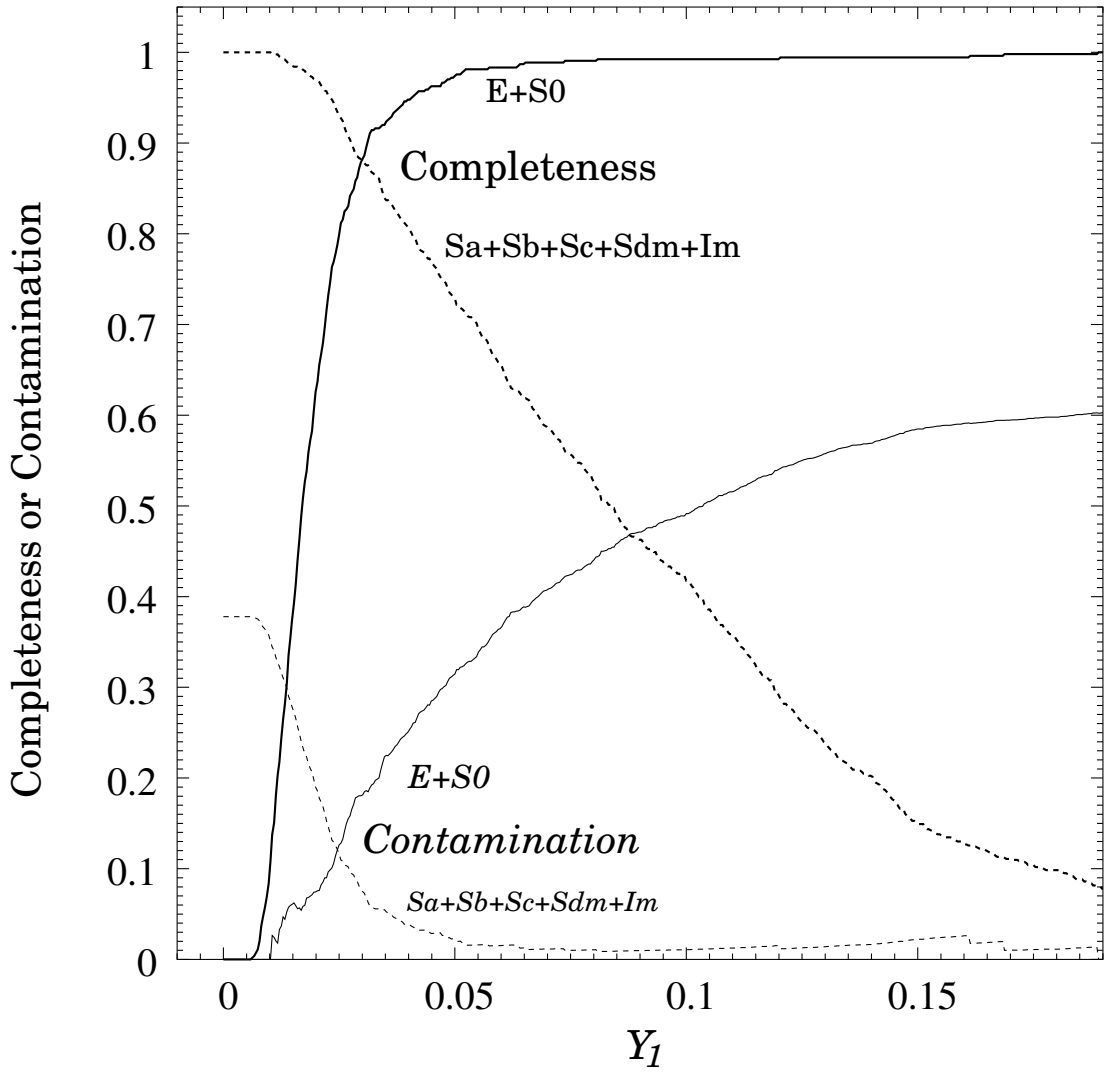

Figure 26: Completeness P and contamination Q of early- and late-type galaxy samples as a function of division parameter Y_1. See Figure 24 for the line definitions.

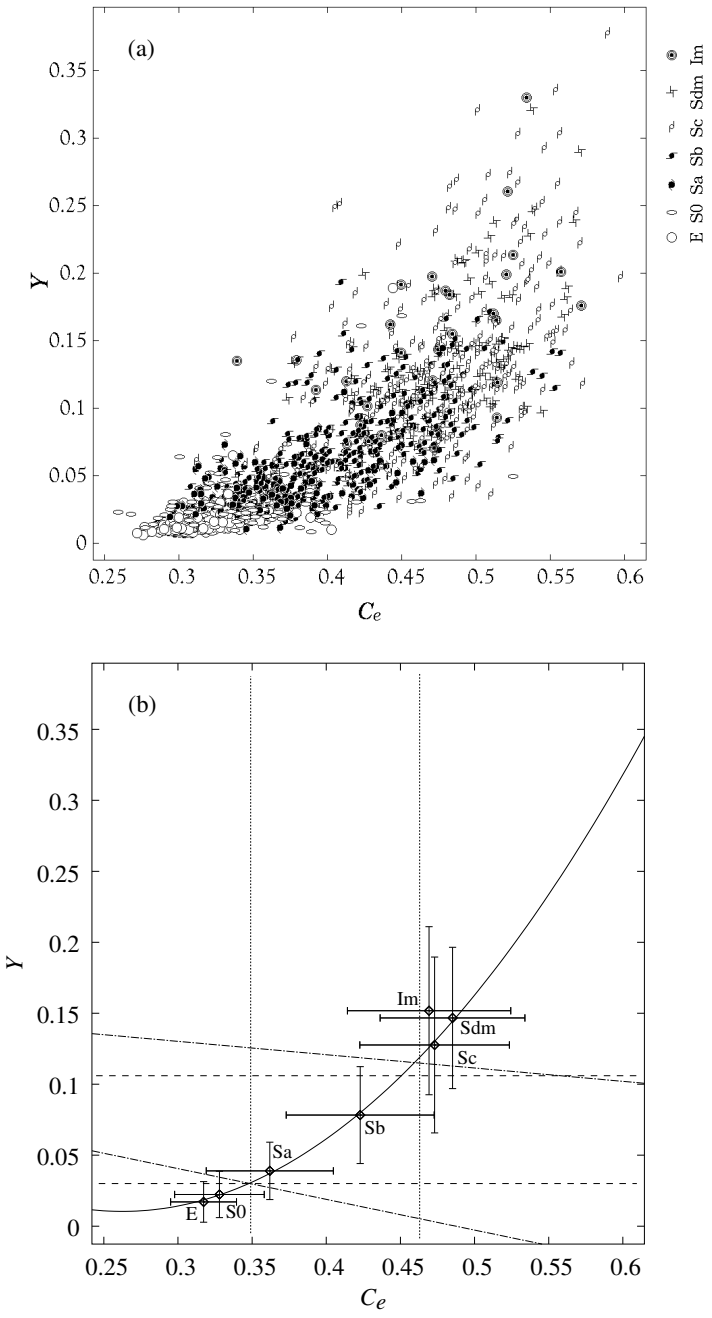

Figure 27: (a) 1421 Galaxies plotted on the (C_e,Y) plane and (b) the average 2-vector and standard deviation for each morphological class. The quadratic function in (b) is the regression line by least-squares fitting to the average 2-vector of galaxies. The two dot-dashed lines are the best classifiers into three types, E+S0, Sa+Sb and Sc+Sdm+Im on the 2-dimensional classification. The dotted and dashed lines show the best of one dimensional separators using C_e and Y, respectively.

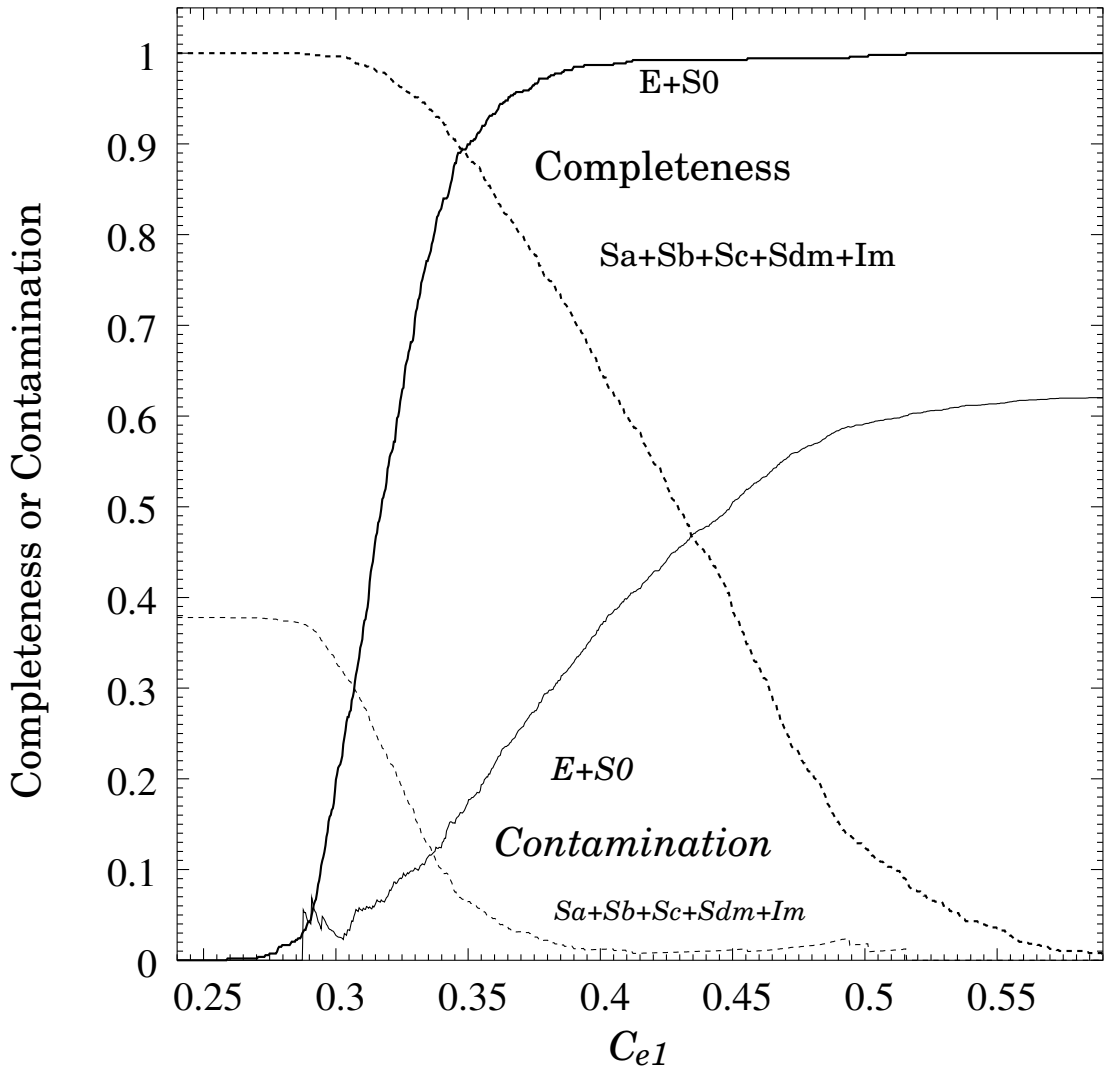

Figure 28: Completeness and contamination of the early and late-type galaxy samples as a function of C_{e1} specified at the crossing point with the quadratic function, using the C_e-Y diagram (Figure 27). See Figure 24 for the line definitions.

C Parameter				
	E+S0	Sa+Sb	Sc+Sdm+Im	Total
e-region	**458**	124	9	591
$\ell_{\rm I}$-region	76	**278**	161	515
$\ell_{\rm II}$-region	3	59	**253**	315
Total	537	461	423	1421
C_e Parameter				
	E+S0	Sa+Sb	Sc+Sdm+Im	Total
e-region	**468**	111	6	585
$\ell_{\rm I}$-region	68	**285**	156	509
$\ell_{\rm II}$-region	1	65	**261**	327
Total	537	461	423	1421
Y Parameter				
	E+S0	Sa+Sb	Sc+Sdm+Im	Total
e-region	**474**	99	6	579
$\ell_{\rm I}$-region	59	**305**	138	502
$\ell_{\rm II}$-region	4	57	**279**	340
Total	537	461	423	1421

Table 1: Classification of 1421 galaxies into three types (E+S0 : Sa+Sb : Sc+Sdm+Im) using parameter C,C_e, or Y. A completeness can be calculated by a column, and a contamination by a row; i.e. in the case of C, completeness of E+S0 in the e-region is 458/537$\simeq$0.85 (by a column), and contamination of the e-region is (124+9)/591$\simeq$0.23 (by a row).

C_e-Y Diagram				
	E+S0	Sa+Sb	Sc+Sdm+Im	Total
e-region	**480**	92	2	574
$\ell_{\rm I}$-region	53	**314**	137	504
$\ell_{\rm II}$-region	4	55	**284**	343
Total	537	461	423	1421

Table 2: Classification of 1421 galaxies into three types (E+S0/Sa+Sb/Sc+Sdm+Im) using the C_e-Y diagram. A completeness can be calculated by a column, and a contamination by a row; i.e. completeness of E+S0 in the e-region is 480/537$\simeq$0.89 (by a column), and contamination of the e-region is (92+2)/574$\simeq$0.16 (by a row).

2.5 Handling SDSS Imaging Data — author's development for thesis

Since the database of SDSS is huge, it is not realistic that researchers download whole data and hold them. Therefore, the SDSS project provided some database servers managed by the SDSS project itself and by some universities. These servers are called 'Catalog Archive Server(CAS)'. Researchers send their requests using the SQL language to a server, and download a part of catalog which they need. The SQL language itself is not so difficult to understand it, and the SDSS project prepared substantial example queries. Recently, many astronomers use the SQL service and publish their papers based on the SDSS catalog. Though frequency in use of the SQL have raised, users may feel awkward in searching observational data stored in the CAS. Since the SDSS data is so large with so many pre-measured quantities, it is not usually straight-forward to find the exact data needed for your research. It is almost like finding a needle in a haystack. This is the first difficulty which users must overcome to use the SDSS data.

The CAS also provides imaging-related service, e.g., Finding Chart, Navigate, Imaging List and Explore. Researchers can easily use them, since these services are web-based systems. Actually, these services are very useful to plan for our follow-up observation. However, if we want to do photometry using the SDSS imaging data, we must download imaging data from the 'Data Archive Server(DAS)' and analyze them. The DAS provides reduced imaging and spectroscopic data, and we can compute observational quantities not stored in CAS from them. Needless to say, it is often important to measure observational quantities by yourself to fulfill your scientific needs. However, for example, doing a photometry on your own is not easy because the SDSS imaging data have its own specifics and one must surmount complicated dealing of various data files. In other words, we must reproduce a part of the intricate procedure in the SDSS photometric pipeline (PHOTO) to do photometry. To ease these procedures, in this subsection, author's development in handling the SDSS imaging data is introduced to readers.

2.5.1 Getting atlas image with special header

The DAS provides reduced imaging data in the form of fpC (corrected frames) and fpAtlas (atlas images) files (Stoughton et al. 2002). The each corrected frame, fpC file, is a normal fits image file, covering the region of $\sim 811'' \times 590''$. The objects in fpC files are detected and cut out by PHOTO, and the deblended image of each

object are stored using the Rice compression in the atlas images, fpAtlas files. When we want to do photometry for an object, basically we can use an fpAtlas file. If there are problems in the deblended image, one must consider the use of fpC.

The SDSS project prepared a standalone software, readAtlasImages[2)], to extract the compression of fpAtlas and create a normal fits image file, and we can easily use it. However, we cannot immediately do photometry using its normal fits image file created by readAtlasImages because the fits image file created by readAtlasImages does not have information needed for photometry.

The SDSS magnitudes m and its error $m_{\rm err}$ are derived by the following equations used in the SDSS photometric pipeline (PHOTO; Lupton et al. 2001),

$$f/f0 = N_{\rm cnt}/T_{\rm exp} \cdot 10^{0.4(v_{\rm aa}+v_{\rm kk}\cdot v_{\rm air})} \tag{28}$$

$$m_{\rm asinh} = -\frac{2.5}{\ln 10} \cdot \left\{ {\rm asinh}\left(\frac{f/f0}{2b}\right) + \ln b \right\} \tag{29}$$

$$m_{\rm Pogson} = -2.5 \cdot \log(f/f0) \tag{30}$$

$$N_{\rm cntErr} = \sqrt{\frac{N_{\rm cnt} + N_{\rm pix}\cdot N_{\rm sky}}{G} + N_{\rm pix}\cdot(V_{\rm D} + N^2_{\rm skyErr})} \tag{31}$$

$$m_{\rm err} = \frac{2.5}{\ln 10} \cdot \frac{(N_{\rm cntErr}/T_{\rm exp})\cdot(1/2b)\cdot 10^{0.4(v_{\rm aa}+v_{\rm kk}\cdot v_{\rm air})}}{\sqrt{1+\{(f/f0)/2b\}^2}} \ , \tag{32}$$

where $N_{\rm cnt}$ and $N_{\rm pix}$ are counts and the number of pixels within an aperture on atlas image, $T_{\rm exp}$ is exposure time in the fpC file, $v_{\rm aa}$, $v_{\rm kk}$, $v_{\rm air}$, G and $V_{\rm D}$ are zero-point, extinction coefficient, airmass, gain and dark variance in tsField file, $N_{\rm sky}$ and $N_{\rm skyErr}$ are the counts of sky and its error in tsObj file, and b is the asinh softening parameters. The $f/f0$ is called 'maggies', and the most basic photometric value in SDSS. See the DR2 Photometric Flux Calibration page[3)] for detail of computing magnitude from the SDSS CCD images.

Unfortunately, an fpAtlas file does not include various values required for photometry mentioned above. Therefore, we must access not only fpAtlas but also fpC, tsField and tsObj files. The values such as airmass and sky are archived using fits binary table in tsField and tsObj files. We can easily read fits binary table using some GUI tools such as fv[4)]. However, if we intend to analyze many objects, we have to fall into ugly routine work and use of GUI tools is not realistic. Therefore,

[2)] http://www.sdss.org/dr2/products/images/read_atlas.html
[3)] http://www.sdss.org/dr2/algorithms/fluxcal.html
[4)] http://heasarc.gsfc.nasa.gov/docs/software/ftools/fv/

a contrivance is required. I achieved this by revising the output of readAtlasImages. That is, the code of readAtlasImages is modified so that it outputs fits image file with a special header which includes all values required for photometry such as airmass and sky. This thesis work also required the exact center position of each object, seeing size and reddening, so they are also extracted to the header. Moreover, readAtlasImages cannot create fits image file which includes all images of the 5 passbands, and sometimes outputs broken images. I improved these points and show an example in Figure 29 which expedite dexterity of photometry.

This software developed by the author using C language is named 'get_atlas'. The get_atlas automatically accesses local disk or network(http) and retrieves fpC, tsField and tsObj files, and reads fits binary table using CFITSIO[5)] functions. Al-

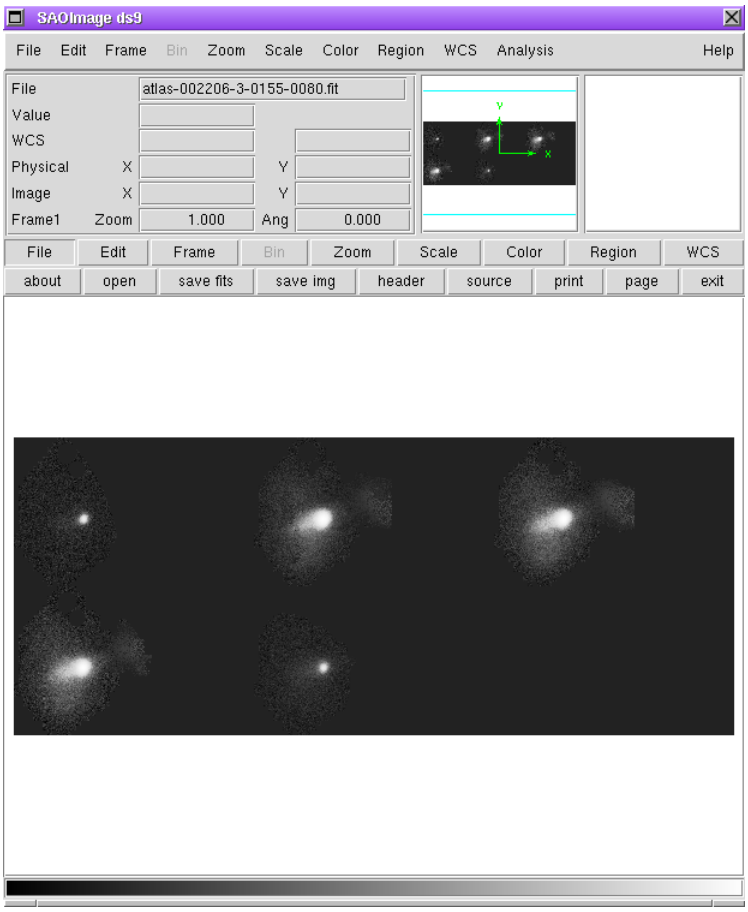

Figure 29: A special fits image file created by 'get_atlas'. The images of 5 passbands are included in a fits file to expedite dexterity of photometry.

[5)] http://heasarc.gsfc.nasa.gov/docs/software/fitsio/fitsio.html

though the fpC files are compressed by gzip, their file sizes are somewhat large and the retrieve of fpC via network takes a lot of time. Therefore, get_atlas retrieves a head part of fpC via network using cURL[6] and zlib to minimize lost time. Figure 30 is an example of header of fits image file created by get_atlas. The header includes all values required for photometry, and we can do photometry using this fits image file only. After all, what we have to do is that we write the code which reads fits header and pixel counts of images, and calculates magnitudes equation (28) $\sim$ (32).

Of course, when we pick out values from tsField and tsObj manually, we must know not only the directory or URL of tsField and tsObj file but also the data structure of binary tables. But use of get_atlas software relieves researches from it. The get_atlas can be easily used in shell script, so we can use it for huge sample. I intend to distribute the get_atlas for astronomers in the near future.

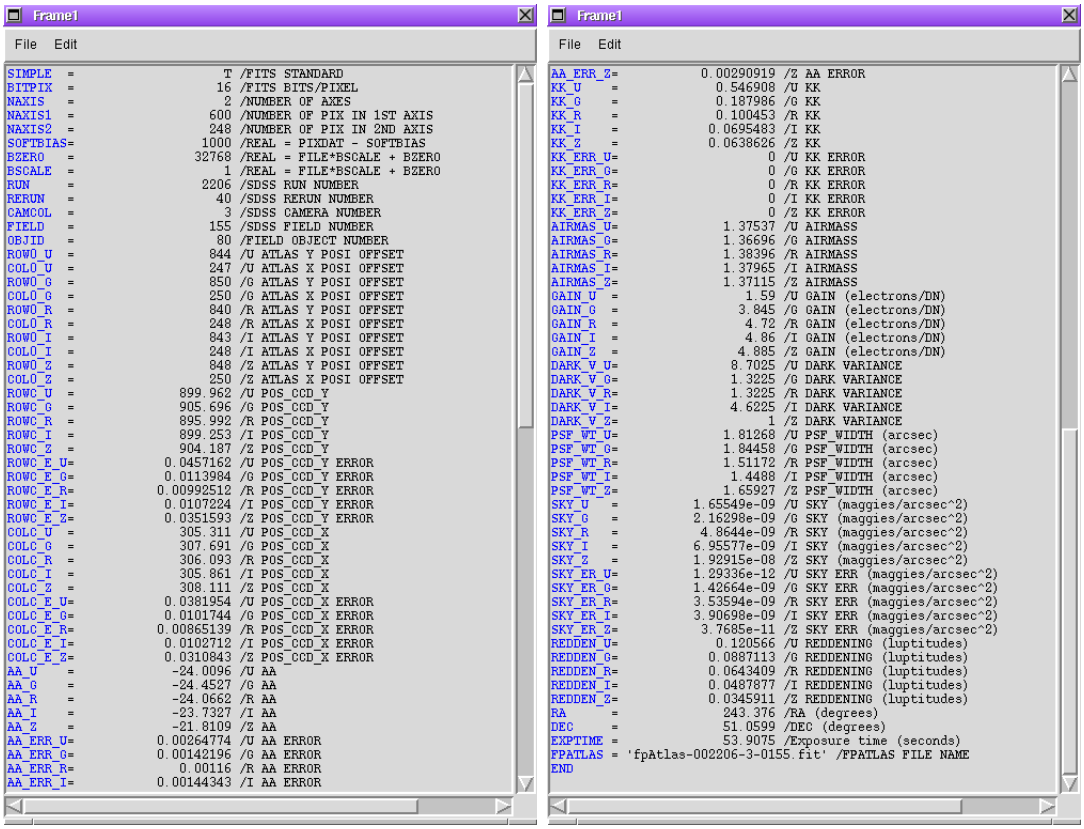

Figure 30: A special header of the fits image file in Figure 29 created by 'get_atlas'. The header includes all values required for photometry.

[6] http://curl.haxx.se/

2.5.2 Composition of two band images and K-correction

In section 3, the strict composition of two band images and pixel-to-pixel K-correction are required. Currently, there is no software which enables us easily to do both the composition and K-correction simultaneously. Therefore, these computation is also done by author's original software written by C language. Fortunately, Blanton et al. (2003) developed `kcorrect.v3_2` library for K-correction for the SDSS broad-band imaging. The composition of two band images depends on author's original code, and K-correction is performed using `kcorrect.v3_2` functions, which is called by my original software. Here, focusing on the composition of two band images using atlas images, the details of procedure are presented.

In the atlas images, the seeing sizes differ from passband to passband. If we do subtraction using two band images without seeing correction, it will produce erroneous colormap. In addition, `kcorrect.v3_2` library refers magnitudes of 5 passbands. Therefore, I smear all images except that with the worst seeing $\sigma_{\rm max}$ among the passbands to equalize seeing sizes of all passbands, u,g,r,i and z. Assuming that point-spread function is Gaussian function, images are convolved with Gaussian function of $\sigma_{\rm c}$,

$$\sigma_{\rm c} = \sqrt{\sigma_{\rm max}^2 - \sigma^2}, \tag{33}$$

where σ is the actual seeing of each image derived from `psf_width` parameter in tsField files:

$$\sigma = (\texttt{psf\_width}/1.06)/2.35, \tag{34}$$

where `psf_width` is equivalent to 1.06 FWHM for a Gaussian profile (Fan et al. 2003).

Unfortunately, the relation between physical and imaging position of a passband on atlas image is not equal to others but slightly differs. That is, even if we do subtraction using two band images with seeing correction, it will also produce erroneous colormap due to slight difference of object's positions on atlas images. This is a serious problem for calculating color near the galaxy center, since the profile near galaxy center is very steep. Therefore we cannot directly compose g- and r-band images, or r- and i-band images using the coordinates given by the fpAtlas file. I adjust the positions of the multi-band images in the following way.

Each passband image are resampled using positional information, "`colc`" and "`rowc`"(real) in tsObj file, and "offsets wrt[7)] reference color"(`dcol` and `drow`; integer) and "bounding box"(`cmin` and `rmin`; integer) in "master mask" in fpAtlas file (see

[7)] with reference to

source code of readAtlasImages). Where "colc" and "rowc" are the exact center position of object in fpC coordinates, and (cmin + dcol, rmin + drow) is the fiducial point of atlas images in fpC coordinates (see Figure 31). The typical error of "colc" and "rowc" are $0.01 \sim 0.1$ pixel($0.004 \sim 0.04$ arcsec).

In the case of making $g-r$ 2D colormap without resampling r-band image, the preliminary position offset $(x0_{pg}, y0_{pg})$ of g-band pixels needed for $1\times$ g-band resampling in atlas image coordinate is

$$\begin{aligned} x0_{pg} &= (\mathtt{colc}_g - \mathtt{col0}_g) - (\mathtt{colc}_r - \mathtt{col0}_r) \\ y0_{pg} &= (\mathtt{rowc}_g - \mathtt{row0}_g) - (\mathtt{rowc}_r - \mathtt{row0}_r) \ , \end{aligned} \tag{35}$$

where col0 = cmin + dcol and row0 = rmin + drow. The idea of equation (35) is sketched in Figure 32. That is, if we begin resampling at $x0_{pg}$ in g-band atlas image, the position of object of resampled g-band is set equal to that of r-band completely.

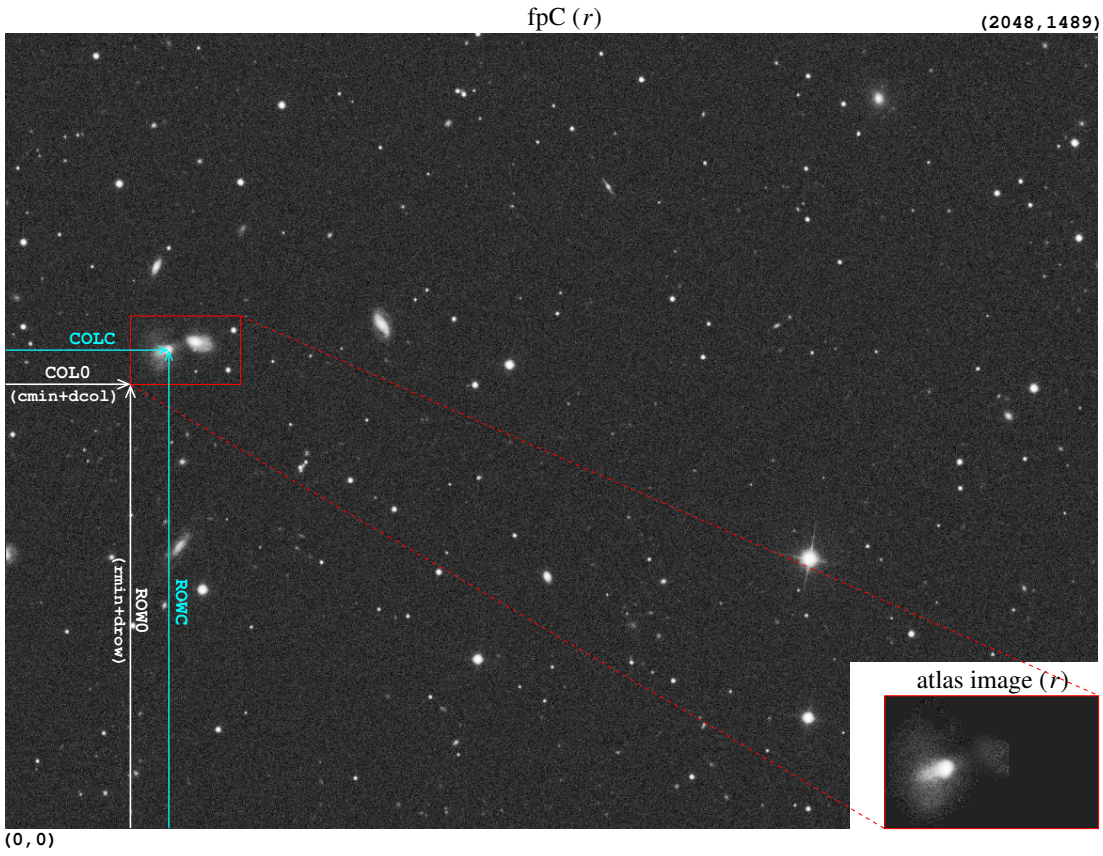

Figure 31: Positional parameters "col0", "row0", "colc" and "rowc" in fpC coordinates, and relation between fpC and atlas image. The unit of fpC coordinates is in pixels.

And I consider the values $(d0_x, d0_y)$:

$$\begin{aligned} d0_x &= x0_{pg} - [x0_{pg}] \\ d0_y &= y0_{pg} - [y0_{pg}] \end{aligned} \tag{36}$$

where $[x]$ is the floor function and $(d0_x, d0_y)$ indicates a distance from pixel grid and resampled position of g-band pixels (That is, the resampling is not required when $(d0_x, d0_y) = (0, 0)$).

Resampling only g-band image is not reasonable. Both r- and g-band should be resampled and optimized. Then I determine the position offsets by $d0_x$,

$$\begin{aligned} x0_{og} &= x0_{pg} + (-d0_x/2) \\ x0_{or} &= (-d0_x/2) \end{aligned} \qquad \text{for} \quad d0_x <= 0.5 \tag{37}$$

or

$$\begin{aligned} x0_{og} &= x0_{pg} + (1 - d0_x)/2 \\ x0_{or} &= (1 - d0_x)/2 \end{aligned} \qquad \text{for} \quad 0.5 < d0_x \ , \tag{38}$$

and by $d0_y$,

$$\begin{aligned} y0_{og} &= y0_{pg} + (-d0_y/2) \\ y0_{or} &= (-d0_y/2) \end{aligned} \qquad \text{for} \quad d0_y <= 0.5 \tag{39}$$

or

$$\begin{aligned} y0_{og} &= y0_{pg} + (1 - d0_y)/2 \\ y0_{or} &= (1 - d0_y)/2 \end{aligned} \qquad \text{for} \quad 0.5 < d0_y \ . \tag{40}$$

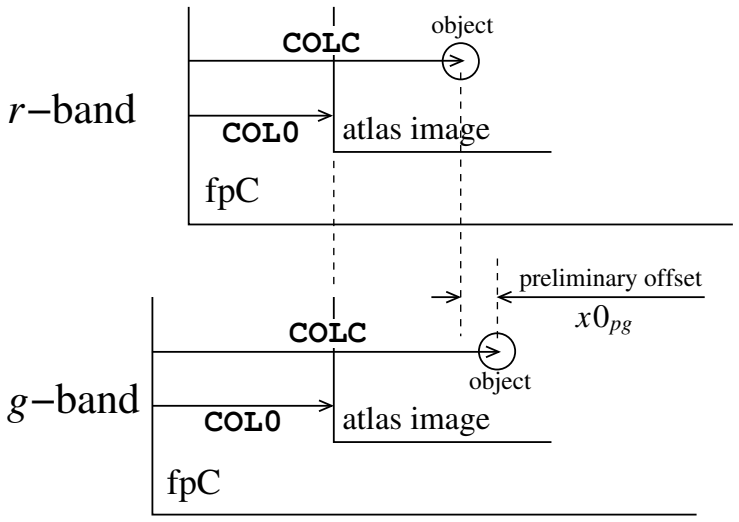

Figure 32: Schematic viewgraph of the relation between positional parameters and preliminary offset $x0_{pg}$.

These position offsets minimize declines of the resolution in r- and g-band images. The position offsets of u-, i- and z-band, $x0_{ou}$, $x0_{oi}$ and $x0_{oz}$, are also derived by equation (37) or (38), and (39) or (40) with replacing g with u, i or z. The $x0_{pu}$, $x0_{pi}$ and $x0_{pz}$ are calculated by equation (35) with replacing g with u, i or z (Note that equation (36) is applied for g-band only).

In the case of $r-i$ 2D colormap, $x1_i$, $y1_i$, $x1_r$ and $y1_r$ are calculated in the same convention. That is,

$$\begin{aligned} x1_{pi} &= (\mathtt{colc}_i - \mathtt{col0}_i) - (\mathtt{colc}_r - \mathtt{col0}_r) \\ y1_{pi} &= (\mathtt{rowc}_i - \mathtt{row0}_i) - (\mathtt{rowc}_r - \mathtt{row0}_r) \ , \end{aligned} \tag{41}$$

$$\begin{aligned} d1_x &= x1_{pi} - [x1_{pi}] \\ d1_y &= y1_{pi} - [y1_{pi}] \end{aligned} \tag{42}$$

$$\begin{aligned} x1_{oi} &= x1_{pi} + (-d1_x/2) \\ x1_{or} &= (-d1_x/2) \end{aligned} \qquad \text{for} \quad d1_x <= 0.5 \tag{43}$$

or

$$\begin{aligned} x1_{oi} &= x1_{pi} + (1 - d1_x)/2 \\ x1_{or} &= (1 - d1_x)/2 \end{aligned} \qquad \text{for} \quad 0.5 < d1_x \ . \tag{44}$$

$$\begin{aligned} y1_{oi} &= y1_{pi} + (-d1_y/2) \\ y1_{or} &= (-d1_y/2) \end{aligned} \qquad \text{for} \quad d1_y <= 0.5 \tag{45}$$

or

$$\begin{aligned} y1_{oi} &= y1_{pi} + (1 - d1_y)/2 \\ y1_{or} &= (1 - d1_y)/2 \end{aligned} \qquad \text{for} \quad 0.5 < d1_y \ . \tag{46}$$

When performing $1\times$ resampling, the bilinear filtering is adopted.

Then I compute surface brightness, SB, of each pixel on $1\times$ resampled image following the equation (28) $\sim$ (32), and correct the reddening due to dust extinction in our Galaxy, using Schlegel, Finkbeiner & Davis (1998). Finally, I calculate 'pixel by pixel' K-corrected surface brightness by `kcorrect.v3_2` library (Blanton et al. 2003). The `kcorrect.v3_2` software includes two stand-alone programs, `fit_coeffs` and `reconstruct_maggies`. I read these code and incorporated our software with `kcorrect.v3_2` library. Basically the input/output of `kcorrect.v3_2` is AB maggies, i.e., $f/f0$ in equation (28), and this feature is useful to do photometry with K-correction. Therefore, users do not have to decide whether Pogson or asinh magnitude for K-correction. After pixel-to-pixel K-correction, I plot radial color profile using Pogson magnitude, and 2D colormap using asinh magnitude which minimizes noisy maps in the outskirts.

Thus, I have done almost all of photometric reductions using author's original software. Writing code takes a lot of time. However, this thesis work will be useful

for larger project in the future, and I intend to apply our software to larger sample. For this purpose, using original code will be much more adaptable and flexible.

3 Radial and 2D Color Properties of E+A Galaxies

3.1 Introduction

As is mentioned in section 1.2, most of the previous work is focused on the global properties of E+A galaxies. Needless to say, it is also indispensable to investigate internal properties of E+A galaxies such as age and metallicity gradients, to solve the E+A mystery. Do E+A galaxies leave the traces of merger/interaction? Where do the traces remain, centralized or decentralized starburst? The elucidation for these questions are essential to test E+A evolution scenarios. Norton et al. (2001) performed long-slit spectroscopic observation of 21 E+A galaxies, and found young stellar populations of E+A galaxies are more centrally concentrated than the older populations, and old component of E+A galaxies conforms to the Faber-Jackson relation. Bartholomew, Rose & Gaba (2001) also reported that K+A galaxies on average tend to have slightly bluer radial gradients toward the center than the normal early-type galaxies. Yang et al. (2004) presented HST observations of five bluest E+A galaxies with $z \sim 0.1$ and reported details of disturbed morphologies and detected compact sources associated with E+A which have consistent with the brightest clusters in nearby starburst galaxies. Although these are important results, previous work often lacked a statistical significance since E+A galaxies are extremely rare. In addition, it is important to understand the spatial properties of E+A galaxies along the evolutionary sequence. Furthermore, there is a contamination problem in the E+A sample selected without using Hα. Kennicutt (1992a,b) shows, Hα is the best star formation indicator in optical wavelength since it is a strong line and it has fewer uncertainties (e.g., dust extinction, self absorption, metallicity dependence) than the other lines. Indeed, Goto (2003) reported that an E+A sample without Hα cut-off contains $\sim$50% of contamination. Blake et al. (2004) also found that the criterion using Hδ and [OII] leads to a significant sub-population of disk systems with detectable Hα emission. We stress that a clean sample selection is essential in order to study a rare population of galaxies such as E+As.

In this section, we use publicly available *true* E+A galaxies (without Hα nor [OII] emission) selected from the Sloan Digital Sky Survey (SDSS, York et al. 2000; Early Data Release, Stoughton et al. 2002, hereafter EDR; First Data Release, Abazajian et al. 2003, hereafter DR1; Second Data Release, Abazajian et al. 2004, hereafter DR2) by Goto (2005). Both of the broad-band imaging and the spectroscopic survey

of 10,000 deg^2 of SDSS provides us with the first opportunity to study E+A galaxies in a much large number. Goto (2005) analyzed ∼250,000 galaxy spectra in the DR2, and the number of E+A homogeneous sample attained to 266. The SDSS imaging is somewhat poor (typical seeing size is ∼1.5″) compared with 8m-class telescopes or HST, but this 266 sample includes very nearby or large E+A galaxies like Figure 33 which exhibits dramatic tidal tails or conspicuous disturbed morphologies. We then select 22 E+A galaxies with $z < 0.2$, large apparent size, and more strict criteria 5.5Å $< H\delta$ EW, -1.0Å $<$ Hα EW and -2.5Å $<$ OII EW (a positive sign is absorption), and investigate spatial properties; 2D colormap and $g-r$ and $r-i$ radial color gradients. The radial color gradients are compared with spectroscopic properties, and we compare these properties with evolution scenarios using a SED model in order to understand the evolutionary sequence of E+A galaxies.

This section is organized as follows: In section 3.2, the definitions of two galaxy

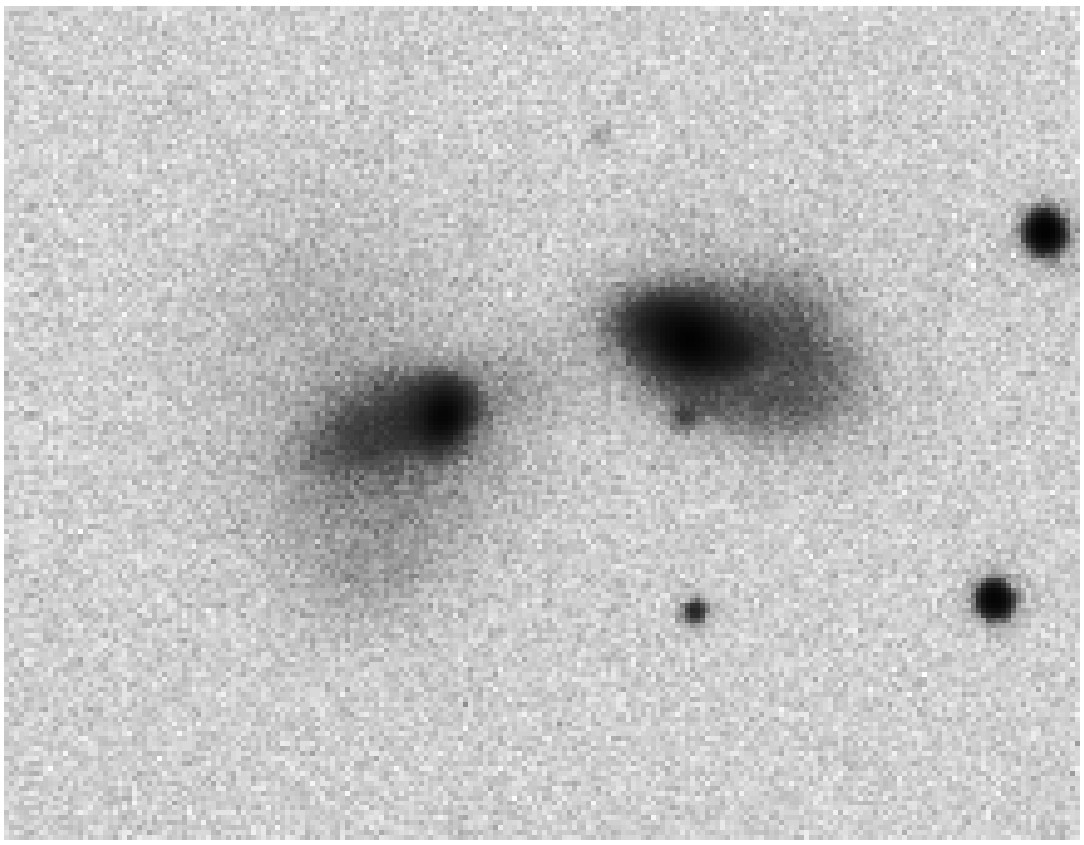

Figure 33: SDSS r-band image of one of the nearest E+A galaxies (left;z=0.034) captured from the SDSS DR2 sample. The image size is 86.3 arcsec × 66.9 arcsec. Note the dramatic tidal tails.

samples are summarized, as well as the spectroscopic and imaging data. In section 3.3, we explain the reduction of the imaging data, e.g., an image convolution, position matching between passbands, a review of concentration index and the definition of radial color gradient. In section 3.4, we briefly describe our E+A morphologies, and study 2D $g-r$ and $r-i$ color properties, 2D colormaps and radial color gradients, with relations to other photometric/spectroscopic properties. We then investigate the evolution scenario for E+A radial color gradients using comparison between a SED model and our observational data. In section 3.5, we discuss our results with other E+A-related studies. The cosmological parameters adopted throughout this section are $H_0 = 75 \mathrm{kms}^{-1}\mathrm{Mpc}^{-1}$, and $(\Omega_m, \Omega_\Lambda, \Omega_k) = (0.3, 0.7, 0.0)$.

3.2 Data Samples

Our E+A galaxies are selected from the publicly available catalog described in Goto (2005). The mother sample of this catalog contains ∼250,000 objects classified as galaxies with spectroscopic information in SDSS DR2 (Abazajian et al. 2004). Goto (2005) selected 266 E+A galaxies as those with 5.0Å $<$ Hδ EW, -3.0Å $<$ Hα EW and -2.5Å $<$ [OII] EW (absorption lines have a positive sign) after redshift (> 0.01) and S/N (>10 per pixel) cut-off.

We have restricted our targets to those galaxies which have redshift z less than 0.2 and apparent size a_{60} (Petrosian 60% flux semi-major axis; described in section 3.3) more than $2.82''$ to keep enough sampling points for radial color gradients. This selection leaves the 50 E+A galaxies. To minimize contamination of our E+A galaxies with a remaining star formation activity, we set more strict spectroscopic criteria 5.5Å $<$ Hδ EW and -1.0Å $<$ Hα EW, and the number of these higher purity of E+A galaxies becomes 22, finally.

We also randomly selected normal 50 early-type galaxies within $z < 0.2$ as a control sample from objects classified as galaxies in the SDSS DR2 catalog. The normal early-type galaxies are selected by the elliptical-based concentration index, C_e (Yamauchi et al. 2004), a ratio of Petrosian 50% flux semi-major axis to 90% flux semi-major axis (See section 3.3); $C_e < 0.33$ for early-type galaxies (Shimasaku et al. 2001). Although the standard (inverse) concentration index $C = r_{50}/r_{90}$ defined with the Petrosian flux in the circular apertures is significantly affected by inclination, the effect of inclination is removed with the use of elliptical apertures (Yamauchi et al. 2004). The a_{60} for size cut-off is the same as that of E+A galaxies. But this subsample contains 1 galaxy with deblending problem, which we eliminated.

Finally, we use 49 normal early-type galaxies as a control sample.

The spectroscopic data, Hδ, Hα and [OII] equivalent width (EWs) and their errors are measured by the flux summing method described in Goto (2005) (See also Goto et al. 2003c). The values of 4000Å break(D_{4000}) in our study are the reciprocal numbers of values in the SDSS catalog. We use DR2 atlas images (Stoughton et al. 2002) as imaging data to calculate 2D colormaps and radial color gradients of $g-r$ and $r-i$, and concentration index C_e. The photometric system, imaging hardware and astrometric calibration of SDSS are described in detail elsewhere (Fukugita et al. 1996; Gunn et al. 1998; Hogg et al. 2001; Smith et al. 2002; Pier et al. 2003).

3.3 Data Reductions

Photometric reductions are done by author's original software. The details of photometry in this thesis are presented in section 2.5. In this subsection, we briefly describe data reduction technique for this study.

From the SDSS database, we can easily download the deblended galaxy images, called atlas images, by fpAtlas file in which images are archived using the Rice compression. In the SDSS images, however, the seeing sizes differ from passband to passband, and the relation between physical and imaging position of a passband on Atlas image is not equal to others but slightly differs. Therefore, we cannot directly compose g- and r-band images, or r- and i-band images using the coordinates given by the fpAtlas file. We adjust the positions of the multi-band images in the following way.

First, we smear all images except that with the worst seeing $\sigma_{\max}$ among the passbands to equalize seeing sizes of all passbands. Assuming that point-spread function is Gaussian function, images are convolved with Gaussian function of $\sigma_{\rm c}$,

$$\sigma_{\rm c} = \sqrt{\sigma_{\max}^2 - \sigma^2}, \tag{47}$$

where σ is the actual seeing of each image derived from `psf_width` parameter in tsField files:

$$\sigma = (\texttt{psf\_width}/1.06)/2.35, \tag{48}$$

where `psf_width` is equivalent to 1.06 FWHM for a Gaussian profile (Fan et al. 2003).

Next, each passband image are resampled using positional information, "`colc`" and "`rowc`"(real) in tsObj file, and "offsets wrt[8)] reference color"(`dcol` and `drow`;

[8)] with reference to

integer) and "bounding box"(`cmin` and `rmin`; integer) in "master mask" in fpAtlas file (see source code of readAtlasImages). Where "`colc`" and "`rowc`" are the exact center position of object in fpC coordinates, and $(\texttt{cmin}+\texttt{dcol}, \texttt{rmin}+\texttt{drow})$ is the fiducial point of atlas images in fpC coordinates. The typical error of "`colc`" and "`rowc`" are $0.01 \sim 0.1$ pixel($0.004 \sim 0.04$ arcsec).

In the case of making $g-r$ 2D colormap without resampling r-band image, the preliminary position offset $(x0_{pg}, y0_{pg})$ of g-band pixels needed for $1\times$ g-band resampling in atlas image coordinate is

$$\begin{aligned} x0_{pg} &= (\texttt{colc}_g - \texttt{col0}_g) - (\texttt{colc}_r - \texttt{col0}_r) \\ y0_{pg} &= (\texttt{rowc}_g - \texttt{row0}_g) - (\texttt{rowc}_r - \texttt{row0}_r) \ , \end{aligned} \tag{49}$$

where $\texttt{col0} = \texttt{cmin} + \texttt{dcol}$ and $\texttt{row0} = \texttt{rmin} + \texttt{drow}$. And we consider the values $(d0_x, d0_y)$:

$$\begin{aligned} d0_x &= x0_{pg} - [x0_{pg}] \\ d0_y &= y0_{pg} - [y0_{pg}] \end{aligned} \tag{50}$$

where $[x]$ is the floor function and $(d0_x, d0_y)$ indicates a distance from pixel grid and resampled position of g-band pixels (That is, the resampling is not required when $(d0_x, d0_y) = (0, 0)$).

Resampling only g-band image is not reasonable. Both r- and g-band should be resampled and optimized. Then we determine the position offsets by $d0_x$,

$$\begin{aligned} x0_{og} &= x0_{pg} + (-d0_x/2) \\ x0_{or} &= (-d0_x/2) \end{aligned} \qquad \text{for} \quad d0_x <= 0.5 \tag{51}$$

or

$$\begin{aligned} x0_{og} &= x0_{pg} + (1 - d0_x)/2 \\ x0_{or} &= (1 - d0_x)/2 \end{aligned} \qquad \text{for} \quad 0.5 < d0_x \ , \tag{52}$$

and by $d0_y$,

$$\begin{aligned} y0_{og} &= y0_{pg} + (-d0_y/2) \\ y0_{or} &= (-d0_y/2) \end{aligned} \qquad \text{for} \quad d0_y <= 0.5 \tag{53}$$

or

$$\begin{aligned} y0_{og} &= y0_{pg} + (1 - d0_y)/2 \\ y0_{or} &= (1 - d0_y)/2 \end{aligned} \qquad \text{for} \quad 0.5 < d0_y \ . \tag{54}$$

These position offsets minimize declines of the resolution in r- and g-band images. The position offsets of u-, i- and z-band, $x0_{ou}$, $x0_{oi}$ and $x0_{oz}$, are also derived by equation (51) or (52), and (53) or (54) with replacing g with u, i or z. The $x0_{pu}$, $x0_{pi}$ and $x0_{pz}$ are calculated by equation (49) with replacing g with u, i or z (Note that equation (50) is applied for g-band only). In the case of $r-i$ 2D colormap,

$x1_{oi}$, $y1_{oi}$, $x1_{or}$ and $y1_{or}$ are calculated in the same convention. When performing $1\times$ resampling, the bilinear filtering is adopted.

Then we compute surface brightness SB of each pixel on $1\times$ resampled image and correct the reddening due to dust extinction in our Galaxy, using Schlegel, Finkbeiner & Davis (1998). The SDSS magnitudes m is derived by the following equations used in the SDSS photometric pipeline (PHOTO; Lupton et al. 2001),

$$f/f0 = N_{\rm cnt}/T_{\rm exp} \cdot 10^{0.4(v_{\rm aa}+v_{\rm kk}\cdot v_{\rm air})} \tag{55}$$

$$m_{\rm asinh} = -\frac{2.5}{\ln 10}\cdot\left\{\mathrm{asinh}\left(\frac{f/f0}{2b}\right)+\ln b\right\} \tag{56}$$

$$m_{\rm Pogson} = -2.5\cdot\log(f/f0) \tag{57}$$

where $N_{\rm cnt}$ is counts within an aperture on atlas image, $T_{\rm exp}$ is exposure time in the fpC file, $v_{\rm aa}$, $v_{\rm kk}$ and $v_{\rm air}$ are zeropoint, extinction coefficient and airmass in tsField file, and b is the asinh softening parameters. See DR2 Photometric Flux Calibration page (http://www.sdss.org/dr2/algorithms/fluxcal.html) for detail of computing magnitude from SDSS CCD images. Finally, we calculate 'pixel by pixel' K-corrected surface brightness by `kcorrect.v3_2` library (Blanton et al. 2003).

The concentration index C_e is computed by r-band image using elliptical aperture which eliminates the effect of apparent axis ratio of galaxy. The details of the effect and method of deriving axis ratio and position angle are described in Yamauchi et al. (2004). To calculate the concentration index C_e for the ellipse, we consider the area $A_e(a)$ of the ellipse of the semi-major axis a and axis ratio α, and the integrated flux $F_e(a)$ within $A_e(a)$. The Petrosian semi-major axis $a_{\rm P}$ for a given η is defined by

$$\eta=\frac{\{F_e(1.25a_{\rm P})-F_e(0.8a_{\rm P})\}/\{A_e(1.25a_{\rm P})-{\rm A_e(0.8a_P)}\}}{F_e(a_{\rm P})/A_e(a_{\rm P})}, \tag{58}$$

where we take $\eta = 0.2$, and the elliptical Petrosian flux $F_{\rm P}$ as

$$F_{\rm P} = F_e(ka_{\rm P}) \tag{59}$$

with k set equal to 2, following the SDSS definition (Strauss et al. 2002). The Petrosian half-, 60%- and 90%-light semi-major axes a_{50}, a_{60} and a_{90} are defined in a way such that the flux in the elliptical apertures of these semi-major axes are 50%, 60% and 90% of the elliptical Petrosian flux:

$$F_e(a_{50}) = 0.5F_{\rm P},\quad F_e(a_{60}) = 0.6F_{\rm P},\quad F_e(a_{90}) = 0.9F_{\rm P}\ . \tag{60}$$

We define our concentration index C_e by

$$C_e = a_{50}/a_{90} \ . \tag{61}$$

The axis ratio and the position angle used in above are also adopted to calculation of radial color gradient.

The radial color gradients are based on our pixel-to-pixel K-corrected $g-r$ and $r-i$ 2D colormap with Pogson magnitude. The regression lines to radial color ($SB_g - SB_r$) and ($SB_r - SB_i$),

$$\begin{array}{rcl} (SB_g - SB_r) & = & t + CI_{g\text{-}r} \cdot \log(a/a_{60}) \\ (SB_r - SB_i) & = & t + CI_{r\text{-}i} \cdot \log(a/a_{60}), \end{array} \tag{62}$$

are calculated by linear least-squares fitting, and we define $CI_{g\text{-}r}$ and $CI_{r\text{-}i}$ as the radial color gradient. Where a is the equivalent distance from galaxy center which is also corrected by the axis ratio and position angle. The Petrosian 60% flux radius corresponds to effective radius with pure de Vaucouleurs' profile. Generally the effective radius is used for the normalization for radial color gradient, but profile fitting is needed for calculating effective radius. However, some E+A's morphologies are somewhat disturbed and it is difficult to obtain a stable profile fit. Thus, we use the Petrosian 60% flux semi-major axis for stability of calculation. When this linear least-squares fitting is applied, the a/a_{60} of data points are restricted to $0.35 < a/a_{60} < 1.0$ to avoid a cusp in the galaxy center and lower S/N regions in the outskirts. The minimum size of a_{60} in our samples applied to the color gradient analysis is $2.83''$(7.14 pixels), and $a/a_{60} = 0.35$ corresponds to the diameter of $2.0''$ since typical FWHM of point-spread function of the SDSS is $\sim 1.5''$ (Shimasaku et al. 2001).

3.4 Results

3.4.1 E+A Morphologies

Since E+A galaxies have experienced the truncation of starburst fairly recently (<1 Gyr), E+A galaxies might still hold some traces in their morphology (e.g., dynamically disturbed signs). Therefore we might obtain some hint on the origins of E+A galaxies by examining their morphology.

First, we can confirm that E+A galaxies are centrally-concentrated using the concentration index C_e. In Figure 34, we show the distribution of C_e of 22 E+A galaxies. Galaxies that follow the de Vaucouleurs' law give $C_e = 0.29$ and those

with the exponential profile give 0.44, so C_e of early-type and late-type galaxies are swarming on each point, respectively (See Yamauchi et al. 2004). C_e of 21 E+A galaxies are distributed like early-type galaxies, and the median $C_e = 0.33$ is a typical value of E or S0 galaxy (Shimasaku et al. 2001; Strateva et al. 2001). Our visual inspection of the SDSS images in Table 3 also shows that our E+A galaxies are predominantly early-type galaxies. We can interpret these results as a suggestion that our all E+A galaxies are bulge-dominated systems except one galaxy.

We showed one of the most splendid SDSS E+A galaxies with a tidal feature in Figure 33. The SDSS imaging does not have high resolution (typical seeing size is $\sim$1.5″) compared with the HST or 8m-class telescopes, but our nearby or large 22 E+A galaxies make a show of dramatic tidal tails or conspicuous disturbed morphologies. We present all r-band negative images of our E+A galaxies in Figure 35 on a logarithmic flux scale with 0% to 50%. The images in Figure 35 are placed in ascending order with respect to 4000Å break(D_{4000}), and we numbered our E+A galaxies by this order. The physical size of a_{60} is displayed on i-band image (right to negative r-band image). To examine E+A morphologies, we present a image of normal elliptical galaxy in Figure 36. Comparison between Figure 36 and Figure 35 helps our examination of E+A morphologies. These 22 E+A galaxies exhibit a variety of disturbed features, ranging from what could visually be classified as a normal elliptical galaxy without disturbance (E+A No.7) to impressive tidal feature (E+A No.1). We notice that at least half of our E+A galaxies have traces of merger/interaction, and exhibit tidal feature or disturbed morphologies. If we observe our E+A galaxies with a higher resolution using an 8m-class telescope, we should be able to examine the details of these features and the fraction of E+A galaxies which leave traces of dynamically disturbed signs might increase.

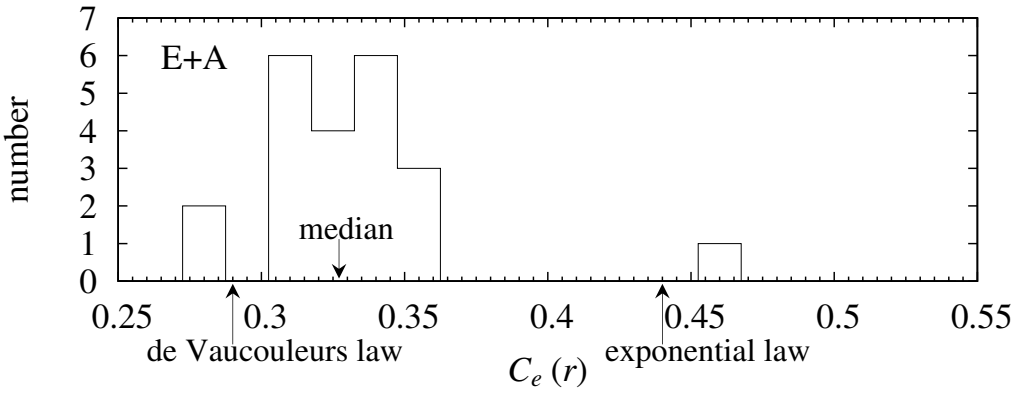

Figure 34: The distributions of concentration index C_e of 22 E+A galaxies. Galaxies that follow the de Vaucouleurs' law give $C_e = 0.29$ and those with the exponential profile give 0.44. All our E+A galaxies are centrally-concentrated galaxies except one.

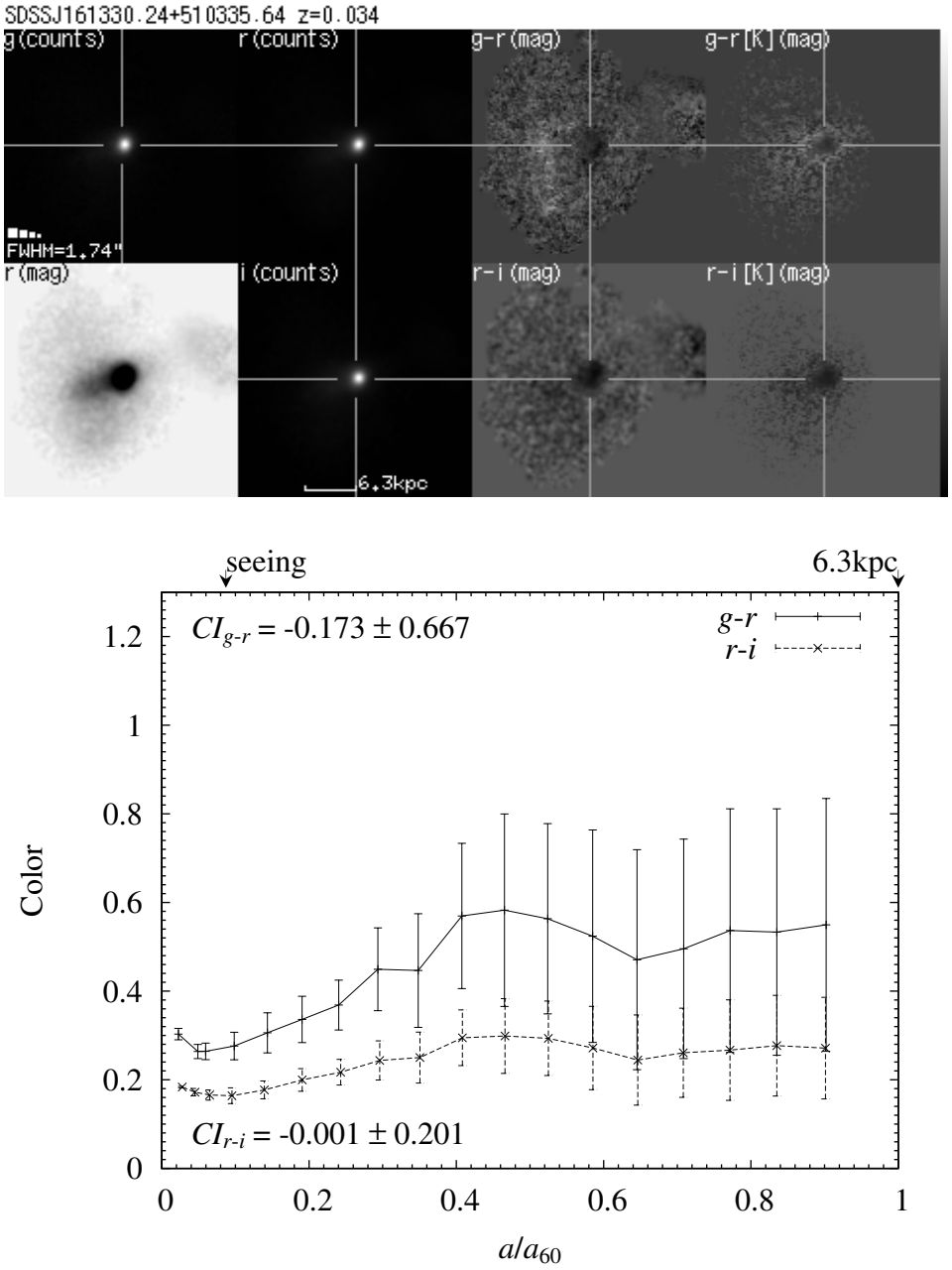

Figure 35: g-, r- and i-band images, $g-r$ and $r-i$ 2D colormaps (*top*) and the rest color profiles (*bottom*) of our all E+A galaxies. The details of explanation of image panels are inlaid in Figure 36. The panels are placed in ascending order with respect to D_{4000}. We numbered our E+A galaxies by this order, so this Figure indicates No.1 and the Figures of following pages show No.2,No.3,... and No.22 E+A galaxies. E+A galaxies with smaller D_{4000} tend to show positive slope of radial color gradients (bluer gradients toward the center) and blue irregular patterns in 2D colormap. Meanwhile, that with larger D_{4000} show negative or flat slope and moderate property in 2D colormap.

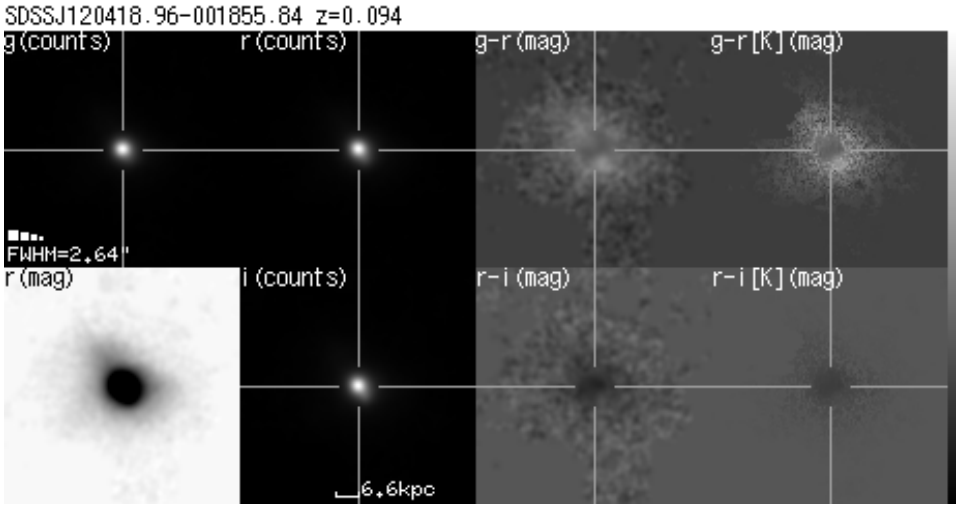

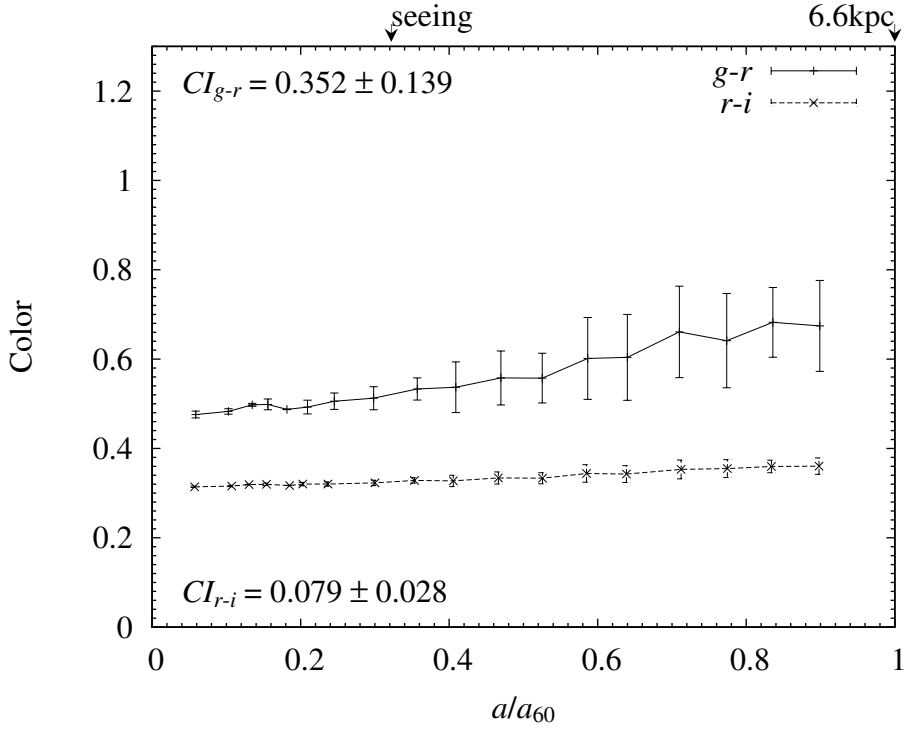

Figure 35: No.2 E+A galaxies

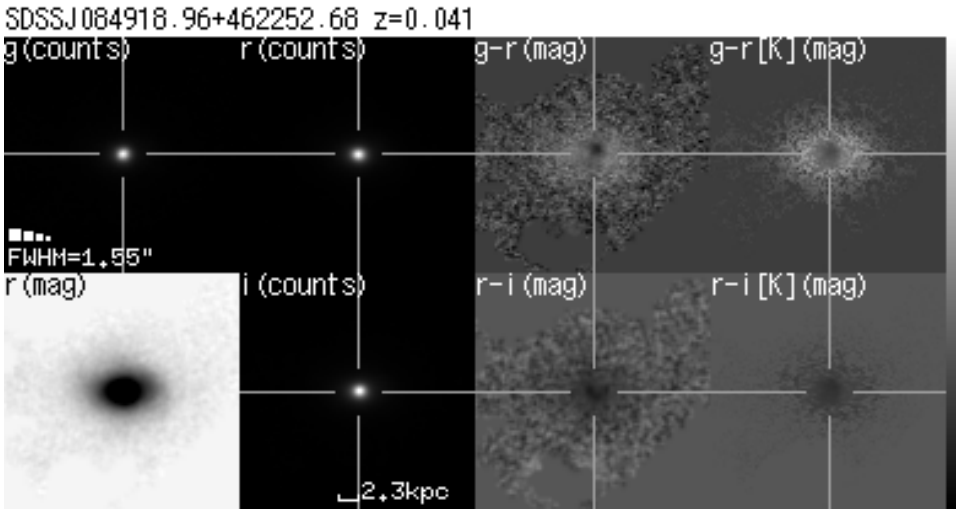

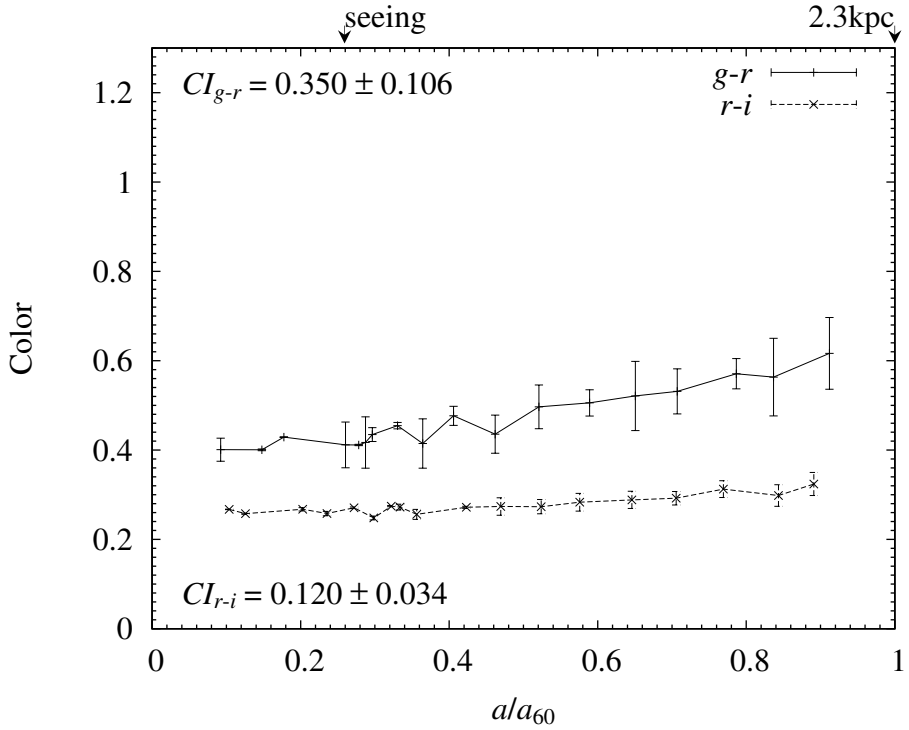

Figure 35: No.3 E+A galaxies

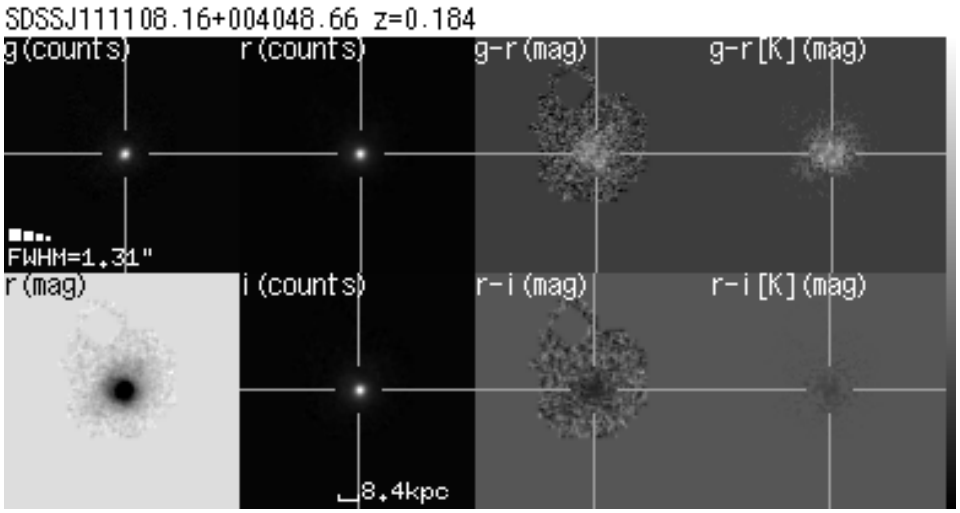

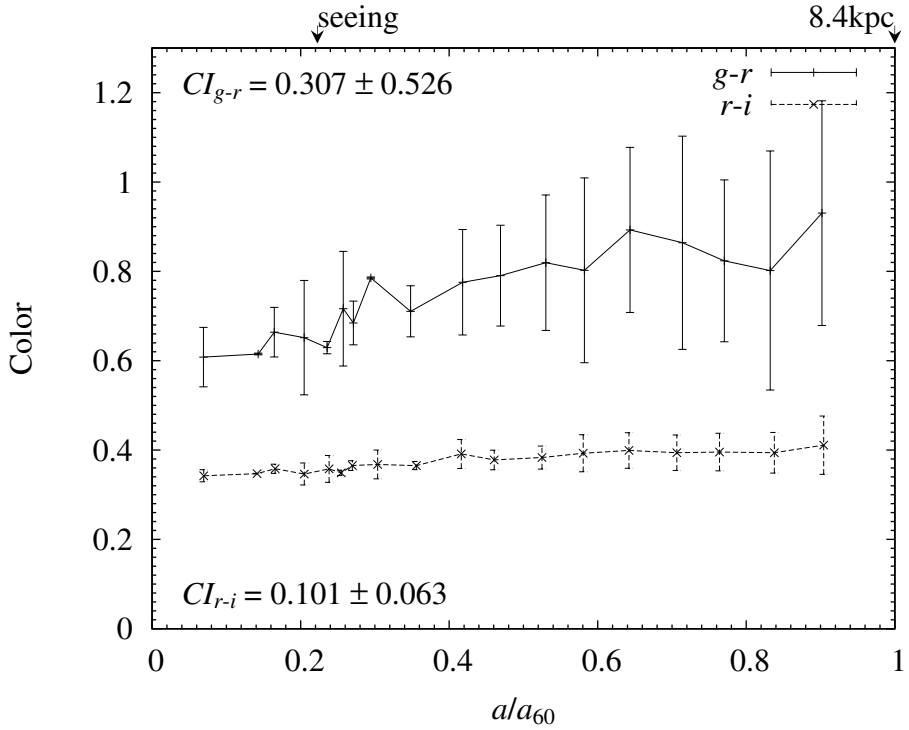

Figure 35: No.4 E+A galaxies

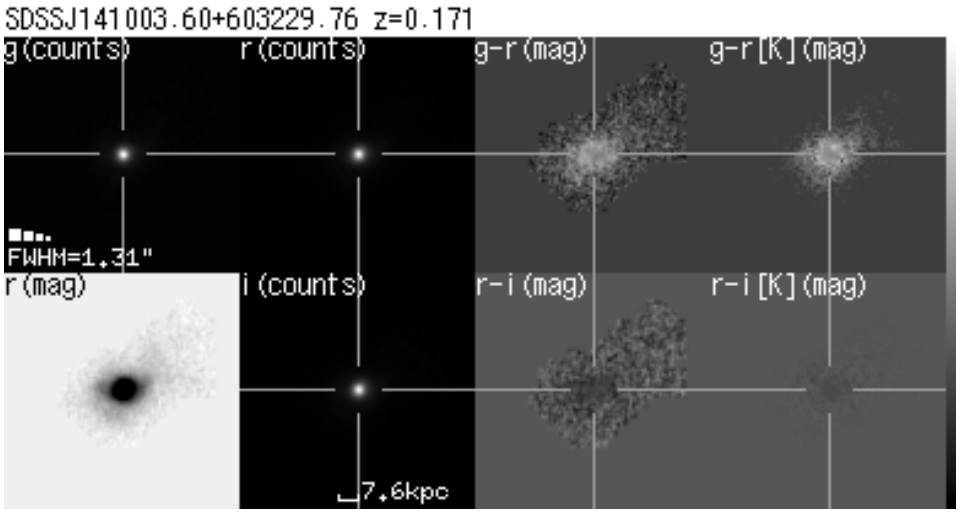

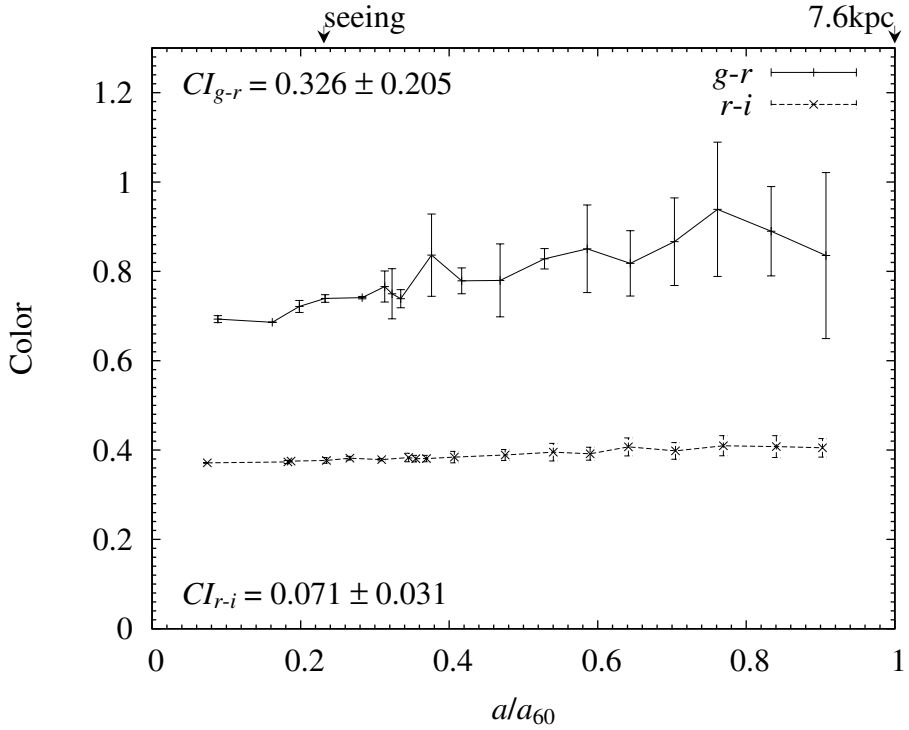

Figure 35: No.5 E+A galaxies

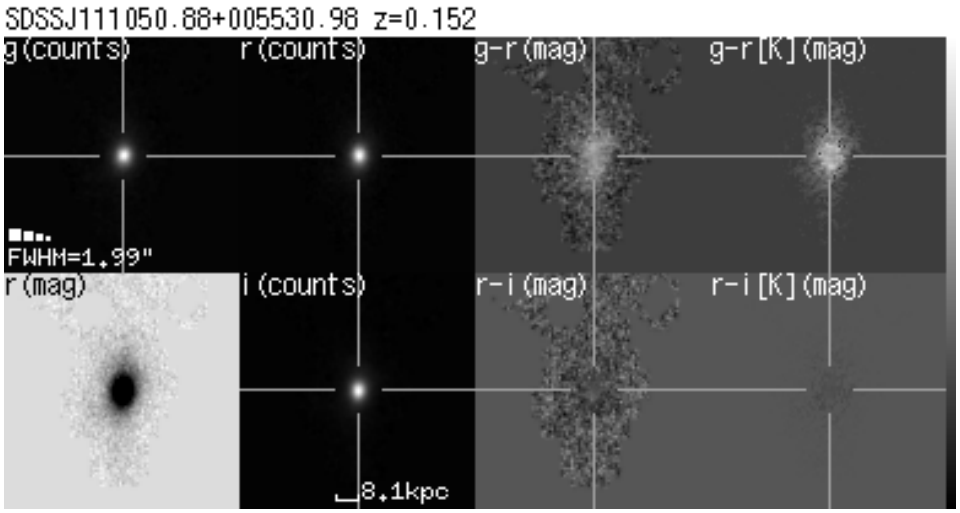

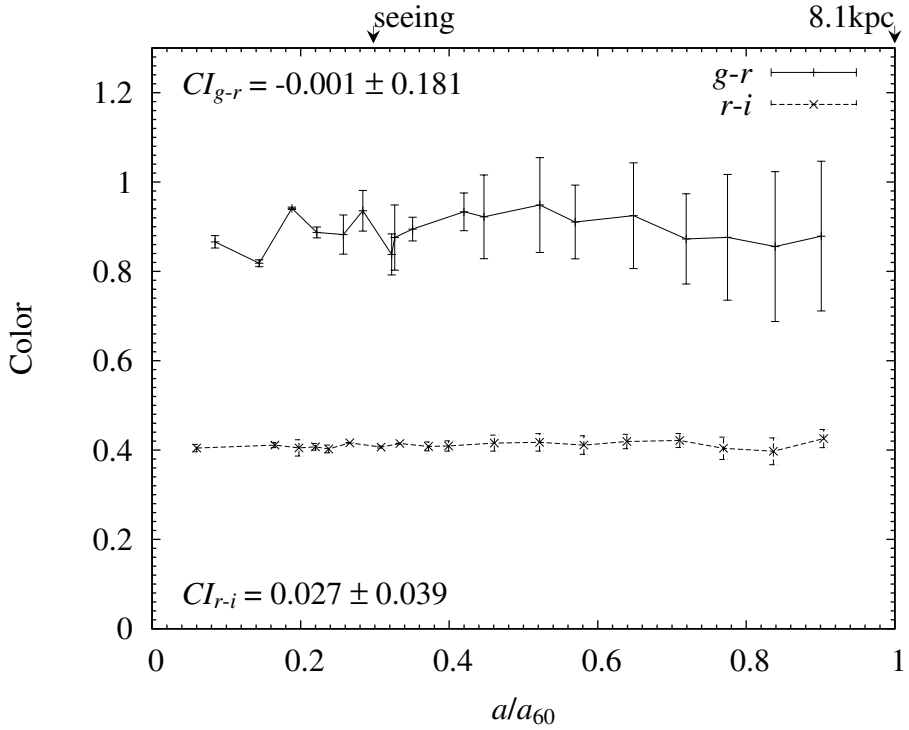

Figure 35: No.6 E+A galaxies

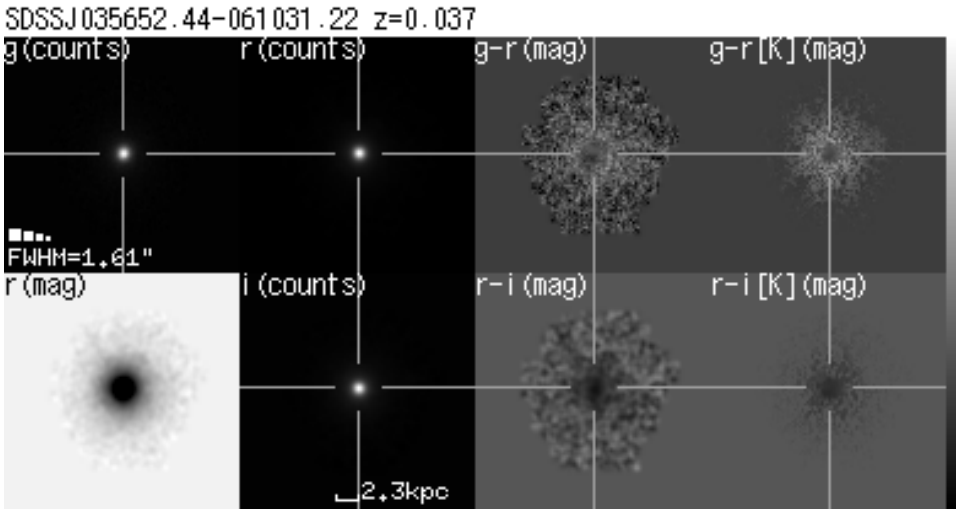

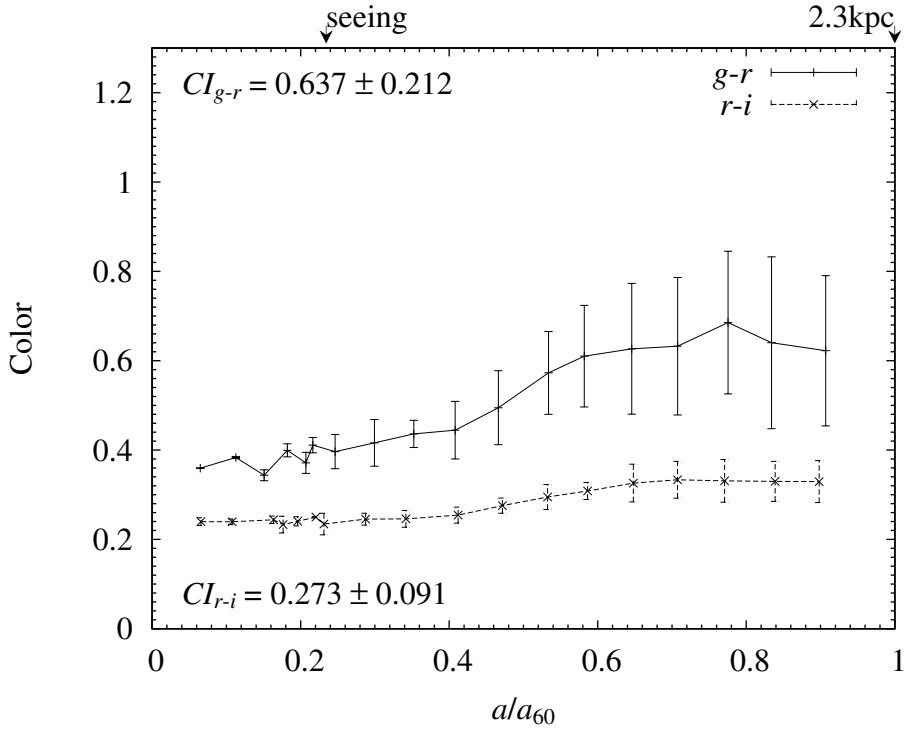

Figure 35: No.7 E+A galaxies

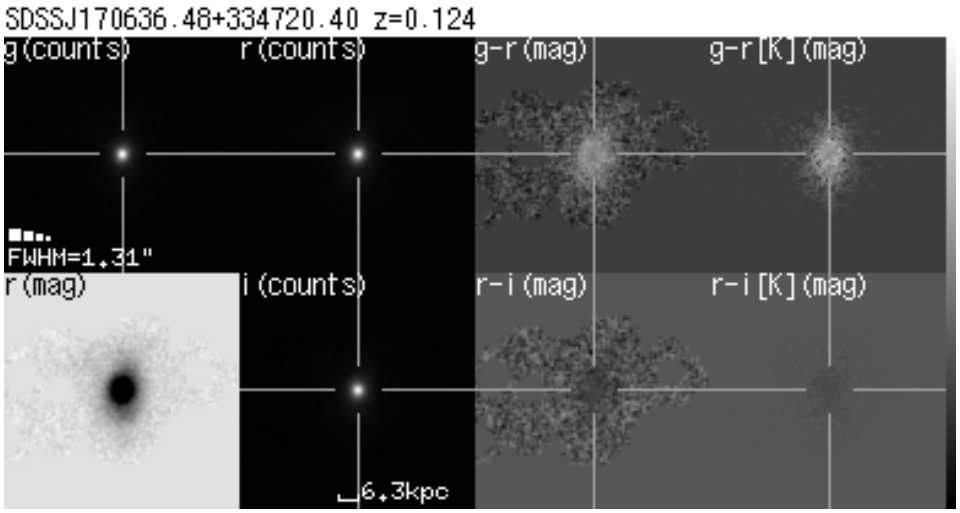

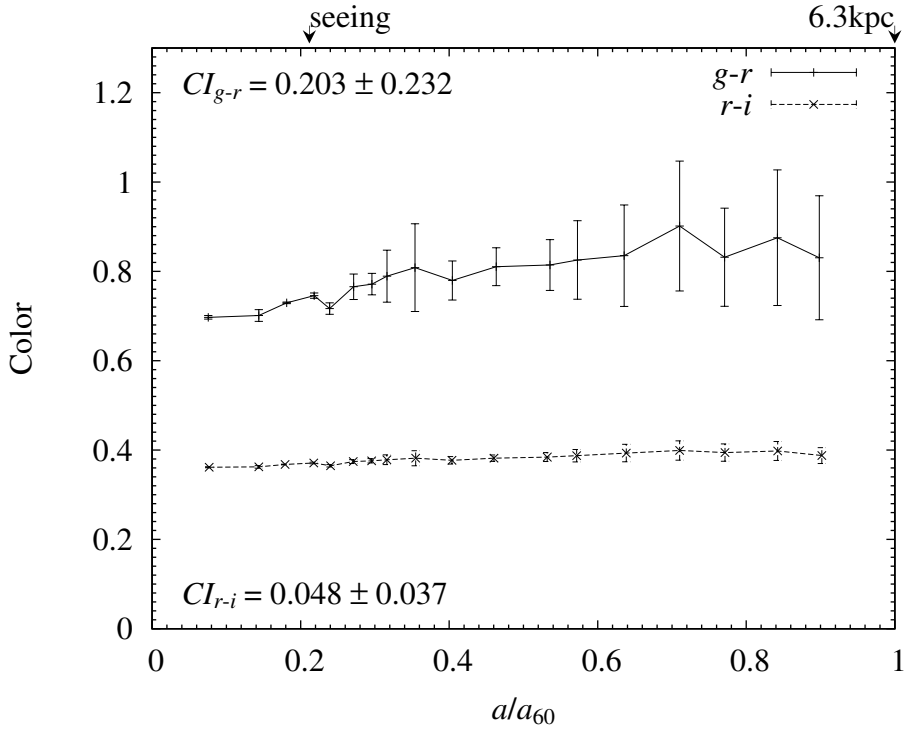

Figure 35: No.8 E+A galaxies

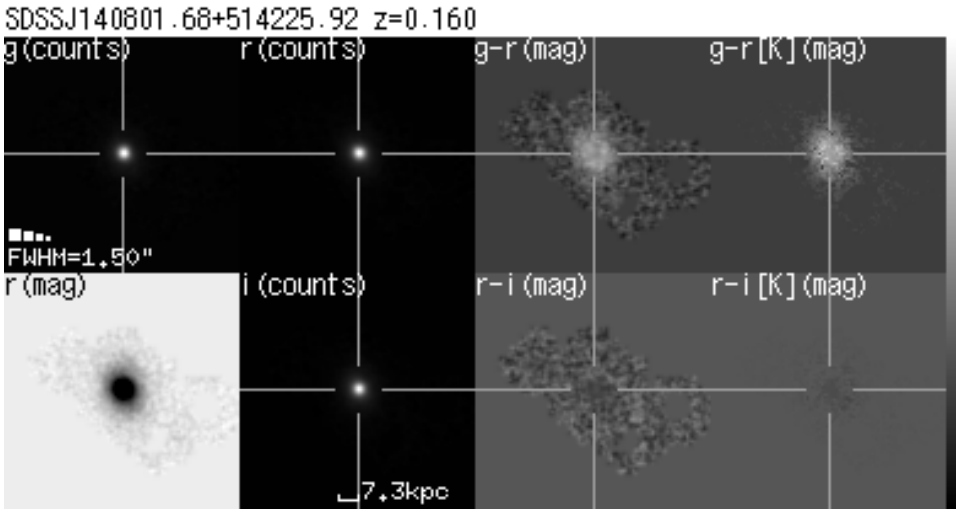

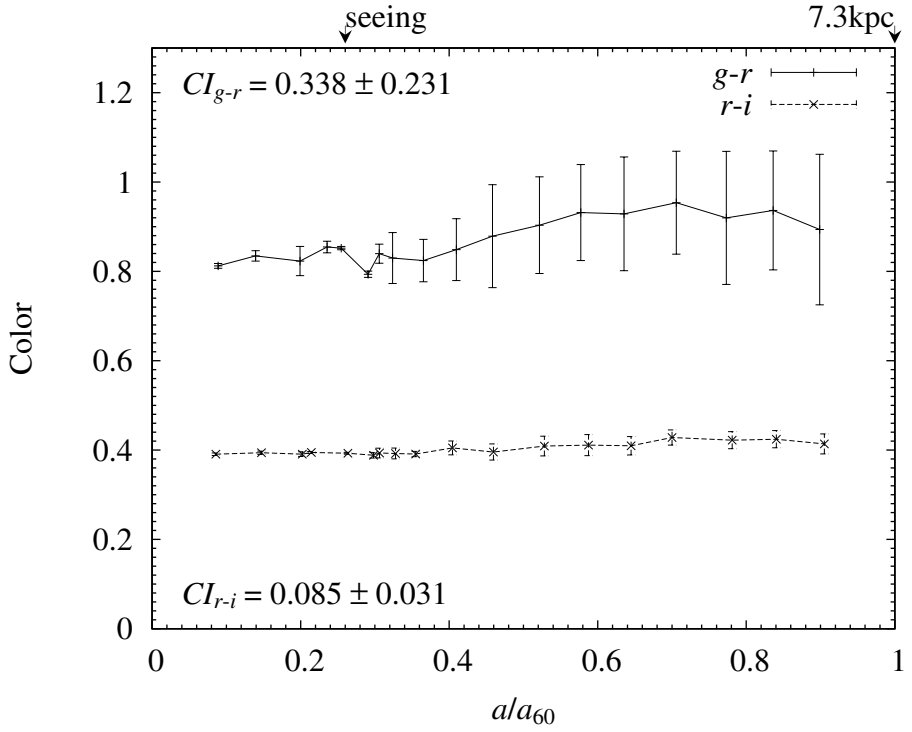

Figure 35: No.9 E+A galaxies

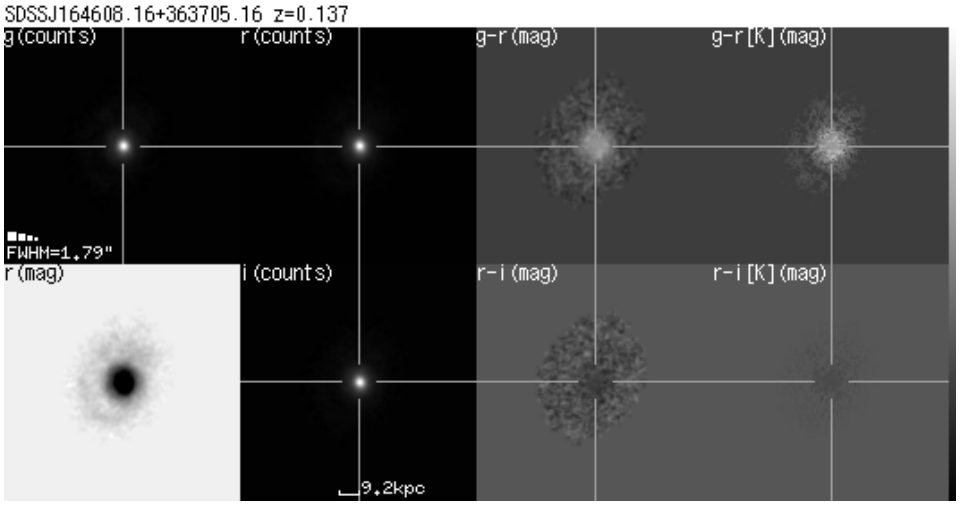

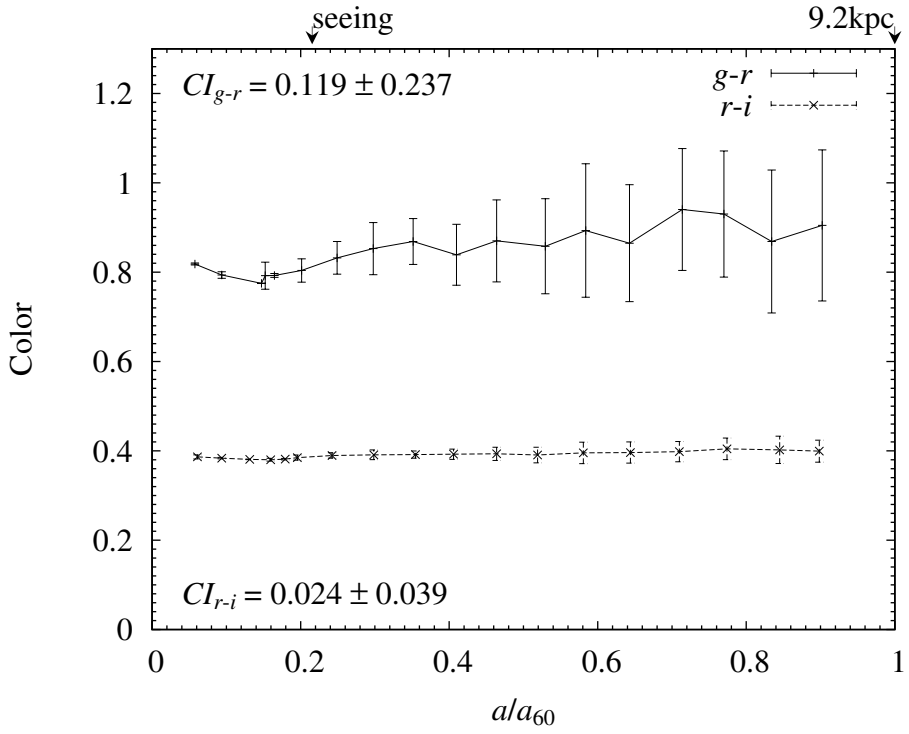

Figure 35: No.10 E+A galaxies

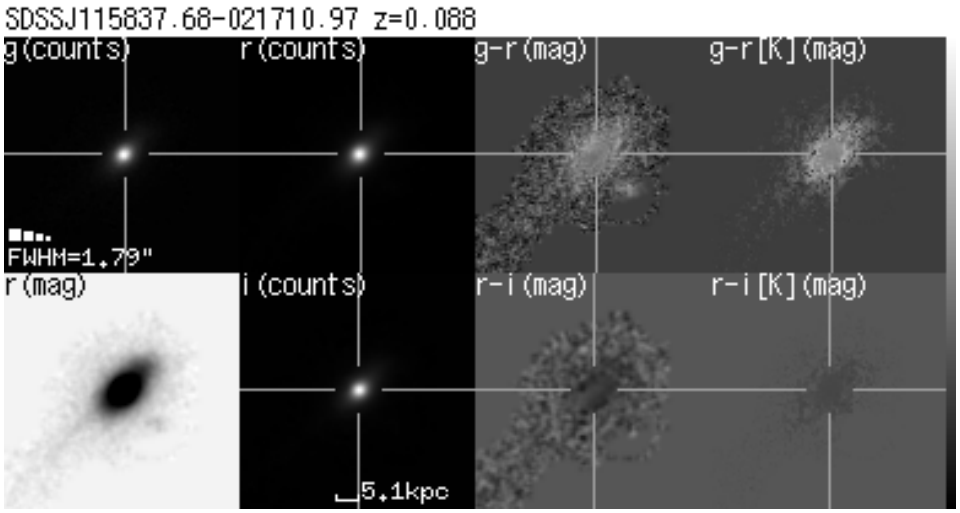

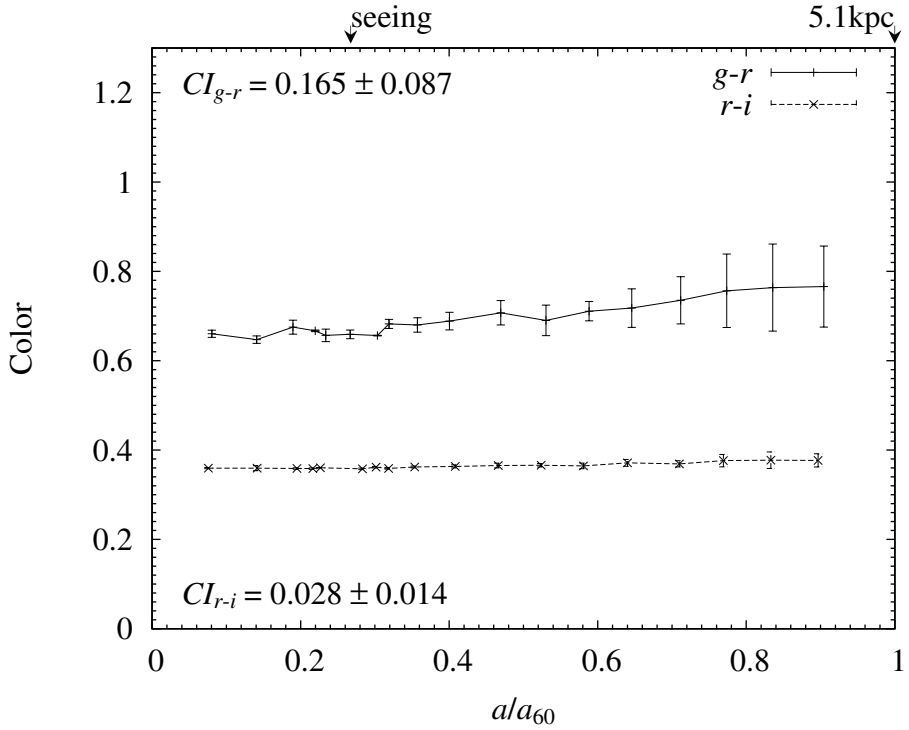

Figure 35: No.11 E+A galaxies

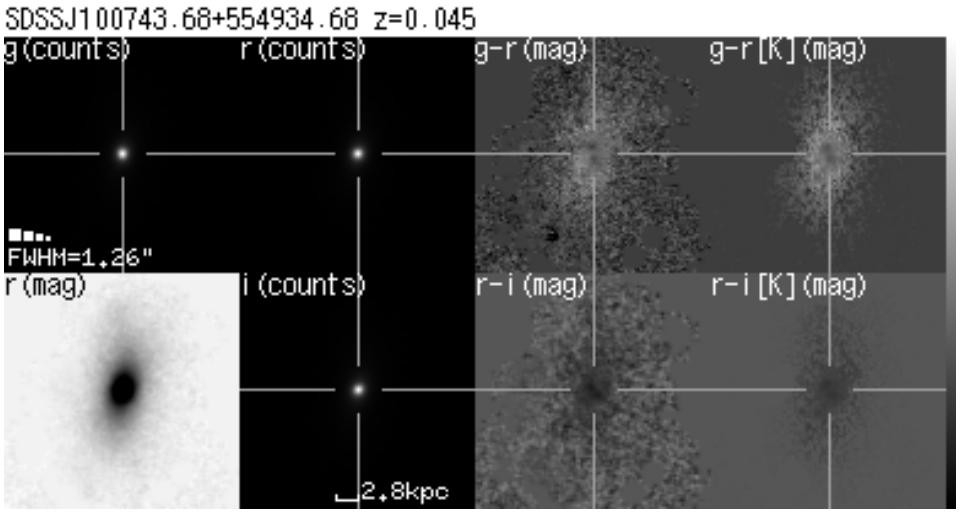

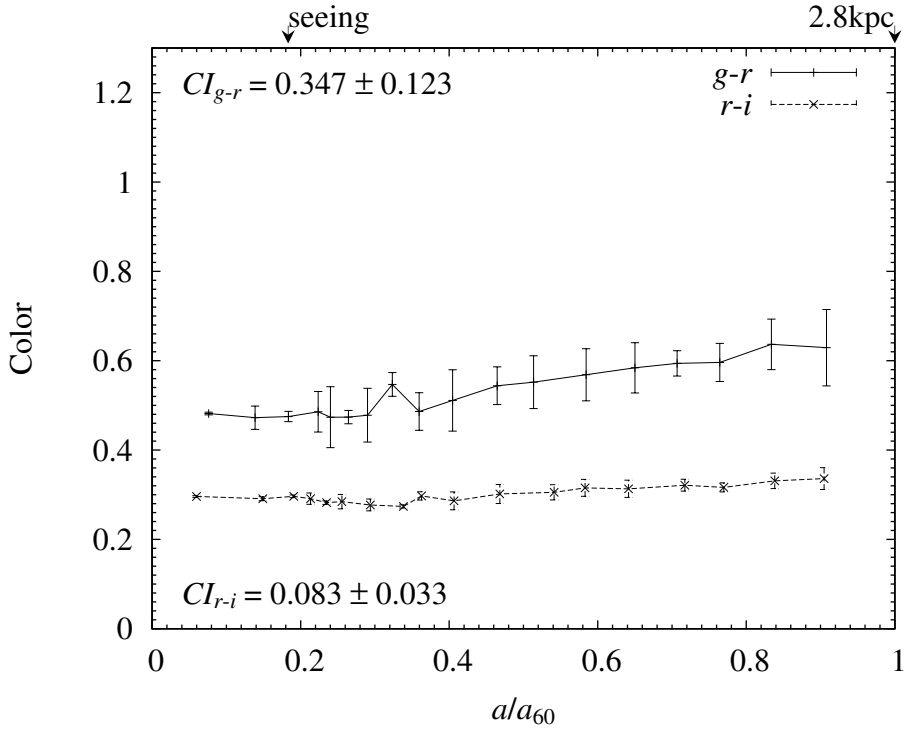

Figure 35: No.12 E+A galaxies

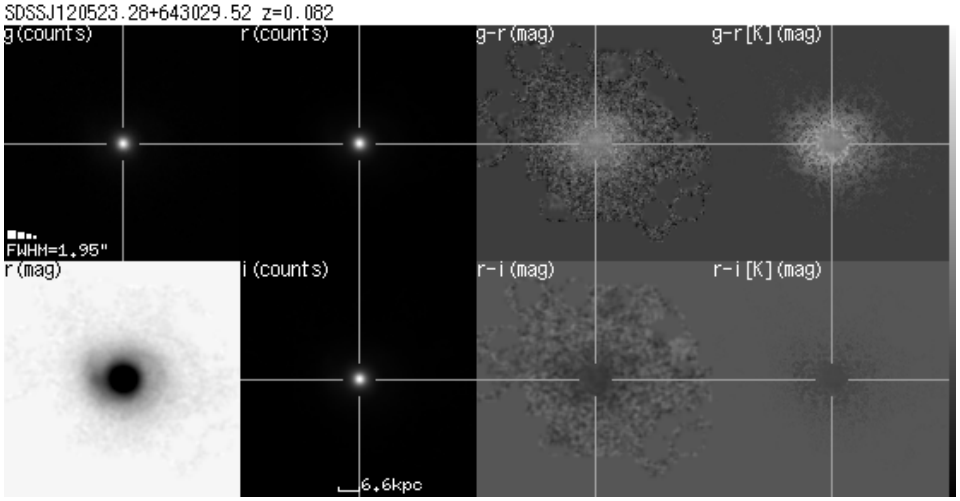

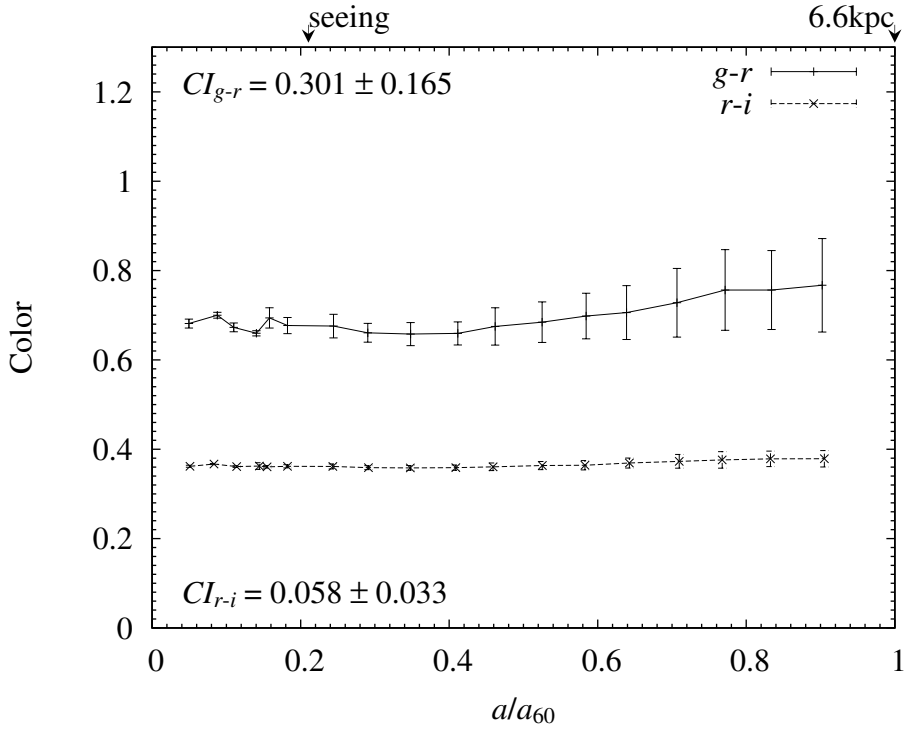

Figure 35: No.13 E+A galaxies

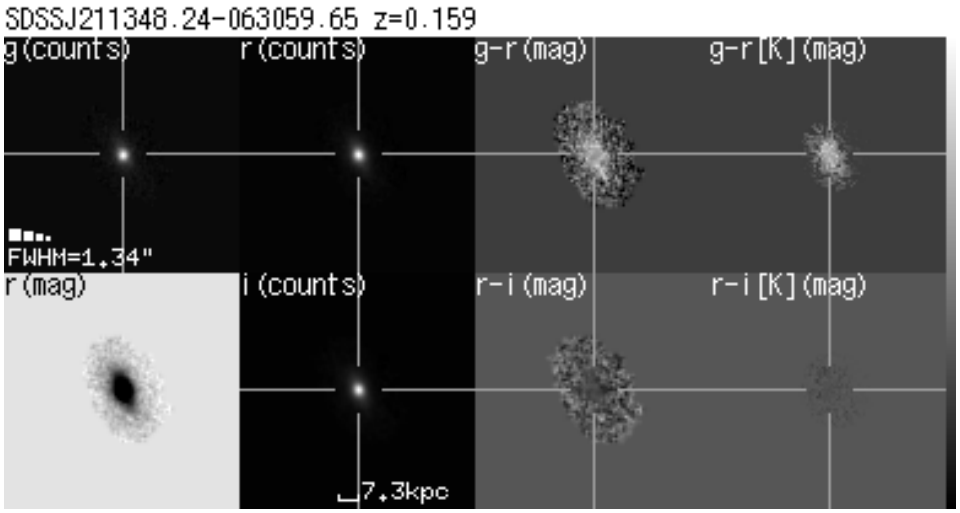

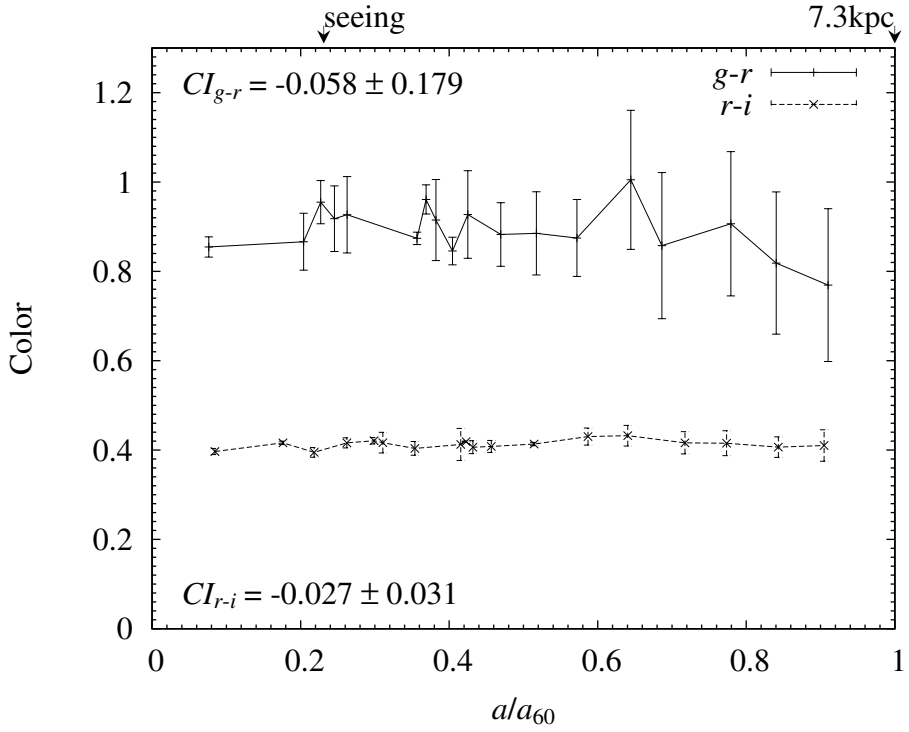

Figure 35: No.14 E+A galaxies

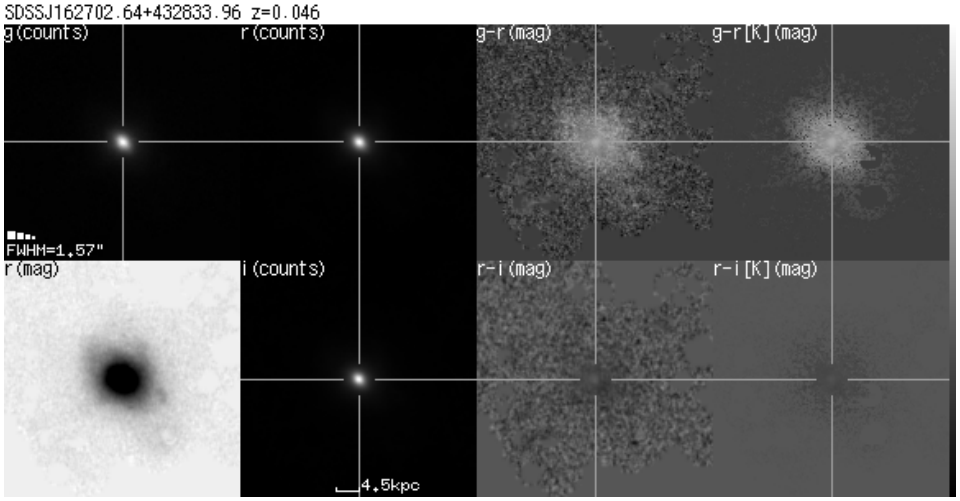

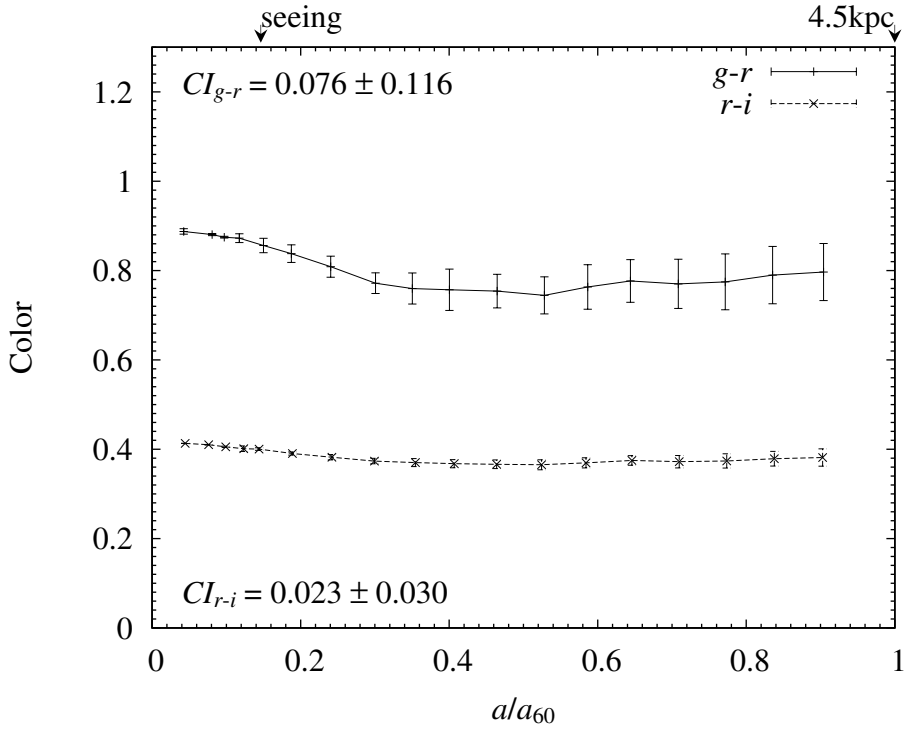

Figure 35: No.15 E+A galaxies

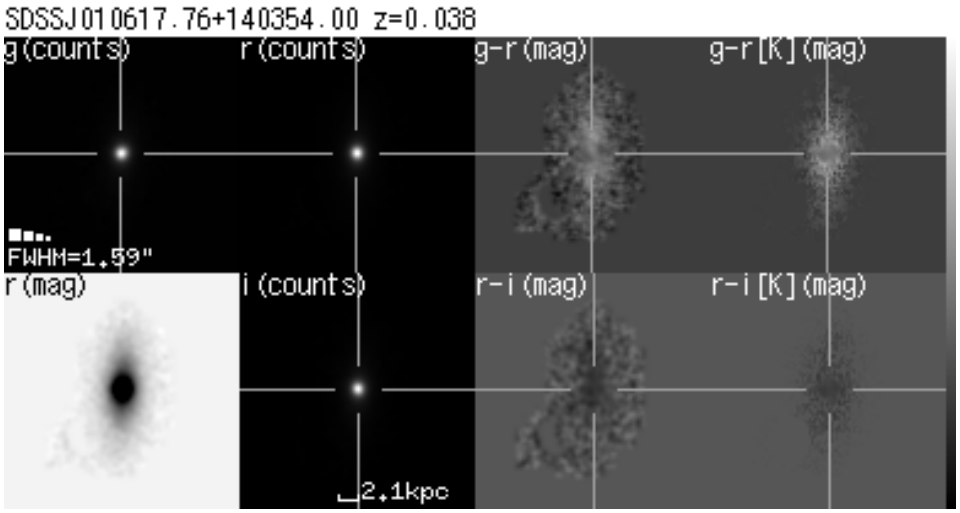

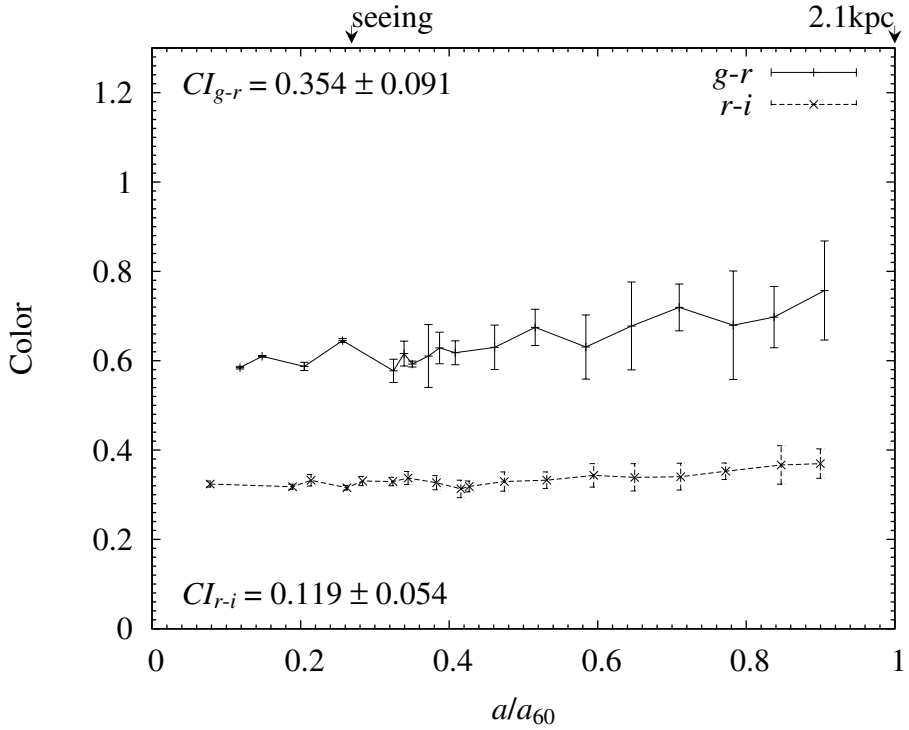

Figure 35: No.16 E+A galaxies

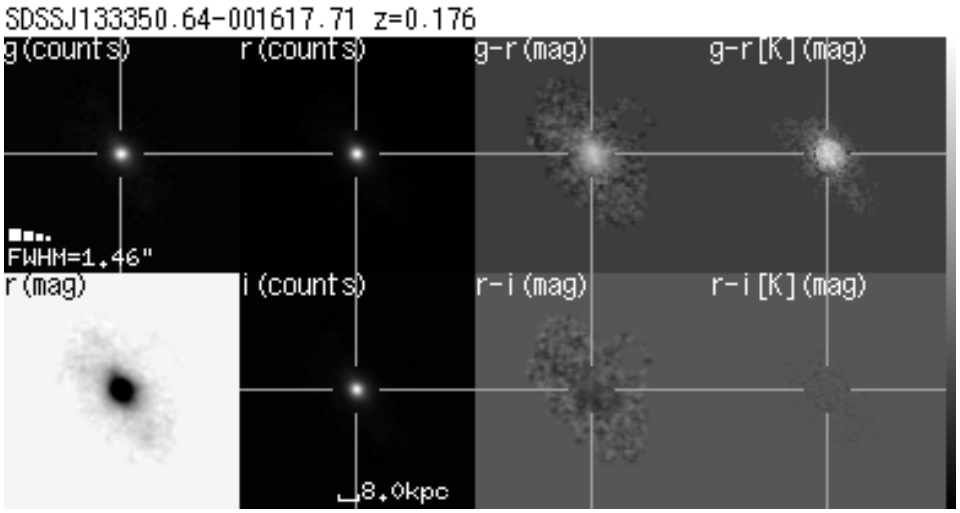

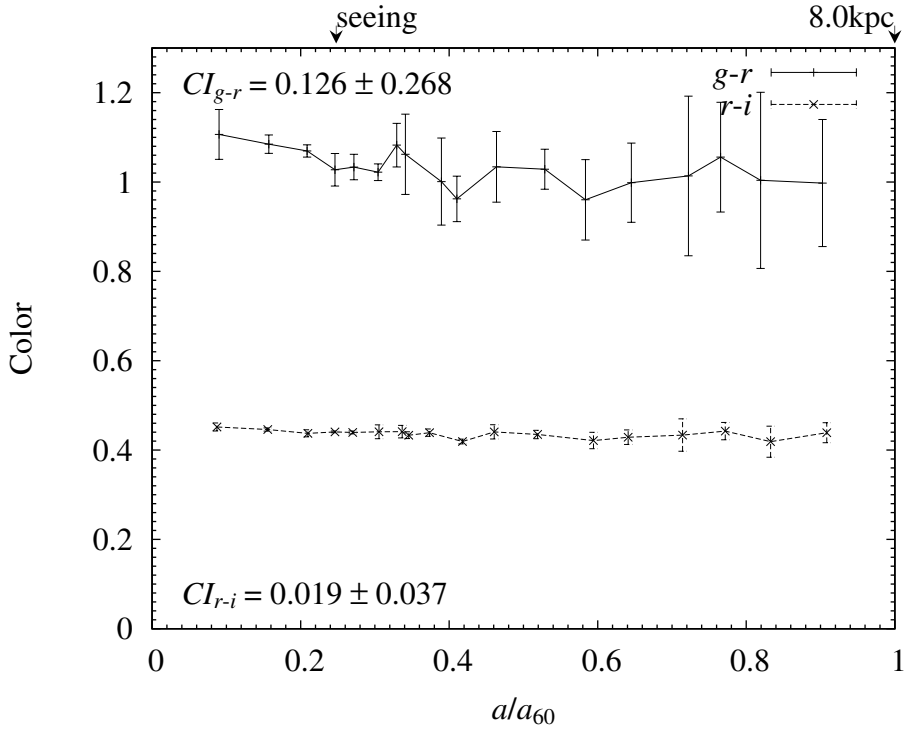

Figure 35: No.17 E+A galaxies

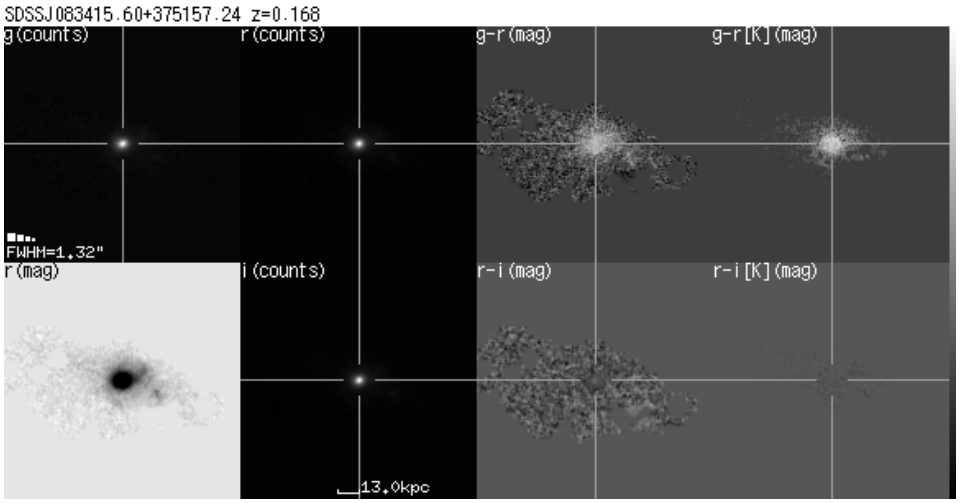

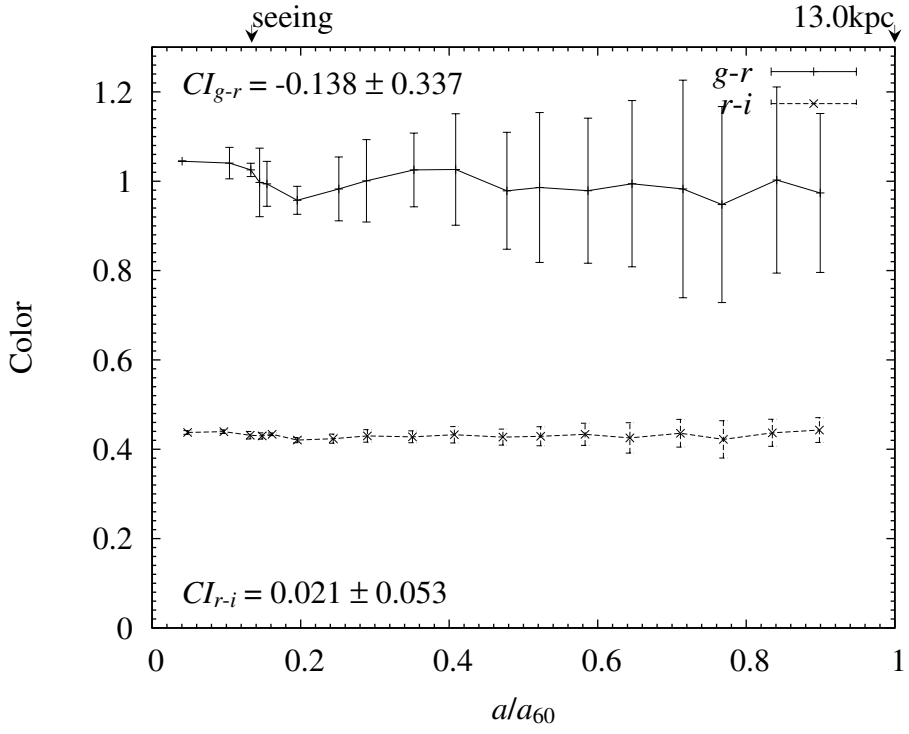

Figure 35: No.18 E+A galaxies

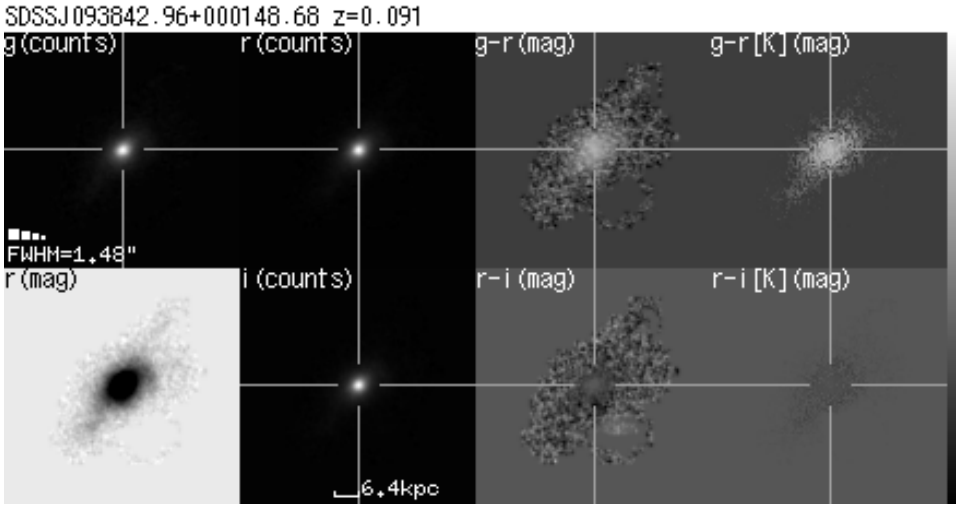

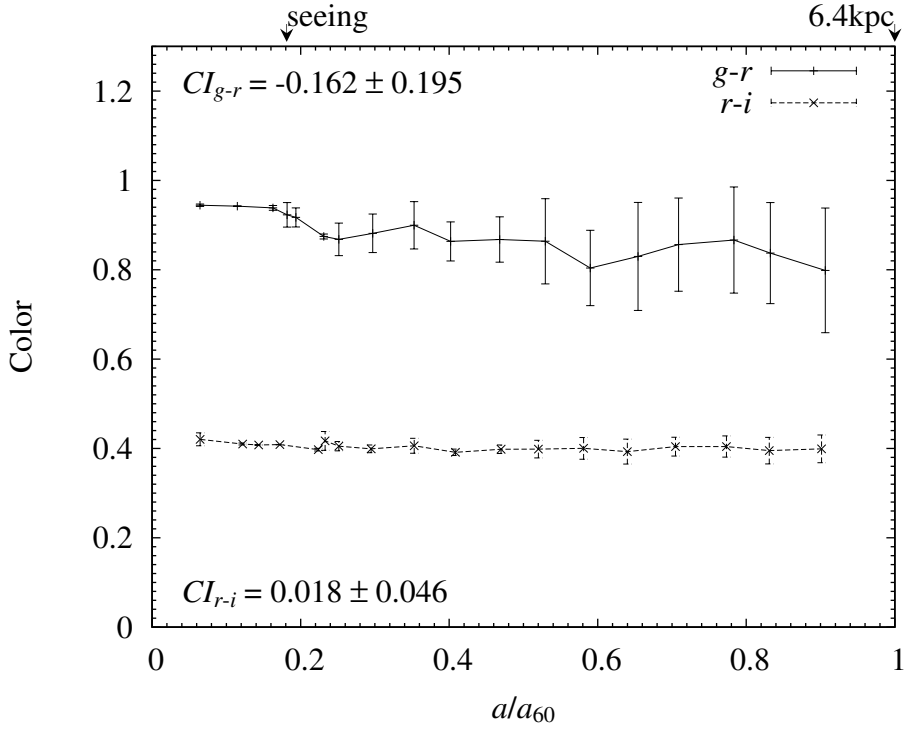

Figure 35: No.19 E+A galaxies

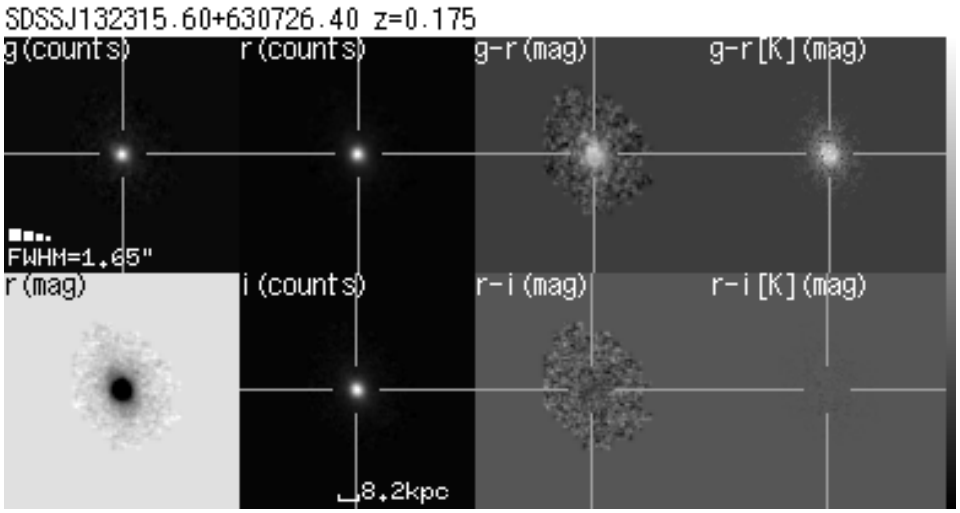

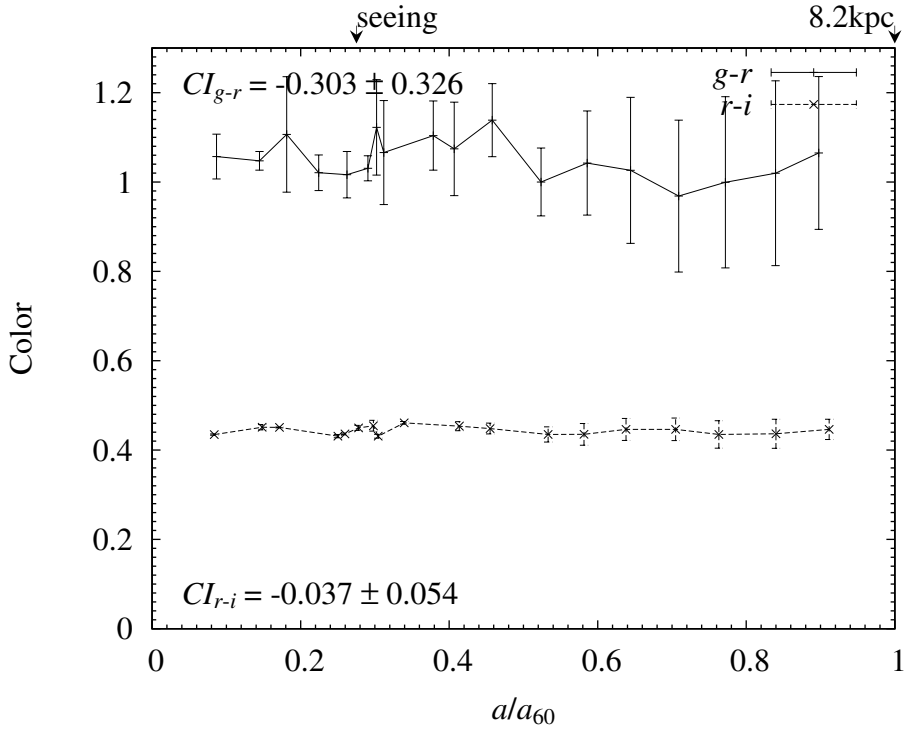

Figure 35: No.20 E+A galaxies

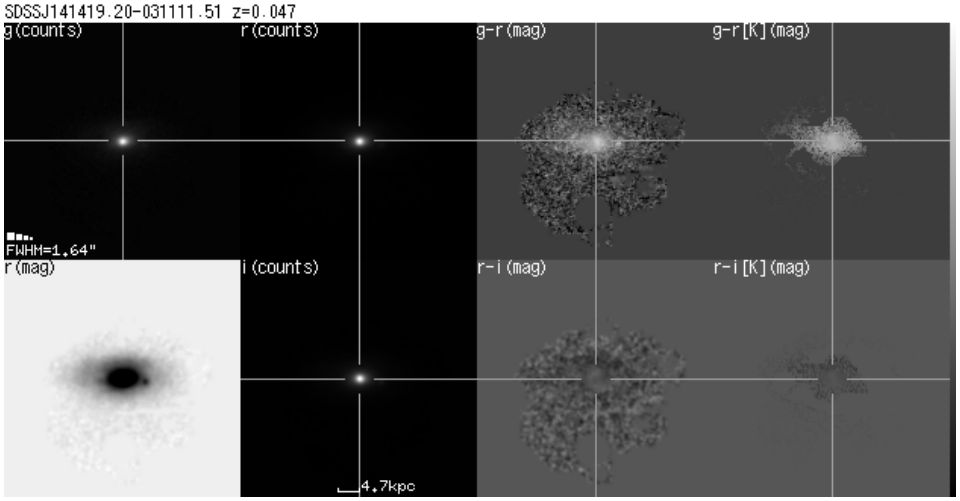

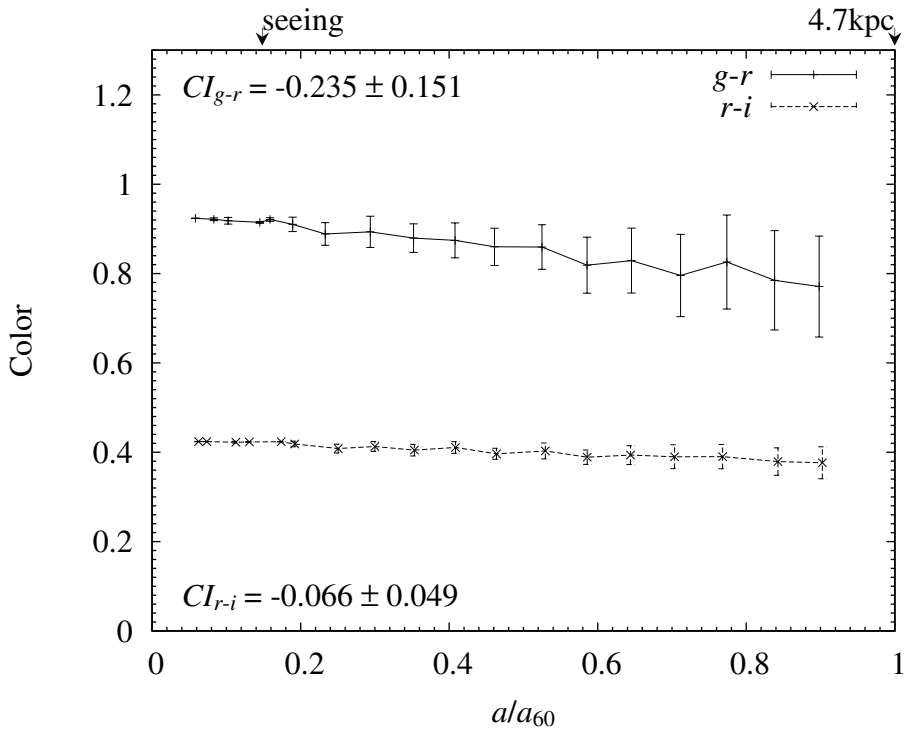

Figure 35: No.21 E+A galaxies

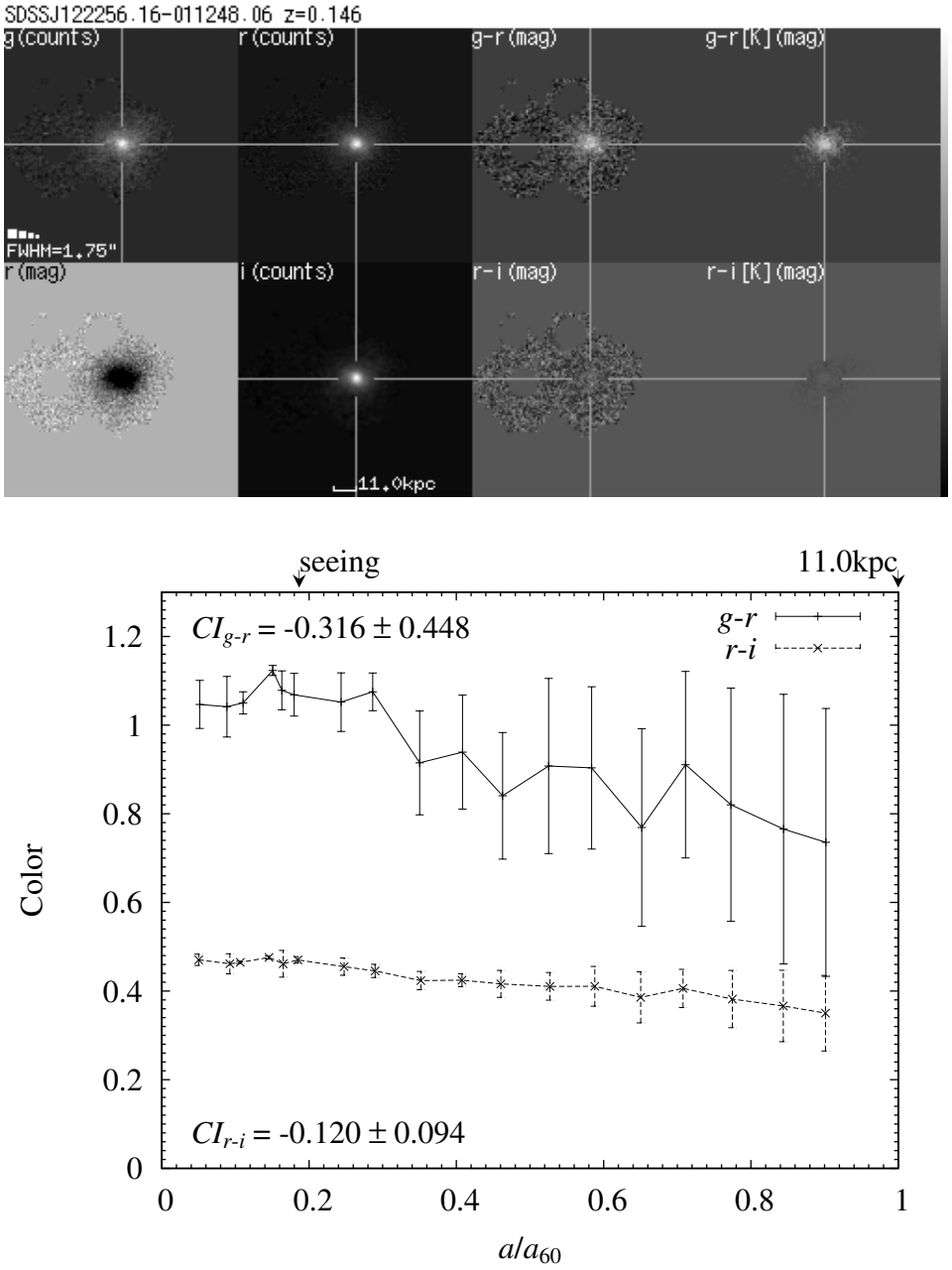

Figure 35: No.22 E+A galaxies

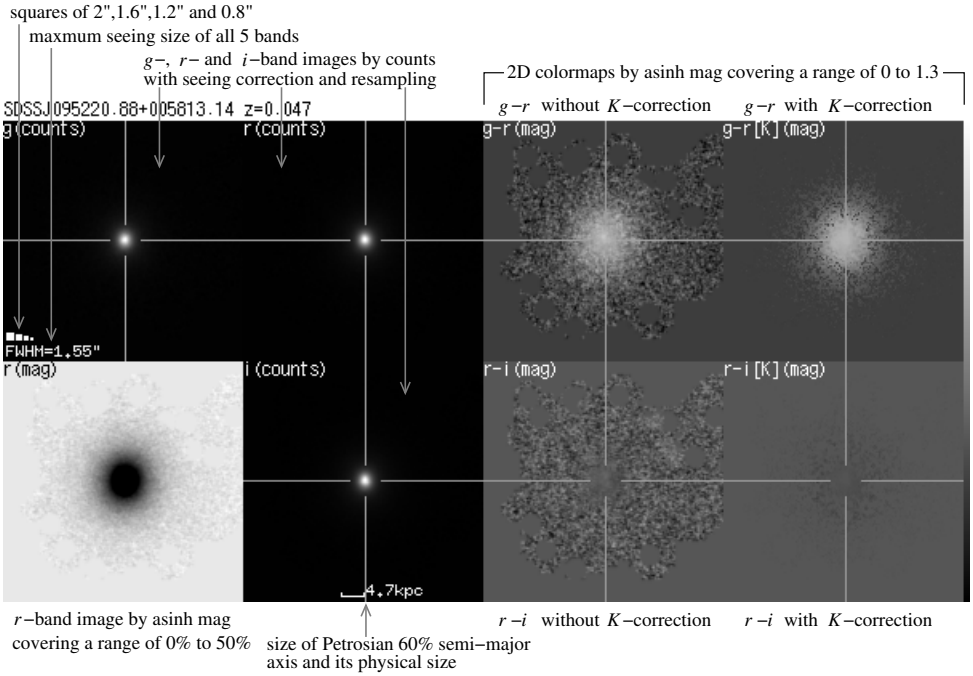

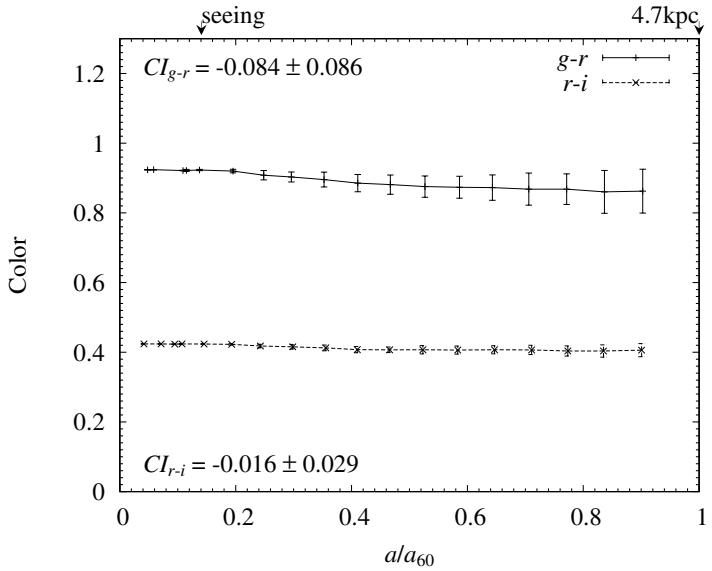

Figure 36: Example of g-, r- and i-band image, $g-r$ and $r-i$ 2D colormaps (*top*) and the rest color profiles (*bottom*) of a normal early-type galaxy. 2D colormaps are based on asinh magnitude, but Pogson magnitude is used for color profiles. The K-corrected 2D colormaps are on the right, another is not applied K-correction. The details of explanation of top panel are inlaid in it. The 2D colormaps of elliptical galaxy are featureless, and many of them have moderate negative slope (redder gradients toward the center) at $g-r$ and quite flat $r-i$ color gradient.

3.4.2 2D Color Properties–Radial Color Gradient and Color Morphologies

An example of $g-r$ and $r-i$ 2D colormaps and its radial color profile of normal early-type galaxy are presented in Figure 36. The 3 positive images of left side on the top panel show g-, r- and i-band images by counts with seeing correction and resampling, and 4 images of right side are $g-r$ and $r-i$ 2D colormaps in asinh magnitude. Two rightmost panels of 2D colormaps are pixel-to-pixel K-corrected, the others are not. The seeing size of all images are indicated in the g-band image, along with squares of $2''$, $1.6''$, $1.2''$ and $0.8''$ for scale. The bottom panel is $g-r$ and $r-i$ radial color profiles using Pogson magnitude, and seeing size(FWHM/2) and physical scale of a_{60} are displayed on the upper abscissa. In this Figure, we inlay the details of explanation of images and 2D colormap, and the same form is used in Figure 35, where we present all of our E+A galaxies.

The 2D colormaps of elliptical galaxies are basically featureless, and major difference between K-corrected and uncorrected is small. The radial color profiles derived from 2D rest color information also show moderate properties. Many of elliptical galaxies have quite flat $r-i$ color gradient and moderate negative slope at $g-r$. Although there are many kinds of $g-r$ radial gradients in early-type galaxies, the positive slope (bluer gradients toward the center) at $g-r$ profile is seldom seen.

Meanwhile, many our E+A galaxies show mysterious 2D colormaps and radial profiles. We present 2D colormaps and radial profiles of our all E+A galaxies in Figure 35. The images and color profiles in Figure 35 are placed in ascending order with respect to 4000Å break(D_{4000}), and we numbered our E+A galaxies by this order. The slopes of $g-r$ radial profile of a number of E+A galaxies are positive (bluer gradients toward the center) which is seldom seen in normal early-type galaxies. We show the list of our 22 E+A galaxies in table 3 with results of $CI_{g\text{-}r}$ and $CI_{r\text{-}i}$. It turns out that $\sim$63% of our E+A galaxies have a positive slope of radial $g-r$ color gradient. In the case of $r-i$ color gradient, $\sim$77% of E+As have a positive slope. In addition, some E+A galaxies show irregular pattern in their $g-r$ and $r-i$ 2D colormap without K-correction — 'Color Morphology' — asymmetrical and clumpy bluer region. The No.1, No.2 and No.3 E+A galaxies are especially conspicuous, the bluer regions are shown near galaxy center, but some bluest regions are slightly placed away from nucleus. However, the K-corrected 2D colormap tend to weaken this asymmetrical feature. We expect that such a region has a particular SED, and this may be a limit of K-correction by fitting template

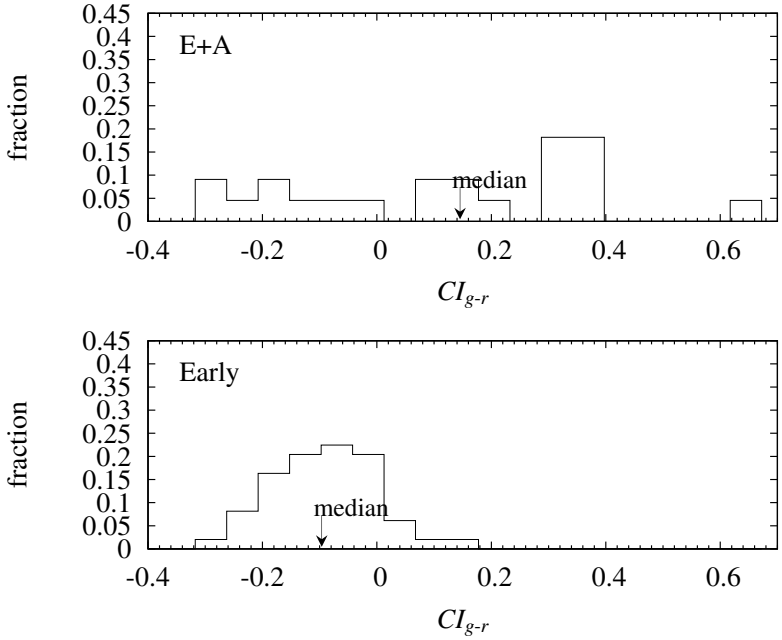

Figure 37: The histograms of $g-r$ radial color gradient, showing E+A (*top*) and early-type (*bottom*) galaxies.

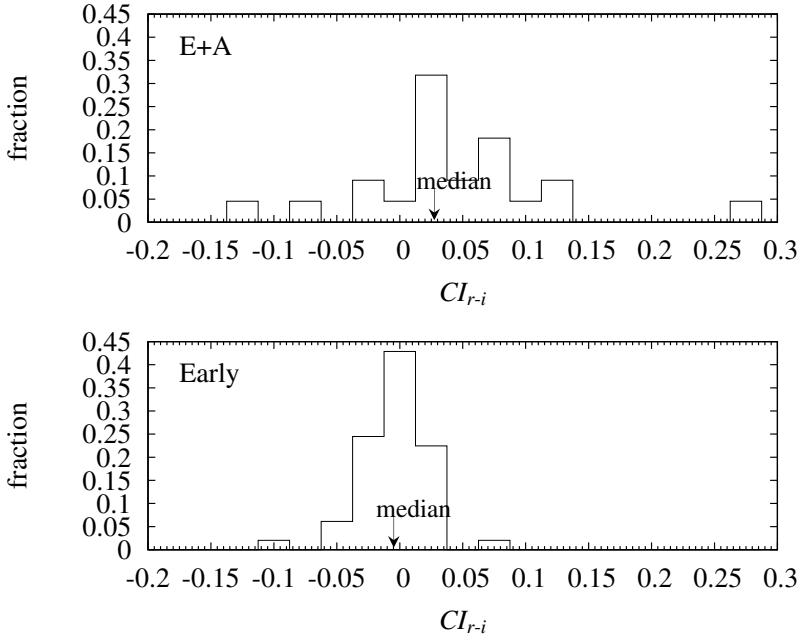

Figure 38: The histograms of $r-i$ radial color gradient, showing E+A (*top*) and early-type (*bottom*) galaxies.

SEDs. This 'irregularities' on 2D colormaps are observed in E+A galaxies with 'positive slope'. But all E+A galaxies with positive slope does not necessarily have conspicuous irregularities on 2D colormap. That is, the E+A galaxies with 'positive slope' of radial color gradient tend to show irregular pattern on 2D colormap.

To compare the radial color gradients of the E+A galaxies with that of normal early-type galaxies, the distributions of radial color gradients $CI_{g\text{-}r}$ and $CI_{r\text{-}i}$ are displayed in Figure 37 and Figure 38. It is clear that normal early-type galaxies have negative $g-r$ color gradients, and almost all are placed within $-0.2 < CI_{g\text{-}r} < 0$, and $r-i$ color gradients are concentrated at $CI_{r\text{-}i} \sim 0$. Each median is -0.10 and 0.005, respectively. On the other hand, $CI_{g\text{-}r}$ and $CI_{r\text{-}i}$ of E+A galaxies are dispersed, and galaxies with large positive slope are obviously increased. Each median is also shifted to positive, 0.14 and 0.03, respectively. We then applied a Kolomogorov-Smirnov (K-S) two-sample test to find the probability that the two samples are drawn from the same parent distribution. The results show that $g-r$ and $r-i$ color gradient distributions of E+A are different from that of early-type galaxies with a more than 99.99% significance level.

3.4.3 Comparison between Radial Color Gradient and Other Photometric/Spectroscopic Properties

We showed that E+A galaxies have interesting radial color gradients. Comparison between radial color gradient and other photometric/spectroscopic properties may find a clue to E+A evolution scenario.

Figures 39 and 40 show the relation between radial color gradients CI and rest $g-r$ or $r-i$ colors. Observed colors in this study are shifted to the restframe using the K-correction software (`v3_2`) by Blanton et al. (2003). Our 22 E+A and 49 early-type galaxies are plotted using asterisks and open lozenges, respectively. The error bars of the top right indicate a typical error. The coefficient P of the bottom left is the Spearman linear correlation coefficient, and the solid line represents a linear least-squares fit using E+A's data points. A data point with open circle is No.1 of E+A galaxy rejected for P and linear least-squares fit, since the errors of $CI_{g\text{-}r}$ and $CI_{r\text{-}i}$ are too large (0.67 and 0.20, respectively). We expect that No.1 of E+A galaxy has too heavy disturbance feature to calculate appropriate Petrosian radius. We can find obvious correlations of $P \sim -0.7$ level between radial colors gradients and colors. On the other hand, the early-type galaxies shows only $P \sim -0.32$ at the maximum absolute value in these diagrams. The results also support that the photometric properties of E+A are different from that of early-type galaxies

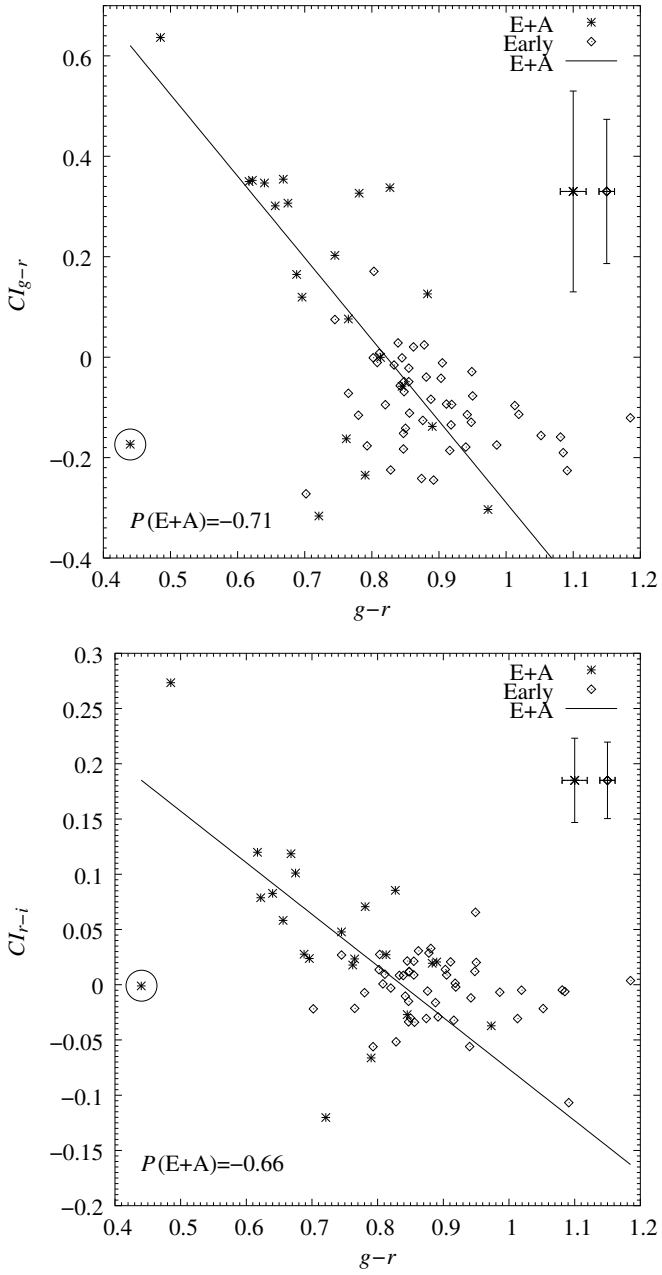

Figure 39: The $g-r$ radial color gradient plotted against $g-r$ rest color (*top*) and $r-i$ radial color gradient plotted against $g-r$ rest color (*bottom*), showing 22 E+A and 49 early-type galaxies. E+A and early-type galaxies are plotted using asterisks and open lozenges, respectively. The coefficient P of the bottom left is the Spearman linear correlation coefficient, and the solid line represents a linear least-squares fit using E+A's data points. A circled asterisk is No.1 E+A galaxy rejected for P and linear least-squares fit. Error bars of the top right are typical errors of the observational data.

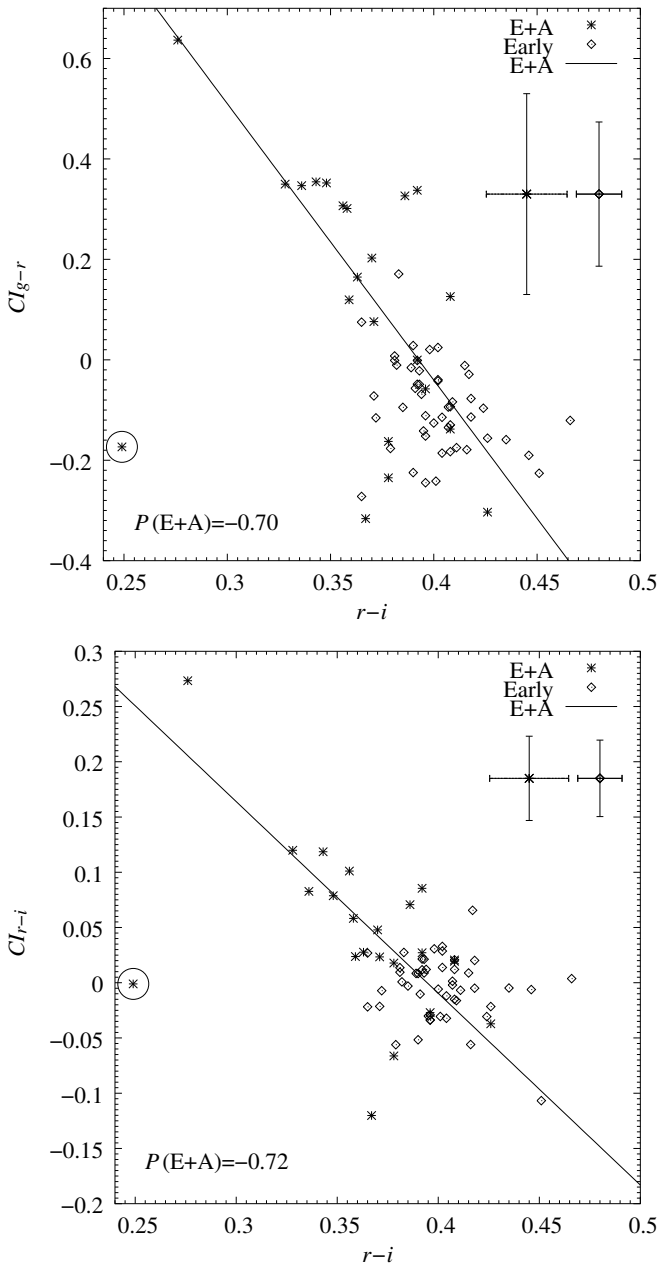

Figure 40: The $g-r$ radial color gradient plotted against $r-i$ rest color (*top*) and $r-i$ radial color gradient plotted against $r-i$ rest color (*bottom*), showing 22 E+A and 49 early-type galaxies. E+A and early-type galaxies are plotted using asterisks and open lozenges, respectively. The coefficient P of the bottom left is the Spearman linear correlation coefficient, and the solid line represents a linear least-squares fit using E+A's data points. A circled asterisk is No.1 E+A galaxy rejected for P and linear least-squares fit. Error bars of the top right are typical errors of the observational data.

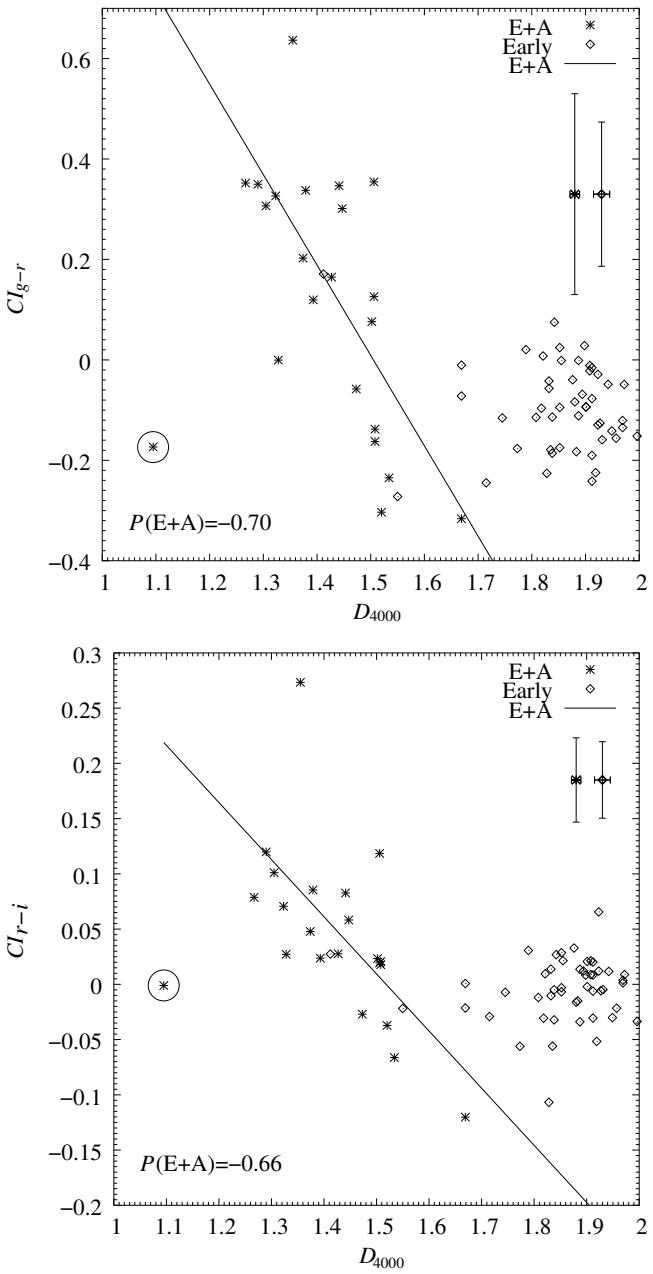

Figure 41: The $g-r$ radial color gradient plotted against D_{4000} (*top*) and $r-i$ radial color gradient plotted against D_{4000} (*bottom*), showing 22 E+A and 49 early-type galaxies. E+A and early-type galaxies are plotted using asterisks and open lozenges, respectively. The coefficient P of the bottom left is the Spearman linear correlation coefficient, and the solid line represents a linear least-squares fit using E+A's data points. A circled asterisk is No.1 E+A galaxy rejected for P and linear least-squares fit. Error bars of the top right are typical errors of the observational data.

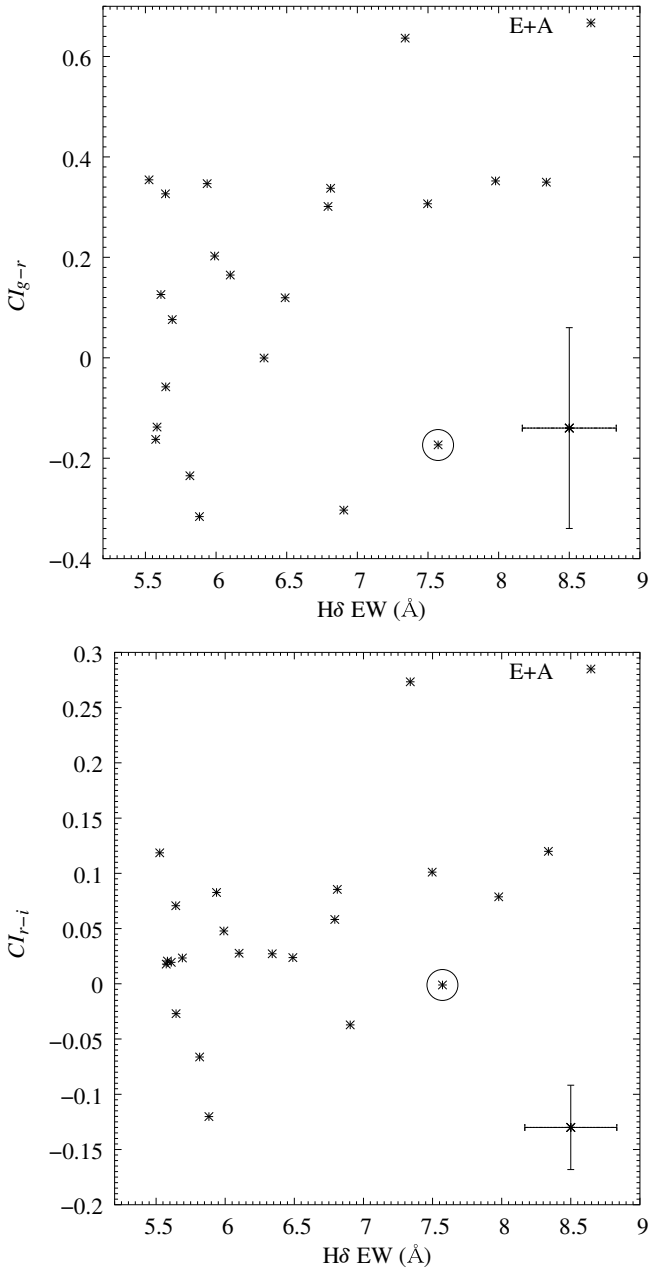

Figure 42: The $g-r$ radial color gradient plotted against Hδ EWs (*top*) and $r-i$ radial color gradient plotted against Hδ EWs (*bottom*), showing 22 E+A galaxies. A circled asterisk is No.1 E+A galaxy. Error bars of the bottom right are typical errors of the observational data.

significantly.

Next, we compare the radial color gradients with spectroscopic properties. In Figure 41, we plot radial color gradient against the 4000Å break (D_{4000}) which is sensitive to old stellar populations. Symbols and rejections are the same as previous figures. This diagram evidently indicate the correlation between radial color gradients and 4000Å break. Early-type galaxies shows less than $|P| \sim 0.2$ level correlations like that of color gradients and colors. But normal early-type galaxies are not placed under the regression line, different from plots of color gradients against colors. It is shown that D_{4000} separates the two populations more clearly than the broad-band colors.

To examine the relation between radial color gradients and amount of young A-type stars, we plot radial color gradients against Hδ EW in Figure 42. Symbols are the same as previous figures. Compared with the case of D_{4000}, we cannot find tight correlation. But, these panels show a trend that E+A galaxies with large positive slope of radial color gradient tend to show strong Hδ EWs. However, this result might be affected by the cut-off of $a/a_{60} < 0.35$ for measuring radial color gradient, since some E+A galaxies with positive slope gradient show the profile which exhibits the bluest color at near the galaxy center.

3.4.4 Evolution Scenario for E+A Radial Color Gradients

In this subsection, we compare SED models and observational quantities to find out evolution scenario for E+A radial color gradients. Using the GISSEL model by Bruzual & Charlot (2003), we simulated three representative star formation histories following Goto (2003): (i) *Burst* model, which has an instantaneous starburst (with duration of 1 Gyr) at the beginning and no star formation thereafter. (ii) *Constant* star formation. (iii) *Exponentially* decaying star formation (with $\tau = 1$ Gyr). In all the three models, we use the Salpeter initial mass function (Salpeter 1955). Figure 43 plots Hδ EWs against time (or galaxy age) for the three models. The dot-dashed, solid and dotted lines show the models with instantaneous burst, constant star formation and exponentially decaying star formation rate. The burst model has a strong Hδ EW right after its truncation at 1 Gyr. However, its Hδ EW declines rapidly, and becomes less than 3Å at 1 Gyr after the truncation. The exponentially decaying model maintains strong Hδ for a longer time. Its Hδ EW becomes 3Å in 5 Gyrs. The constantly star-forming model maintains a large Hδ EW (>6Å) beyond 13 Gyr. Although shown here for a comparison purpose, we omit the constantly star-forming model from our main discussion, since our E+A galaxies are selected

to have no on-going star formation activity.

We compare the models and the data on the Hδ EW v.s. D_{4000} plane in Figure 44. A caveat, however, is that models become less accurate on the plane since both Hδ EW and D_{4000} are more difficult quantities to reproduce than broad band colors. For models, we use Hδ EWs given in the GISSEL model, which were measured using the flux between 4083.50 and 4122.25Å. This is essentially the same window as used to measure Hδ EWs from the observational data between 4082 to 4122Å. For D_{4000}, the SED model uses the flux ratio of the 3750-3950Å window to the 4050-

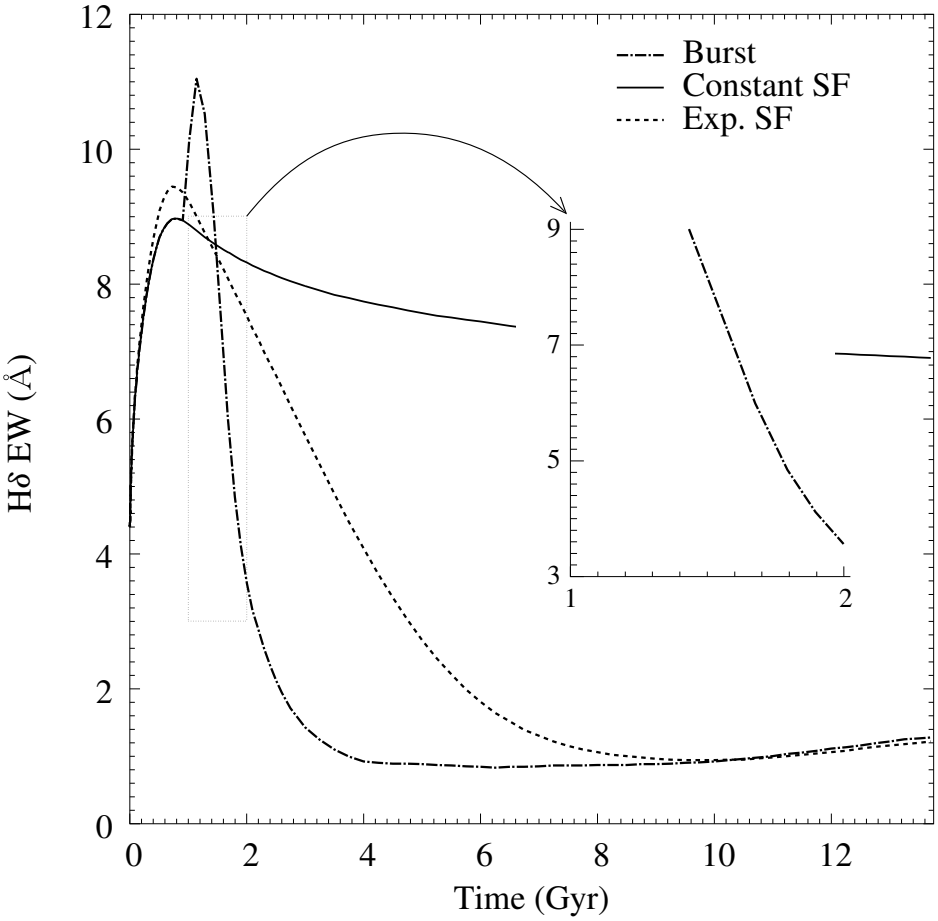

Figure 43: Hδ EWs are plotted against time (age) for three star formation histories with the GISSEL model. The dot-dashed, solid and dotted lines show the models with instantaneous burst, constant star formation and exponentially decaying star formation rate. The models in this figure assume Salpeter IMF and solar metallicity. The inlaid panel is enlarged plot of burst model with $3 <$ Hδ EW < 9. Numerical result of each model is provided by Goto (2003).

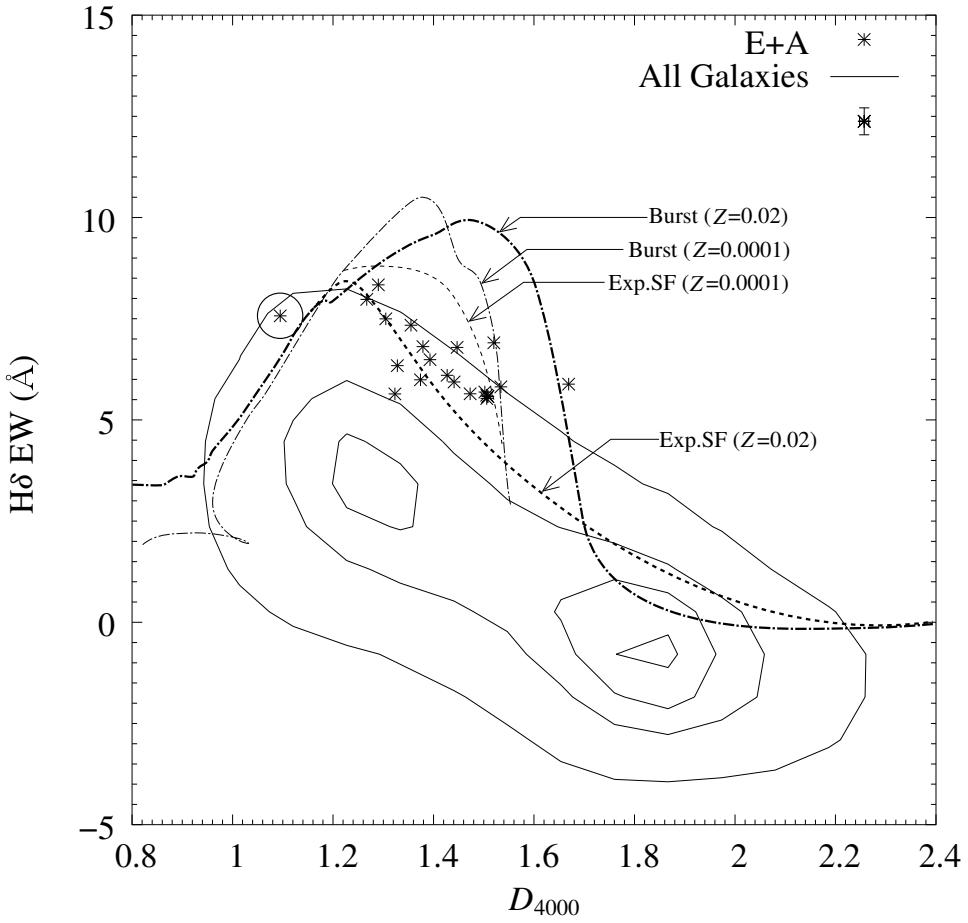

Figure 44: Hδ EWs are plotted against D_{4000} for the models with $Z = 0.0001$(0.5% solar) and $Z = 0.02$(solar). Star formation histories are the burst and exponentially decreasing, shown by the dot-dashed and dotted, respectively. Observational data are plotted using asterisks. A circled asterisk is No.1 E+A galaxy. Error bars of the top right are typical errors of the observational data. The contours show the distribution of all DR1 94770 galaxies in Goto (2003).

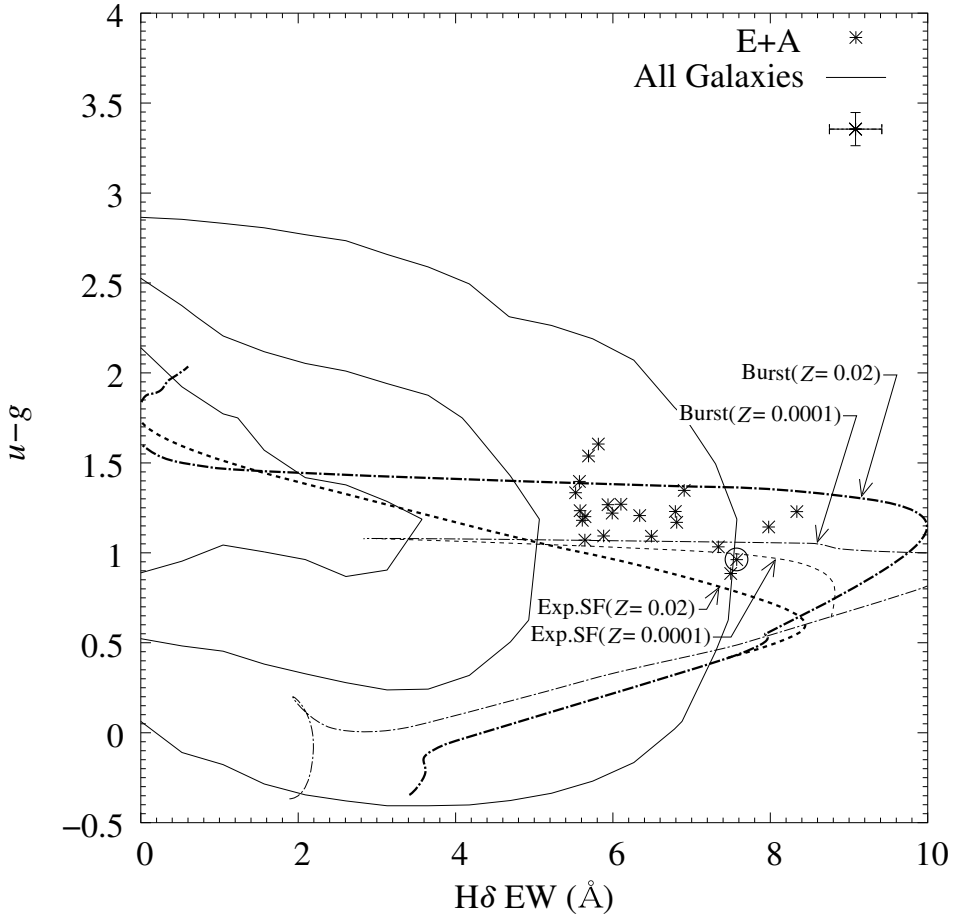

Figure 45: The $u-g$ color is plotted against Hδ EWs for the models with $Z = 0.0001$(0.5% solar) and $Z = 0.02$(solar). The dot-dashed and dotted lines are for the models with instantaneous burst and exponentially decaying star formation rate. Observational data are plotted using asterisks. A circled asterisk is No.1 E+A galaxy. Error bars of the top right are typical errors of the observational data. The contours show the distribution of all DR1 94770 galaxies in Goto (2003).

5250Å window (Bruzual 1983). Observationally D_{4000} is measured using the ratio of the flux in the 3751-3951Å window to that in the 4051-4251Å (Stoughton et al. 2002). We regard these two D_{4000} measurements as essentially the same.

In Figure 44, the dot-dashed and dotted lines are for the models with the instantaneous burst and the exponentially decaying star formation rate. We subtracted 1Å from the model Hδ EWs to compensate for possible stellar absorption. Different line width are for two different metallicities (Z = 0.001 and 0.02). The models might have a slight shift toward larger D_{4000} and Hδ directions, compared with the distribution of all the observed galaxies. However, the behavior of the models on this plane well reproduce expected behavior of galaxies, in the sense that star-forming galaxies evolve into large D_{4000} and small Hδ EWs. Therefore, we regard that qualitative interpretation based on the models is valid. Observed data of E+A galaxies are plotted using asterisks, and we find that our E+A galaxies are located under a single evolution track for the most part. But it is uncertain whether these E+A galaxies run along the track of instantaneous burst or not, since models might have a slight shift.

It is more difficult to reproduce emission lines with the current version of the model, therefore, the $u-g$ color is preferable for examination of on-going star formation since it shows better agreement between the SED models and the observation data. In Figure 45, we plot $u-g$ against Hδ EW for the two models and the observational data. Symbols are the same as previous figures. The model $u-g$ color depends on metallicity to some extent, showing bluer $u-g$ color with decreasing metallicity. Our E+A galaxies are distributed between the instantaneous burst model with Z = 0.001 and that with solar metallicity. Neither of the exponentially decaying models cannot explain the observed data. This indicates that E+A galaxies are in a post-starburst phase, and cannot be explained by more normal star formation histories.

If the burst model is assumed, our young E+A galaxies with Hδ EW $\sim$ 8Å are evolved into that with Hδ EW $\sim$ 5Å within $\sim$300 Myr by Figure 43. Our radial color gradient correlates with D_{4000} in Figure 41, and E+A galaxies with large positive slope of radial color gradient tend to show strong Hδ EWs (Figure 42). Our E+A galaxies are placed under a single track in D_{4000} - Hδ EW plane, therefore, we can interpret these results as some E+A's metamorphosis of large positive slope into flat or negative slope of radial color gradients within its time scale. Taken together, our observational results suggest that E+A galaxies have positive color gradients, large Hδ EW and small D_{4000} at the beginning, then evolve into negative color gradients,

small Hδ EW and large D_{4000}. It is revealing that a morphological quantity, color gradients, correlates well with the spectral properties such as Hδ EW and D_{4000}.

3.5 Discussion

Based on the SDSS broad-band imaging, we investigated spatial properties such as morphologies, 2D color properties and radial color gradients of the E+A galaxies. In this section, we discuss the relevance of our results to other E+A-related studies and physical implications.

The concentration index, C_e, of our E+A galaxies were distributed like early-type galaxies, and our visual inspection of the SDSS images also showed that our E+A galaxies are predominantly early-type galaxies. We can interpret these results as a suggestion that all of our E+A galaxies are bulge-dominated systems. Although E+As with disk-like morphologies have sometimes found in the previous observations (Couch et al. 1994, 1998; Dressler et al. 1994, 1999; Oemler, Dressler & Butcher 1997; Smail et al. 1997; Chang et al. 2001), it is not surprising if previous samples were contaminated by Hα-emitting galaxies. Perhaps since we selected 22 E+A galaxies with strict spectroscopic criteria, 'without Hα nor [OII] emission', our 22 E+A galaxies are all bulge-dominated. Our results are also consistent with those by Quintero (2004) and Blake et al. (2004).

These findings have important implications to the physical origin of E+A galaxies when compared with theoretical simulations. It has been long known that an elliptical galaxy can be a final product of major merging (e.g., Barnes & Hernquist 1992), quite possibly accompanied by a tidal tail feature in its early stage. In a more detailed major merger model, Bekki (1998) showed that ancestral equal-mass galaxies are completely destroyed so as to form a spheroid that looks more like an elliptical galaxy, and merging of two unequal-mass spirals are finally transformed into one S0 galaxy that has a flattened oblate spheroid. We noticed that at least half of our E+A galaxies show tidal feature or disturbed morphologies. Thus not only disturbed morphologies but also E/S0 morphologies of our unalloyed E+A sample indicates possibilities of merger origin of E+A galaxies, and we can expedite following discussion smoothly.

We found irregular 'Color Morphologies' – asymmetrical and clumpy pattern – at the center of $g-r$ and $r-i$ 2D colormap of E+A galaxies without K-correction. The HST observations of five bluest E+A galaxies with $z \sim 0.1$ by Yang et al. (2004) show the presence of asymmetric components in the residual images obtained by

subtraction the smooth and symmetric model images form the data. The physical scale of the asymmetric components of the HST observation is comparable to that of our asymmetrical/clumpy pattern in the 2D colormap. We expect that these irregularities of residual images and our 2D colormap are basically the same origin, and one possible interpretation is that they are fluctuations created during the merger/interaction event, which also caused the central post-starburst phase.

Our results showed that more than half of our E+A galaxies exhibit the positive radial $g-r$ and $r-i$ color gradients. The $g-r$ and $r-i$ colors represent roughly age and metallicity gradient, respectively. The results of $g-r$ radial color gradients are good agreement with a long-slit spectroscopic observation of 21 E+A galaxies by Norton et al. (2001) who found young stellar populations of E+A galaxies are more centrally concentrated than the older populations. Although Bartholomew, Rose & Gaba (2001) reported that K+A galaxies on average tend to have slightly bluer radial gradients toward the center than the normal early-type galaxies, these K+A galaxies are detected in rich clusters and their spectroscopic criteria (Hδ EW < 3 and $-5 <$ [OII] EW) is less strict than ours. It is perhaps difficult to compare our E+A galaxies with that selected with the different criteria in different environment, however, we can find the same tendency that substantial number of E+A galaxies have a positive slope of radial color gradient and that our strict spectroscopic criteria produce clearer results of a K-S test (more than 99.99% significance level). Theoretically, models of interacting gas-rich spirals suggest that the most common result of such tidal perturbations is indeed to drive a large fraction of interstellar material close to the center of each galaxy; the shocked gas robbed its angular momentum flows inward (Barnes & Hernquist 1992). Recent numerical simulations show that rapid collapse of gas drives a starburst at the center of the merging system (e.g., Mihos & Heanquist 1996). Especially, Mihos & Heanquist (1994) numerically simulated galaxy merger and predicted color gradients in such systems. In their Fig.7, they show that the color gradient of merger remnants changes the slope of color gradient from positive to negative during 1-5 Gyr after the burst in a qualitatively similar way as our Fig.35. The agreement adds more credibility in the merger/interaction origin of E+A galaxies, and further justifies our interpretation of change of the slope as an evolutionary sequence. In summary, our findings of positive $g-r$ radial color gradients of E+A galaxies are consistent with the merger origin of E+A galaxies.

We found the tight correlation between radial color gradients and 4000Å break. We also found that E+A galaxies follow a single evolution track in D_{4000} - Hδ EW plane (in Figure 44). Taken all together, these results can be interpreted in an

evolutionary sequence where E+A galaxies change their slope from positive to negative, and they also change irregular into moderate of 2D colormap during the time scale of ∼300 Myr. It is revealing that E+A galaxies show morphological metamorphosis (change in color gradients and 2D colormap) synchronously as their stellar population ages as indicated by D_{4000} and Hδ EW. This may be the general picture how E+A galaxies evolve after the truncation of starburst caused possibly by the merger/interaction. It is a concern that our radial color gradients do not show a tight correlation with Hδ EW, but the tendency that E+A galaxies with large positive slope of radial color gradient show strong Hδ EWs. However, this may be affected by our cut-off of inner region ($a/a_{60} < 0.35$) to avoid seeing effects when measuring radial color gradients. Observation with high-resolution imaging might remove this effects, and produce a more accurate picture.

Although we also found the tight correlation between radial color gradients and colors, the data points of E+A galaxies with redder color in the *CI*-Color plane overlap with that of normal early-type galaxies. We eliminated E+A candidates with Hδ EW less than 5.5Å for our analysis. Nevertheless, $g-r$ and $r-i$ color information have such a degeneracy. This means that it may be difficult to elucidate E+A's evolution phase with Hδ EW < 5.5 using only these color information.

Table 3: The list of E+A galaxies. The numbers are labeled in ascending order with respect to D_{4000}. The digits in Name represent R.A. and Dec., for example, R.A. and Dec. of Name SDSSJ010617.76+140354.00(No.16) are 01:06:17.76 and +14:03:54.00, respectively. The unit of a_{60} and line EWs are arcsec and Å, respectively. The morphological type $T = 0, 1, 2, 3, 4, 5, 6$ and -1 represent E,S0,Sa,Sb,Sc,Sdm,Im and unclassified, respectively.

No.	Name	z	M_r	$u-g$	$g-r$	$r-i$	a_{60}	D_{4000}	Hδ EW	Hα EW	[OII] EW	C_e	T	CI_{g-r}	CI_{r-i}
16	SDSSJ010617.76+140354.00	0.038	-19.76	1.33	0.67	0.34	2.96	1.51	5.53±0.32	2.10±0.08	-0.13±-0.02	0.28	1	0.35±0.09	0.12±0.05
7	SDSSJ035652.44-061031.22	0.037	-19.85	1.03	0.48	0.28	3.43	1.35	7.34±0.41	2.39±0.10	-0.46±-0.05	0.32	0	0.64±0.21	0.27±0.09
18	SDSSJ083415.60+375157.24	0.168	-23.10	1.23	0.89	0.41	4.93	1.51	5.58±0.23	0.74±0.02	-0.22±-0.03	0.32	-1	-0.14±0.34	0.02±0.05
3	SDSSJ084918.96+462252.68	0.041	-20.88	1.23	0.62	0.33	3.00	1.29	8.34±0.27	1.91±0.05	-1.17±-0.08	0.31	1	0.35±0.11	0.12±0.03
19	SDSSJ093842.96+000148.68	0.091	-21.84	1.40	0.76	0.38	4.07	1.51	5.57±0.47	1.15±0.04	-1.62±-0.21	0.36	-1	-0.16±0.19	0.02±0.05
12	SDSSJ100743.68+554934.68	0.045	-20.88	1.27	0.64	0.34	3.44	1.44	5.94±0.32	1.57±0.05	-2.06±-0.20	0.28	1	0.35±0.12	0.08±0.03
6	SDSSJ111050.88+005530.98	0.152	-22.22	1.21	0.81	0.39	3.34	1.33	6.34±0.32	1.28±0.05	-0.94±-0.13	0.33	1	-0.00±0.18	0.03±0.04
4	SDSSJ111108.16+000408.66	0.184	-22.32	0.89	0.68	0.36	2.95	1.30	7.50±0.47	1.60±0.08	-0.57±-0.08	0.36	1	0.31±0.53	0.10±0.06
11	SDSSJ115837.68-021710.97	0.088	-22.11	1.27	0.69	0.36	3.35	1.43	6.10±0.28	1.75±0.07	0.69±0.09	0.34	-1	0.16±0.09	0.03±0.01
2	SDSSJ120418.96-001855.84	0.094	-22.74	1.14	0.62	0.35	4.10	1.27	7.98±0.27	2.11±0.06	-1.18±-0.07	0.31	-1	0.35±0.14	0.08±0.03
13	SDSSJ120523.28+643029.52	0.082	-22.78	1.23	0.66	0.36	4.64	1.45	6.79±0.29	1.78±0.05	0.91±0.09	0.31	-1	0.30±0.16	0.06±0.03
22	SDSSJ122256.16-011248.06	0.146	-21.74	1.09	0.72	0.37	4.69	1.67	5.88±1.42	1.19±0.05	0.61±0.40	0.45	2	-0.32±0.45	-0.12±0.09
20	SDSSJ132315.60+630726.40	0.175	-21.94	1.35	0.97	0.43	3.00	1.52	6.90±0.93	1.11±0.07	1.56±0.36	0.35	1	-0.30±0.33	-0.04±0.05
17	SDSSJ133350.64-001617.71	0.176	-22.35	1.18	0.88	0.41	2.94	1.51	5.61±0.49	2.21±0.14	0.71±0.15	0.31	1	0.13±0.27	0.02±0.04
9	SDSSJ140801.68+514225.92	0.160	-22.34	1.17	0.83	0.39	2.88	1.38	6.81±0.37	-0.12±-0.00	0.51±0.07	0.33	1	0.34±0.23	0.09±0.03
5	SDSSJ141003.60+603229.76	0.171	-22.76	1.07	0.78	0.39	2.83	1.32	5.64±0.25	0.67±0.05	-1.08±-0.07	0.31	-1	0.33±0.21	0.07±0.03
21	SDSSJ141419.20-031111.51	0.047	-21.37	1.60	0.79	0.38	5.53	1.53	5.81±0.34	0.33±0.01	-1.11±-0.18	0.34	-1	-0.24±0.15	-0.07±0.05
1	SDSSJ161330.24+510335.64	0.034	-20.06	0.96	0.44	0.25	9.98	1.09	7.57±0.29	0.54±0.02	1.10±0.21	0.36	-1	-0.17±0.67	-0.00±0.20
15	SDSSJ162702.64+432833.96	0.046	-21.75	1.54	0.77	0.37	5.38	1.50	5.69±0.22	0.67±0.01	-1.41±-0.12	0.32	-1	0.08±0.12	0.02±0.03
10	SDSSJ164608.16+363705.16	0.137	-22.45	1.09	0.70	0.36	4.15	1.39	6.49±0.46	1.12±0.03	-0.35±-0.04	0.35	-1	0.12±0.24	0.02±0.04
8	SDSSJ170636.48+334720.40	0.124	-22.06	1.22	0.74	0.37	3.08	1.37	5.99±0.39	0.34±0.02	-0.84±-0.10	0.32	-1	0.20±0.23	0.05±0.04
14	SDSSJ211348.24-063059.65	0.159	-22.11	1.20	0.84	0.40	2.90	1.47	5.64±0.51	0.96±0.03	-2.32±-0.56	0.33	1	-0.06±0.18	-0.03±0.03

4 Conclusions and A Future Perspective

We have investigated morphologies, 2D color property and radial color gradients of *true* 22 E+A galaxies with 5.5Å $< H\delta$ EW $<$ 8.5Å using the SDSS DR2 imaging data, in order to reveal evolution of E+A galaxies in terms of internal galaxy structures. We present the summary of our results:

- Concentration index, C_e, and our visual inspection of the SDSS images suggested that our E+A galaxies are predominantly bulge-dominated systems, and at least half of our E+A galaxies exhibit a tidal feature or disturbed morphologies.

- We found irregular 'Color Morphologies' – asymmetrical and clumpy pattern – at the center of $g-r$ and $r-i$ 2D colormap of the E+A galaxies.

- We found that substantial number of E+A galaxies have a positive slope (bluer towards the center) of radial $g-r$ and $r-i$ color gradient.

- Kolomogorov-Smirnov two-sample tests showed that $g-r$ and $r-i$ color gradient distributions of E+A galaxies are different from that of early-type galaxies with more than 99.99% significance level.

- Our E+A sample showed tight correlation between radial color gradients and colors, and between radial color gradients and 4000Å break. We also found the tendency that E+A galaxies with large positive slope of radial color gradient show strong Hδ EWs.

- The comparison between the GISSEL model (Bruzual & Charlot 2003) and E+A's observational quantities, Hδ EW, D_{4000} and $u-g$ color, indicated that almost all our E+A galaxies are located under a single evolution track. Therefore, these results are interpreted that E+A's radial color gradient evolve from positive into negative slope, coherently with Hδ EW (8-5Å) within ∼300 Myr.

Our findings support that E+A galaxies are post-starburst galaxies caused by merger/interaction and underwent a centralized starburst, and make the two transitions, "from merger/interaction galaxy to E+A galaxy" and "from E+A galaxy to early-type galaxy", more plausible in one of the evolutionary paths. In addition, we presented a constraint on E+A's spatial evolution properties with a physical time scale. Detailed comparison with future theoretical simulations would advance our knowledge on the origin of E+A galaxies further.

Although we presented our results using an advantageous data set, the SDSS imaging and spectroscopic data, further work is needed to fully understand E+A's spatial evolution. A problems is the small number of E+A galaxies with a large apparent size. Needless to say, we intend to study using DR3 and following data releases, and expect results with stronger statistics and spatial evolution scenario. It is a critical point whether the evolution of radial color gradients of E+A galaxies is rapid or slow. If it is too rapid, we can hardly trace evolution of post-E+A phase using photometric information. If not, we might be able to trace it.

Higher-resolution photometric observations are also requited. If we observe our E+A galaxies with a higher resolution using an 8m-class telescope, we should be able to examine the details of morphological features and the fraction of E+A galaxies which leave traces of dynamically disturbed signs might increase. Structures like shells/ripple (Malin & Carter 1983) might be found in E+A galaxies which does not exhibit any disturbance in the SDSS imaging data.

Detailed spatial spectroscopic observations are also required. If photometric spatial evolution scenario of E+A galaxies is established, we might study more detailed evolution of kinematics but also evolution of metallicity gradient, using comparison to photometric properties. Note that previous spectroscopic study of E+A galaxies contains $\sim$50% of contamination.

As is mentioned in section 1.2, E+A evolution may be a part of E/S0 evolution scenario. Therefore, an exhaustive studies of spatial photometric properties of normal E/S0 galaxies is also required. That is, both top-down and bottom-up approaches are needed (We think that our study of E+A galaxies corresponds to top-down). In general, radial color gradient of elliptical galaxies have no correlation with other photometric/spectroscopic values in previous studies. However, the investigations using large and uniform sample like SDSS data set have not been undertaken. We may find some weak evolutional tendency by chance, and it may clue to solution of basic problems in global galaxy evolution scenario.

Theoretical approaches are also urgent necessity. Actually, it is difficut for us to find theoretical studies of spatial evolution of E+A or post-merger phase. Recent work related to such a spatial evolution which we can find is Kobayashi (2004) only.

5 Appendix

The spectrum of the example early-type galaxy in Figure 36 is displayed in Figure 46, which shows features of typical elliptical galaxy. In addition, we show spectra of all E+A galaxies used in this thesis in Figure 47. Each panel in the Figure 47 corresponds to that in Figure 35. The strong Hδ absorption line with no Hα and [OII] emission lines indicates that these galaxies have had strong star burst in recent 1 Gyr, but they do not have on-going star formation at all as shown in the lack of emission lines which indicate current star formation.

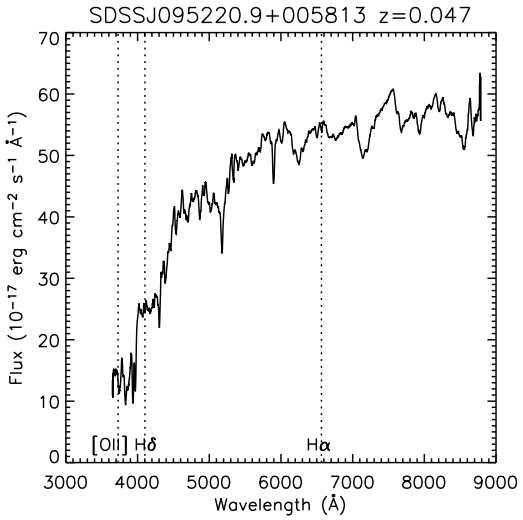

Figure 46: Example spectrum of a normal early-type galaxy in Figure 36. Spectrum is shifted to restframe and smoothed using a 20Å box.

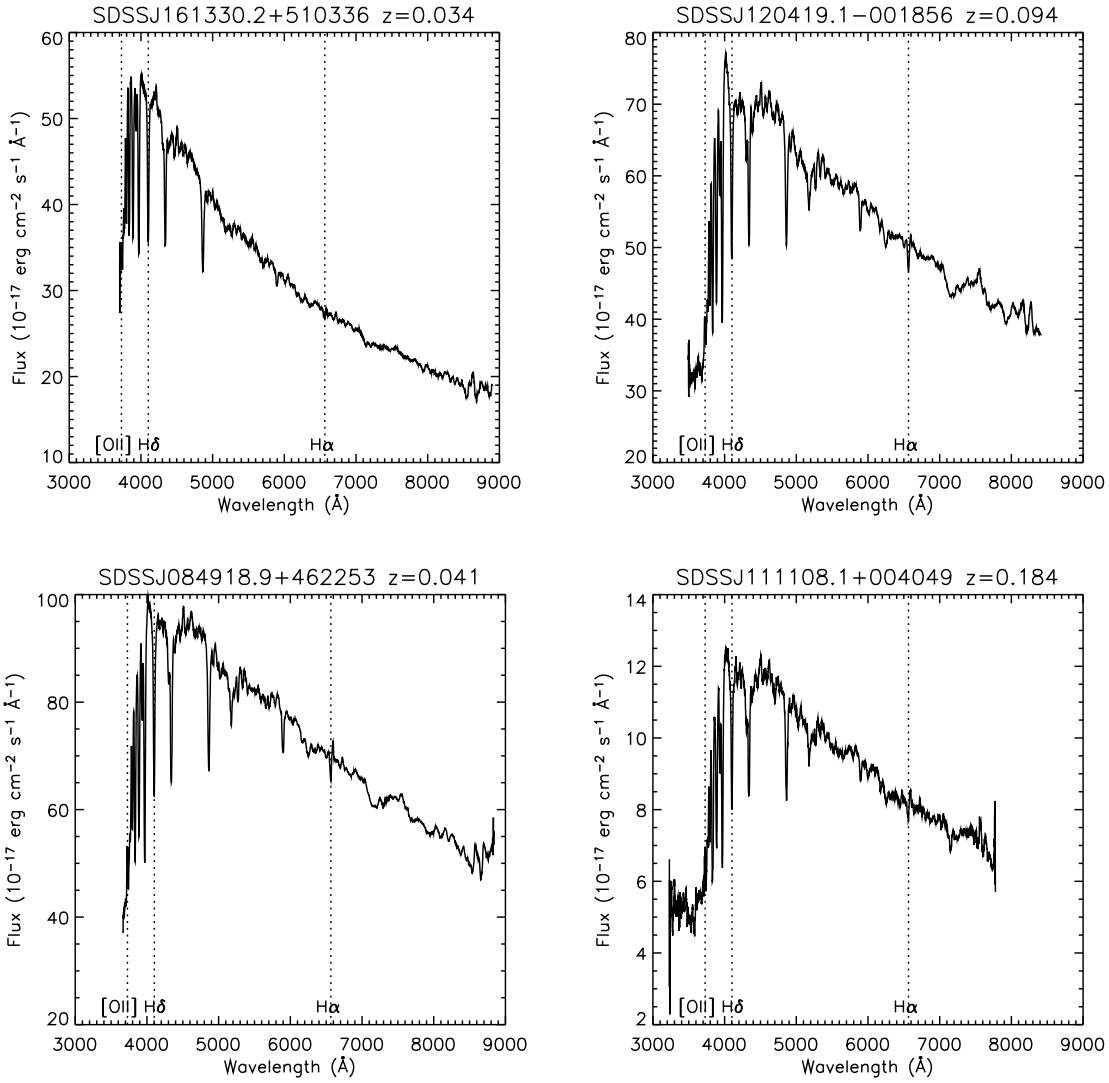

Figure 47: Spectra of our all E+A galaxies. The panels are placed in ascending order with respect to D_{4000}. We numbered our E+A galaxies by this order, so this Figure includes No.1(*top left*), No.2(*top right*), No.3(*bottom left*) and No.4(*bottom right*) E+A galaxies. Each panel in this figure corresponds to that in Figure 35. Spectra are shifted to restframe and smoothed using a 20Å box.

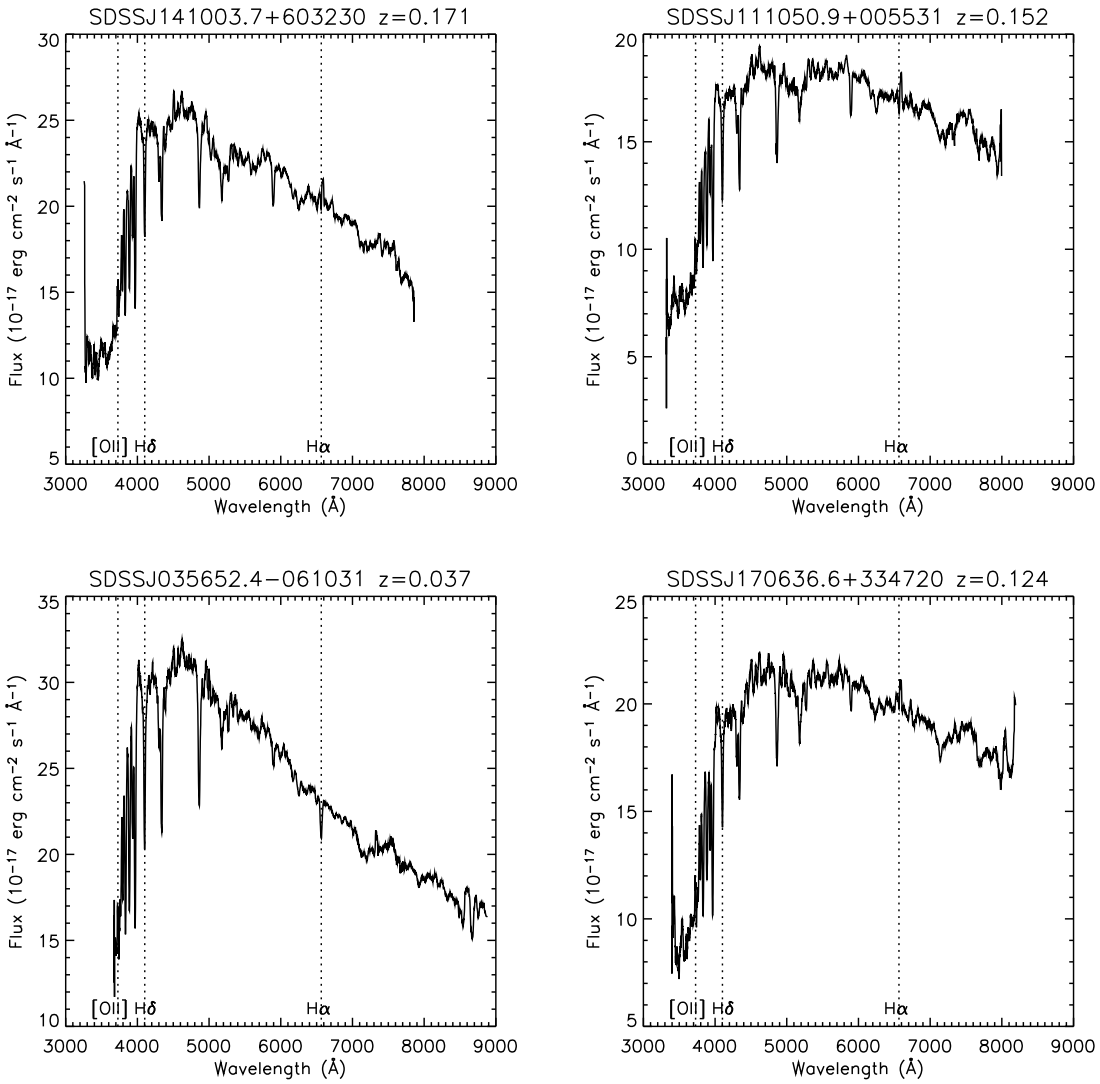

Figure 47: No.5, No.6, No.7 and No.8 E+A galaxies.

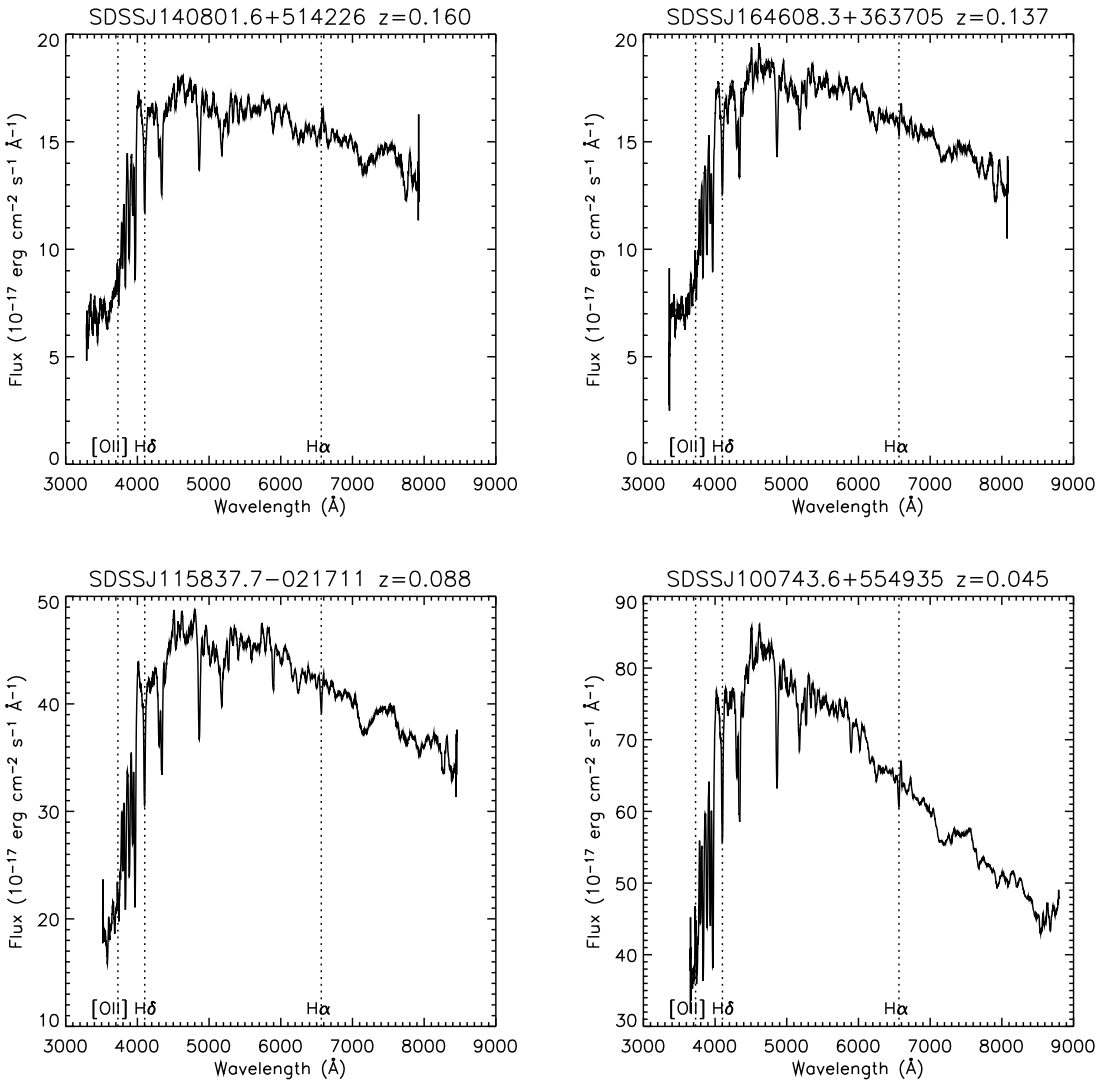

Figure 47: No.9, No.10, No.11 and No.12 E+A galaxies.

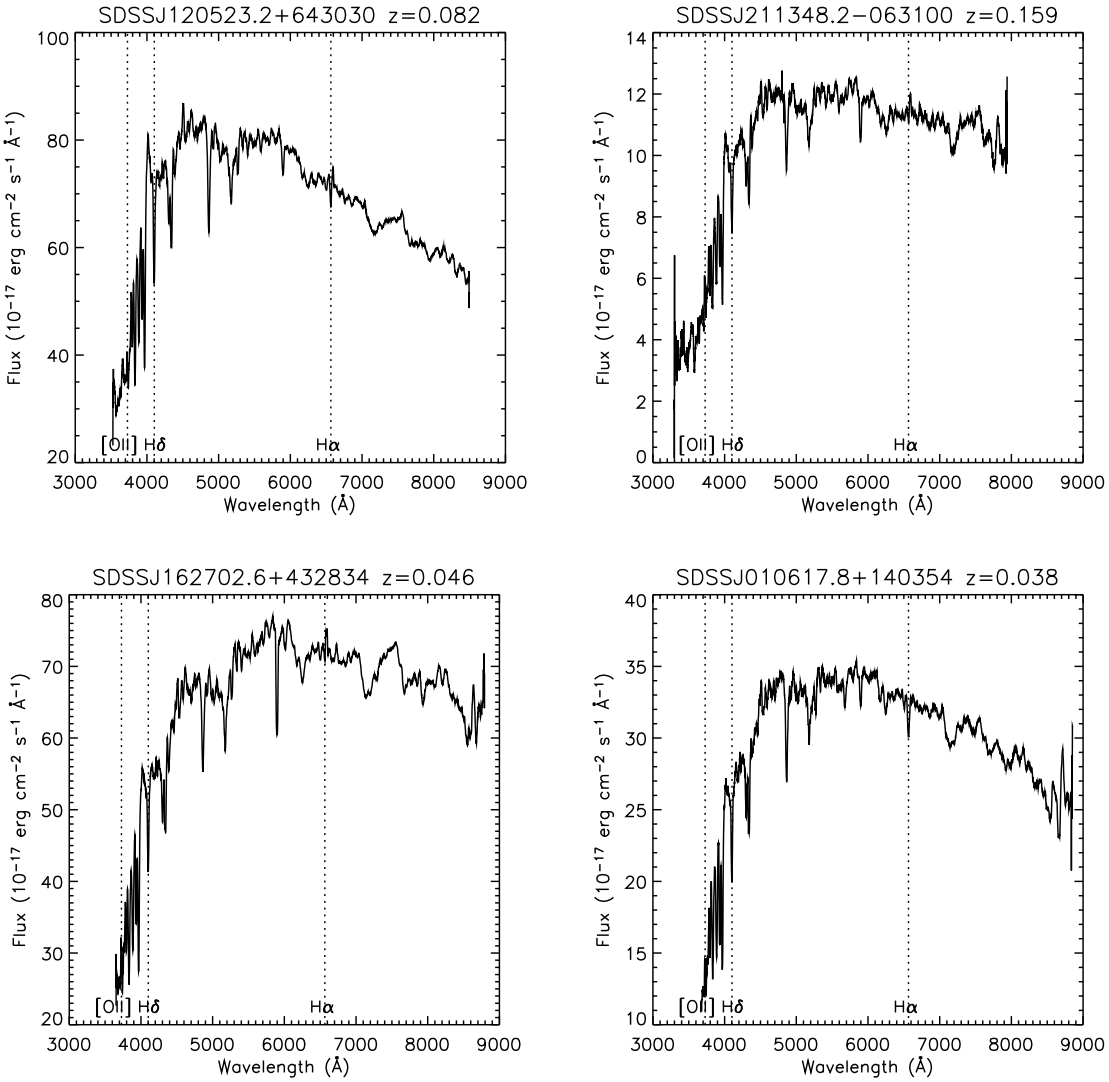

Figure 47: No.13, No.14, No.15 and No.16 E+A galaxies.

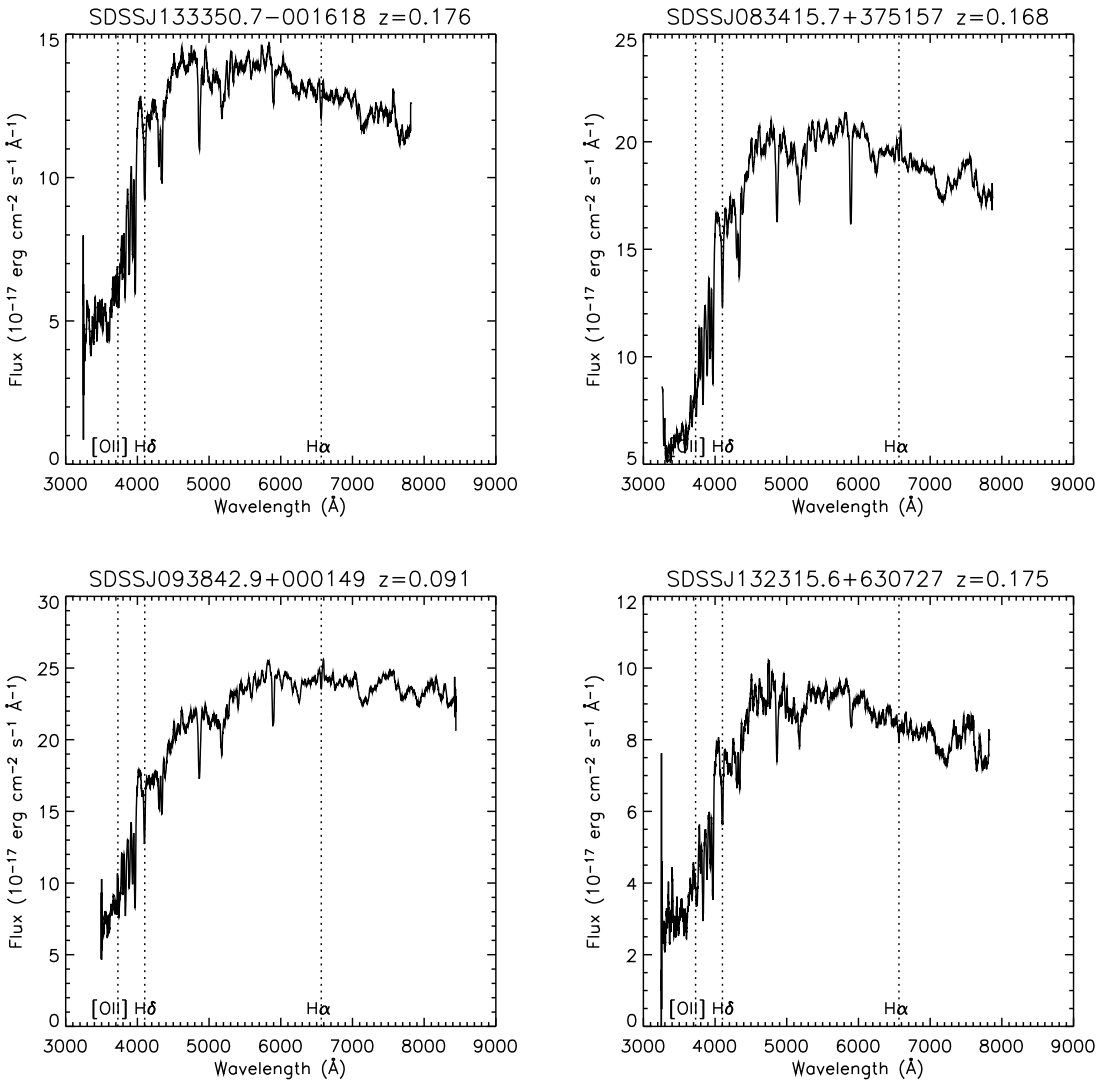

Figure 47: No.17, No.18, No.19 and No.20 E+A galaxies.

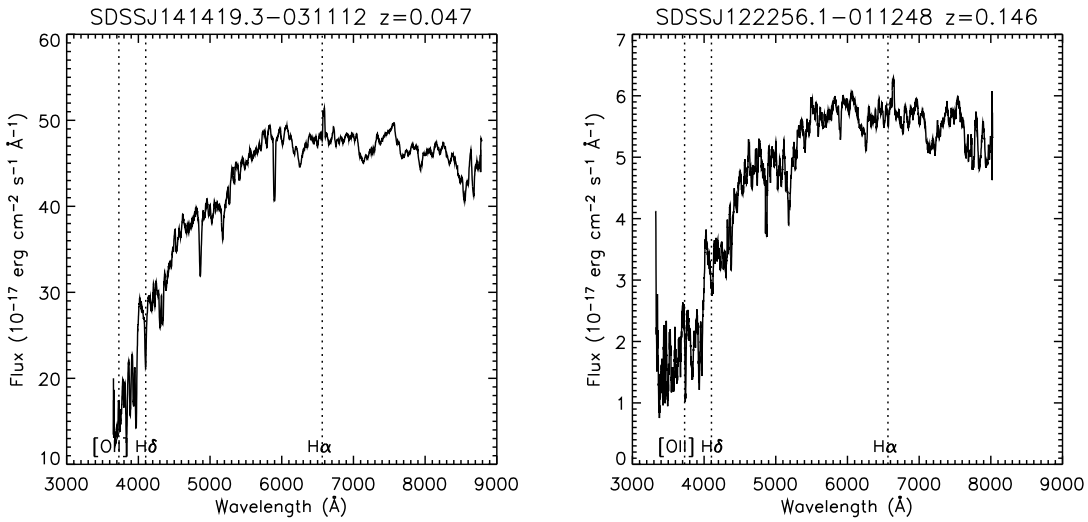

Figure 47: No.21 and No.22 E+A galaxies.

References

Abadi, M. G., Moore, B., & Bower, R. G. 1999, MNRAS, 308, 947

Abazajian, K., et al. 2003, AJ, 126, 2081

Abazajian, K., et al. 2004, AJ, 128, 502

Abraham, R. G., Valdes, F., Yee, H. K. C., & van den Bergh, S. 1994, ApJ, 432, 75

Abraham, R. G., et al. 1996, ApJ, 471, 694

Aguilar, L. A., & Merritt, D. R. 1990, ApJ, 354, 33

Arimoto, N., & Yoshii, Y. 1987, A&A, 173, 23

Ball, N. M., Loveday, J., Fukugita, M., Nakamura, O., Okamura, S., Brinkmann, J., & Brunner, R. J. 2004, MNRAS, 348, 1038

Barger, A. J., Aragon-Salamanca, A., Ellis, R. S., Couch, W. J., Smail, I., & Sharples, R. M. 1996, MNRAS, 279, 1

Barger, A. J., Cowie, L. L., Trentham, N., Fulton, E., Hu, E. M., Songaila, A. & Hall, D. 1999, AJ, 117, 102

Barnes, J. E. 1988, ApJ, 331, 699

Barnes, J. E., & Hernquist L. 1992, ARA&A, 30, 705

Bartholomew, L. J., Rose, J. A., & Gaba, A. E. AJ, 122, 2913

Baugh, C. M., Cole, S., & Frenk, C. S. 1996, MNRAS, 283, 1361

Baugh, C. M., Cole, S., Frenk, C. S., & Lacey, C. G. 1998, ApJ, 498, 504

Becker, R. H., White, R. L., & Helfand, D. J., 1995, ApJ, 450, 559

Bekki, K. 1998, ApJ, 502, L133

Bekki, K., Shioya, Y., & Couch, W. J. 2001, ApJ, 547, L17

Belloni, P., Bruzual, A. G., Thimm, G. J., & Roser, H.-J. 1995, A&A, 297, 61

Bender, R. 1998, A&A, 193, L7

Bender, R., Döbereiner, S., & Möllenhoff, C. 1998, A&AS, 74, 385

Bender, R., Surma, P., Döbereiner, S., Möllenhoff, C., & Madejsky, R. 1988, A&A, 217, 35

Bender, R., & Saura, P. 1992, A&A, 258, 250

Binggeli, B., Sandage, A., & Tammann, G. A. 1988, ARA&A, 26, 509

Blake, C., et al. 2004 MNRAS in press.

Blanton, M. R., et al. 2003, AJ, 125, 2348

Bower, R. G., Lucey, J. R., & Ellis, R. S. 1992, MNRAS, 254, 601

Brinchmann, J., & Ellis, R. S. 2000, ApJ, 536, L77

Broadhurst, T. J., Ellis, R. S., & Shanks, T. 1988, MNRAS, 235, 827

Bruzual, A. G. 1983, ApJ, 273, 105

Bruzual, A. G., & Charlot, S. 2003, MNRAS, 344, 1000

Burda, P. & Feitzinger, J. V. 1992, A&A, 261, No.2, 697

Butcher, H. & Oemler, A. J. 1984, ApJ, 285, 426

Caldwell, N., Rose, J. A., Sharples, R. M., Elllis, R. S., & Bower, R. G. 1993, AJ, 106, 473

Caldwell, N., & Rose, J. A. 1997, AJ, 113, 492

Campos, A., Yahil, A., Windhorst, R. A., Richards, E. A., Pascarelle, S., Impey, C., Petry, C. 1999, ApJ, 511, L1

Castander, F. J. et al. 2001, AJ, 121, 2331

Chang, T., van Gorkom, J. H., Zabludoff, A. I., Zaritsky, D., & Mihos, J. C. 2001, AJ, 121, 1965

Cimatti, A., et al. 1999, A&A, 352, L45

Ciotti, L., D'Eecole, A., Pellegrini, S., & Renzini, A. 1991, ApJ, 376, 380

Condon, J. J. 1992, ARA&A, 30, 575

Couch, W. J., & Shareples, R. M. 1987, MNRAS, 229, 423

Couch, W. J., Ellis, R. S., Sharples, R. M., & Smail, I. 1994, ApJ, 430, 121

Couch, W. J., Barger, A. J., Smail, I., Ellis, R. S., & Sharples, R. M. 1998, ApJ, 497, 188

Cowie, L. L., & Hu, E. M. 1998, AJ, 115, 1319

Daddi, E., Cimatti, A., Pozzetti, L., Hoekstra, H., Röttgering, H. J. A., Renzini, A., Zamorani, G., & Mannucci, F. 2000, A&A, 361, 535

Davis, R. L., Sadler, E. M., & Peletier R. F. 1993, MNRAS, 262, 650

Davies, R. L., Burstein, D., Dressler, A., Faber, S. M., Lynden-Bell, D., Terlevich, R. J., & Wegner, G. 1987, ApJS, 64, 581

de Zeeuw, T., & Franx, M. 1991, ARA&A, 29, 239

Dickinson, M. 1996, in Buzzoni, A., Renzini, A., Serrano, A., eds, ASP Conf. Ser. Vol. 86, Fresh Views of Elliptical Galaxies. Astron. Soc. Pac., San Francisco, 283

Dickinson, M., Papovich C., Ferguson, H. C., & Budavári, T. 2003, ApJ, 587, 25

Djorgovski, S., & Davis, M. 1987, ApJ, 313, 59

Doi, M., Fukugita, M., & Okamura, S. 1993, MNRAS, 264, 832

Dressler, A. 1980, ApJ, 236, 351

Dressler, A., Lynden-Bell, D., Burstein, D., Davies, R. L., Faber, S. M., Terlevich, R. J., & Wegner, G. 1987, ApJ, 313, 42

Dressler, A., & Gunn, J. E. 1983, ApJ, 270, 7

Dressler, A., & Gunn, J. E. 1992, ApJS, 78, 1

Dressler, A., Oemler, A. J., Sparks, W. B., & Lucas, R. A. 1994, ApJ, 435, L23

Dressler, A., et al. 1997, ApJ, 490, 577

Dressler, A., Smail, I., Poggianti, B. M., Butcher, H., Couch, W. J., Ellis, R. S., & Oemler, A. J. 1999, ApJS, 78, 1

Drory, N., Bender, R., Snigula, J., Feulner, G., Hopp, U., Maraston, C., Hill, G. J. & de Oliveira, C. Mendes 2001, ApJ, 562, L111

Eisenstein, D. J., et al. 2001, AJ, 122, 2267

Elston, R., Rieke, G. H., & Rieke, M. J. 1988, ApJ, 331, L77

Elston, R., Rieke, M. J., & Rieke, R. H. 1989, ApJ, 341, 80

Farouki, R., & Shapiro, S. L. 1980, ApJ, 241, 928

Faber, S. M., & Jackson, R. E. 1976, ApJ, 204, 668

Fabricant, D. G., McClintock, J. E., & Bautz, M. W. 1991, ApJ, 381, 33

Fan, X. 1999, AJ, 117, 2528

Fan, X. et al. 2003, AJ, 125, 1649

Fisher, D., Fabricant, D., Franx, M., & van Dokkum, P. 1998, ApJ, 498, 195

Fontana, A., Menci, N., D'Odorico, S., Giallongo, E., Poli, F., Cristiani, S., Moorwood, A., & Saracco, P. 1999, MNRAS, 310, L27

Franx, M. 1993, ApJ, 407, L5

Franx, M., & van Dokkum, P. G. 1996, in IAU Symp. 171, New Light on Galaxy Evolution, ed. R. Bender & R. L. Davies (Dordrecht: Kluwer), 233

Fujita, Y. 1998, ApJ, 509, 587

Fujita, Y. 2004, PASJ, 56, 29

Fujita, Y., & Goto, T. 2004, PASJ in press

Franceschini, A., Silva, L., Fasano, G., Granato, G. L., Bressan, A., Arnouts, S., & Danese, L., 1998, ApJ, 506, 600

Fukugita, M., Ichikawa, T., Gunn, J. E., Doi, M., Shimasaku, K., & Schneider, D. P. 1996, AJ, 111, 1748

Gott, J. R. 1973, ApJ, 186, 481

Gott, J. R. 1975, ApJ, 201, 296

Goto, T., 2003, PhD Thesis, The University of Tokyo, astro-ph/0310196

Goto, T. et al. 2003a, PASJ, 55, 739

Goto, T., Okamura, S., Sekiguchi, M., et al. 2003b, PASJ, 55, 757

Goto, T. et al. 2003c, PASJ, 55, 771

Goto, T. et al. 2003d, PASJ, submitted

Goto, T., Yamauchi, C., Fujita, Y., Okamura, S., Sekiguchi, M., Smail, I., Bernardi, M., & Gomez, P. L. 2003e, MNRAS, 346, 601

Goto, T. 2004, A&A, 427, 125

Goto, T. 2005, MNRAS, in press

Gunn, J. E., & Gott, J. R. I. 1972, ApJ, 176, 1

Gunn, J. E., et al. 1998, AJ, 116, 3040

Hu, E. M., Cowie, L. L., & McMahon, R. G. 1998, AJ, 115, 1319

Hogg, D. W., Schlegel, D. J., & Finkbeiner, D. P., & Gunn, J. E. 2001, AJ, 122, 2129

Hopkins, A. M., et al. 2003, ApJ, 599, 971

Im, M., et al. 2002, ApJ, 571, 136

Ivison, R. J., et al. 2002, MNRAS, 337, 1

Kauffmann, G., White, S. D. M., & Guiderdoni, B. 1993, MNRAS, 264, 201

Kauffmann, G. 1996, MNRAS, 281, 487

Kauffmann, G., Colberg, J. M., Diaferio, A. & White, S. D. M., 1999, MNRAS, 303, 188

Kelson, D. D., van Dokkum, P. G., Franx, M., Illingworth, G. D., & Fabricant, D. 1997, ApJ, 478, L13

Kennicutt, R. C. 1992a, ApJS, 79, 255

Kennicutt, R. C. 1992b, ApJ, 388, 310

Kennicutt, R. C. 1998, ARA&A, 36 189

Kent, S. M. 1981, ApJ, 245, 805

Kobayashi, C. 2004, MNRAS, 347, 740

Kodama, T., Arimoto, N., Barger, A. J., & Aragón-Salamanca, A. 1998, A&A, 334, 99

Kormendy, J. 1984, ApJ, 287, 577

Kormendy, J., & Sanders, D. B. 1992, ApJ, 390, L53

Krisciunas, K., Margon, B., & Szkody, P. 1998, PASP, 110, 1342K

Larson, R. B. 1974, MNRAS, 169, 229

Lauer, T. R. 1985, MNRAS, 216, 429

Lavery, R. J. & Henry, J. P. 1986, ApJ, 304, L5

Lavery, R. J. & Henry, J. P. 1988, ApJ, 330, 596

Liu, C. T., & Kennicutt, R. C. 1995a, ApJS, 100, 325

Liu, C. T., & Kennicutt, R. C. 1995b, ApJ, 450, 547

Lynden-Bell, D. 1967, MNRAS, 176, 367

MacLarn, I., Ellis, R. S., & Couch, W. J. 1988, MNRAS, 230, 249

Madau, P. 1997, Star Formation Near and Far : Seventh Astrophysics Conference. Edited by Steven S. Holt and Lee G. Mundy. Woodbury N. Y. : AIP Press, 393, 481

Marchant, A. B., & Shapiro, S. L. 1977, ApJ, 215, 1

Malin, D. F., & Carter, D. 1983, ApJ, 274, 534

McGlynn, T. A. 1984, ApJ, 281, 13

Menanteau, F., Ellis, R. S., Abraham, R. G., Barger, A. J., & Cowie, L. L. 1999, MNRAS, 309, 208

Meza, A., Navarro, J. F., Steinmetz, M., & Eke, V. R. 2003, ApJ, 590, 619

Miller, N. A., & Owen, F. N. 2001, ApJ, 554, L25

Mihos, J. C., Richstone, D. O., & Bothun, G. D. 1992, ApJ, 400, 153

Mihos, J. C., & Heanquist, L. 1994, ApJ, 427, 112

Mihos, J. C., & Heanquist, L. 1996, ApJ, 464, 641

Miyazaki, M., et al. 2003, PASJ, 55, 1079

Morgan, W. W. 1958, PASP, 70, 364

Morris, S. J., Hutchings, J. B., Carlberg, R. G., Yee, H. K. C., Ellingson, E., Balogh, M. L., Abraham, R. G., & Smecker-Hane, T. A. 1998, ApJ, 507, 84

Naab, T., Burkert, A., & Hernquist, L. 1999, ApJ, 523, L133

Naab, T., & Burkert, A. 2003, ApJ, 597, 893

Naim, A., Lahav, O., Sodre, L., & Storrie-Lombardi, M. C. 1995, MNRAS, 275, 567

Naim, A., Ratnatunga, K. U., & Griffiths, R.E. 1997, ApJ, 476, 510

Newberry, M. V., Boroson, T. A., & Kirshner, R. P. 1990, ApJ, 350, 585

Nikolic, B., Cullen, H., & Alexander, P. 2004, MNRAS in press

Norton, S. A., Gebhardt, K., Zabludoff, A. I., & Zaritsky, D. 2001, ApJ, 557, 150

Odewahn, S. C., Cohen, S. H., Windhorst, R. A., & Philip, N. S. 2002, ApJ, 568, 539

Oegerle, W. R., Hill, J. M., & Hoessel, J. G. 1991, ApJ, 381, L9

Oemler, A. J., Dressler, A., & Butcher, H. R. 1997, ApJ, 474, 561

Ouchi, M., et al. 2001, ApJ, 558, L83

Ouchi, M., et al. 2003, ApJ, 582. 60

Owen, F. N., Ledlow, M. J., Keel, W. C., & Morrison, G. E. 1999, AJ, 118, 633

Padmanabhan, N., et al. 2004, NewA, 9, 329

Papovich, C., Dickinson, M., & Ferguson, H. C. 2001, ApJ, 559, 620

Palunas, P., Francis, P., & Woodgate, B. 2000, AAS, 197, 107.06

Petrosian, V. 1976, ApJL, 209, L1

Pier, J. R., Munn, J. A., Hindsley, R. B., Hennessy, G. S., Kent, S. M., Lupton, R. H., & Ivezic, Z. 2003, AJ, 125, 1559

Poggianti, B. M., & Wu, H. 2000, ApJ, 529, 157

Quilis, V., Moore, B., & Bower, R. 2000, Sci, 288, 1617

Quintero, A. D., et al. 2004, ApJ, 602, 190

Rose, J. A., Gaba, A. E., Caldwell, N., & Chaboyer, B. 2001, AJ, 121, 793

Richards, G. T., et al. 2002, AJ, 123, 2945

Salpeter, E. E. 1955, ApJ, 121, 161

Sandage, A. 1961, The Hubble Atlas of Galaxies (Washington: Carnegie Inst. Washington)

Sanders, D. B., Soifer, B. T., Elias, J. H., Madore, B. F., Matthews, K., Neugebauer, G., & Scoville, N. Z. 1988a, ApJ, 325, 74

Sanders, D. B., Soifer, B. T., Elias, J. H., Neugebauer, G., & Matthews, K. 1988b, ApJ, 328, L35

Schade, D., Barrientos, L. F., & Lopez-Cruz, O. 1997, ApJ, 477, L17

Schade et al. 1999, ApJ, 525, 31

Schlegel, D. J., Finkbeiner, D. P., & Davis, M. 1998, ApJ, 500, 525

Schweizer, F. 1982, ApJ, 252, 455

Schweizer, F., & Seitzer, P. 1988, ApJ, 328, 88

Schweizer, F., Seitzer, P., Faber, S. M., Brustein, D., Ore, C. M. D., & Gonzalez, J. J. 1990, ApJ, 364, L33

Schweizer, F., & Seitzer, P. 1992, AJ, 104, 1039

Schweizer, F. 1996, AJ, 111, 109

Serra-Ricart, M., Calbet, X., Garrido, L., & Gaitan, V. 1993, AJ, 106, 1685

Sharples, R. M., Ellis, R. S., Couch, W. J., & Gray, P. M. 1985, MNRAS, 212, 687

Shimasaku, K. et al. 2001, AJ, 122, 1238

Shioya Y., & Taniguchi, Y. 1993, PASJ, 45, L39

Silva, D. R., & Bothun, G. D. 1998, AJ, 116, 85

Smail, I., Dressler, A., Couch, W. J., Ellis, R. S., Oemler, A. J., Butcher, H., & Shaples, R. M. 1997, ApJS, 110, 213

Smail, I., Morrison, G., Gray, M. E., Owen, F. N., Ivison, R. J., Kneib, J.-P., & Ellis, R. S. 1999, ApJ, 525, 609

Smith, J. A., et al. 2002, AJ, 123, 2121

Spitzer, L. J., & Baade, W. 1951, ApJ, 113, 413

Stanford, S. A., Eisenhardt, P. R. M., & Dickinson, M. 1998, ApJ, 492, 461

Steidel, C. C., Giavalisco, M., Dickinson, M., & Adelberger, K. L. 1996, AJ, 112, 352

Steidel, C. C., Adelberger, K. L., Shapley, A. E., Pettini, M., Dickinson, M. & Giavalisco, M. 2000, ApJ, 532, 170

Steinmetz, M., & Navarro, J. F. 2002, New Astron., 7, 155

Stiavelli, M., & Treu, T. 2001, in ASP Conf. Ser. 230, Galaxy Disks and Disk Galaxies, ed. J. G. Funes, S. J., & E. M. Corsini (San Francisco: ASP), 603

Storrie-Lombardi, M. C., Lahav, O., Sodre, L., & Storrie-Lombardi, L. J. 1992, MNRAS, 259, 8p

Stoughton, C., et al. 2002, AJ, 123, 485

Strateva, I., et al. 2001, AJ, 122, 1861

Strauss, M. A. et al. 2002, AJ, 124, 1810

Tanaka, M., Goto, T., Shimasaku, K., & Okamura, S. 2004, ApJ, submitted

Toomre, A. 1977, in Tinsley, B. M., Larson, R. B., eds, The Evolution of Galaxies and Stellar Populations. New Haven, Yale Univ. Observatory, p.401

Uomoto, A., et al. 2003, in prep.

van Albada, T. S. 1982, MNRAS, 201, 939

van den Bergh, S. 1998, Galaxy Morphology and Classification, Cambridge University Press

van Dokkum, P. G., & Franx, M. 2001, ApJ, 553, 90

van Dokkum, P. G., et al. 2004, ApJ, 611, 703

Venemans, B. P., at al. 2002, ApJ, 569, L11

White, S. D. M. 1979, MNRAS, 189, 831

White, S. D. M., & Frenk, C. S. 1991, ApJ, 379, 52

Yamauchi, C., & Goto, T. 2004, MNRAS, 352, 815

Yamauchi, C., Ichikawa, S., Doi, M., Yasuda, N., Yagi M., Fukugita, M., Okamura, S., Nakamura, O., Sekiguchi, M., & Goto, T., AJ, submitted.

Yan H., et al. 2004, ApJ, 616, 63

Yang, Y., Zabludoff, D., Zaritsky, D., Lauer, T., & Mihos, J. C. 2004, ApJ, 607, 258

York, D. G., et al. 2000, AJ, 120, 1579

Zepf, S. E. 1997, nature, 390, 377